Technische Universität München
Fakultät für Elektrotechnik und Informationstechnik
Lehrstuhl für Biologische Bildgebung

Development of multi-wavelength optoacoustic mesoscopy for high resolution morphological and functional imaging of skin

Andrei Berezhnoi

Vollständiger Abdruck der von der Fakultät für Elektrotechnik und Informationstechnik der Technischen Universität München zur Erlangung des akademischen Grades eines Doktors der Naturwissenschaften (Dr. rer. nat.) genehmigten Dissertation.

Vorsitzender: Prof. Dr.-Ing habil. Dr. h.c. Alexander W. Koch

Prüfer der Dissertation:

1. Prof. Dr. Vasilis Ntziachristos
2. Prof. Dr. Friedrich Simmel
3. Prof. Dr. Oliver Hayden

Die Dissertation wurde am 15.06.2020 bei der Technischen Universität München eingereicht und durch die Fakultät für Elektrotechnik und Informationstechnik am 10.12.2020 angenommen.

Abstract

In vivo skin imaging is gaining interest in medical and biological fields as an indispensable tool to study functional and morphological alteration that can enlighten functions of skin, pathophysiology of cutaneous diseases and manifestation of diabetes, cardiovascular conditions, and metabolic syndromes in skin. However, most of the techniques utilized for skin imaging are constrained by their performance and do not provide comprehensive information on the physiology and morphology of skin. For example, optical microscopy is restricted to 200 µm of penetration depth; optical coherence tomography, laser Doppler imaging, laser speckle contrast imaging, and ultrasound imaging fall short to visualize some of the fine features of human skin, such as dermal microvasculature, pilosebaceous unit, or subdermal fat layer, which are relevant to many cutaneous, systemic and metabolic diseases, due to either low resolution, poor sensitivity or contrast. The lack of suitable and comprehensive imaging modalities that can assess skin functions, visualize molecular composition and skin structures varying in size renders a need for development of new methods for morphological and functional assessment of skin.

In this thesis, the technology named raster-scanning optoacoustic mesoscopy (RSOM) was further developed and explored with an aim to tackle present challenges and limitations of the techniques conventionally employed for skin imaging. The contrast in RSOM is provided by the absorption of light, followed by the generation of ultrasound waves. Skin chromophores, e.g. hemoglobin, melanin, lipids and water, exhibit pronounced light absorption and, in principle, can be detected directly by RSOM. Furthermore, the chromophores can be distinguished based on their unique absorption spectra using multi-wavelength excitation. Owning to the detection of the induced high-frequency ultrasound signals, optoacoustic imaging achieves high depth-to-resolution ratio of ~200, making the imaging of fine skin features possible through the whole skin depth. To date, the RSOM technique has shown a great capability to capture oxygenation of dermal microvasculature and melanin at high resolution in the skin. However, further exploration and improvements are required to allow the technique to assess hemodynamic processes in cutaneous microvasculature, including oxygenation dynamics, to detect other biologically relevant bio-absorbers like water and lipids, and to image sebaceous glands, whole hair, water content in the epidermis and subcutaneous fat in addition to previously reported microvasculature and the melanin layer. Therefore, the technical development herein is focused on the multi-wavelength implementation of RSOM as well as its applicability to study dynamic processes in the skin. In terms of hardware, the main progress

of this work regards a simultaneous coupling and operation of several light sources integrated into one system as well as implementation of 24 MHz and 55 MHz transducers. The methodological aspects concern the development of a robust and precise methods for quantifying blood volume changes in human skin induced by external stimuli, imaging of the skin features from visible to short-wave infrared region, and monitoring of rapid oxygenation changes in skin microvasculature, including capillaries. The achieved technical developments are corroborated by the translational applications, such as monitoring of heat-induced hyperemic reaction, characterization of vascular changes in response to vascular-targeted photodynamic therapy and performing a post-occlusive reactive hyperemia (PORH) test to extract clinically relevant parameters of hyperemic response and oxygenation.

For the first time, a handheld clinical RSOM system was utilized to study microvascular perfusion changes in human skin in response to local hyperthermia and cutaneous treatment by pharmaceuticals. In order to provoke microvascular response to local heating, a temperature control system (TCS) was designed and built in-house. Imaging methods consisting of TCS coupled with RSOM disclosed previously unseen vasodilation of single vessels through the whole skin depth in response to focal heating. At high precision, it has been revealed that the diameter of vessels grows 1.56-fold while bulk blood volume multiplies by two- to threefold. The performance of RSOM in examining the dynamics of single microvessels proved the technique to be particularly suitable for revealing and understanding mechanisms associated with vasodilation and recruitment of microvessels in non-glabrous skin in response to external stimuli. The developed method is anticipated to bring new insights into microvascular responses associated with major diseases.

In order to achieve the goal of increasing the number of detected chromophores, the unique absorption spectra of chromophores intrinsic to human skin were thoroughly studied over a broad spectral range spanning from visible (VIS) to short-wave infrared (SWIR). Based on the retrieved optoacoustic spectra and wise selection of interrogating wavelengths, the developed ultra-wide spectrum and bandwidth (UWSB) RSOM system visualized the distribution of lipids, hemoglobin, melanin, and water content in human skin *in vivo*. Furthermore, capitalizing on the absorption spectra of the detected skin chromophores, the UWSB RSOM expanded the number of visualized skin features, which resulted in complementary imaging of microvasculature, whole hair, sebaceous glands, subcutaneous fat, melanin layer, and water content. The resolution of the non-invasive imaging of lipids, hair and water content improved more than twofold in comparison with previous reports on optoacoustic imaging, achieving ~10-30 μm. The unprecedented performance presented in this thesis of

UWSB RSOM in revealing skin features through the whole skin depth reaching below the subcutaneous fat at high resolution is expected to deliver new approaches to the detection and diagnosis of systemic diseases, as well as other clinical and biological applications.

The dynamic imaging of the oxygenation changes in skin was accomplished by upgrading the RSOM system with two fast-repetition rate lasers operating at 515 nm and 532 nm wavelengths. Dual-wavelength (DW) RSOM revealed a complex pattern of oxygenation changes over 25 h time span induced by a novel vascular-targeted cancer therapy in mouse models, and for the first time identified the initial oxygenation boost at the beginning of the therapy. Furthermore, translation of DW RSOM to oxygenation studies in humans showed a great potential for monitoring oxygenation of cutaneous microvasculature. The accuracy of the oxygenation assessment was evaluated by a developed sensitivity metric, which facilitated robust monitoring of oxygenation changes in the cutaneous microvasculature. Moreover, the optoacoustic signals attributed only to blood excluding melanin were segmented based on the metric using only two wavelengths, whereas previous approaches required at least three wavelengths. The oxygenation changes retrieved from the forearm skin as well as from the capillary loops and microvasculature of the nailfold facilitated calculation of clinically relevant oxygenation parameters, e.g. oxygen consumption, time of recovery, and time-to-peak value, which can bring new insights into understanding a range of the diseases associated with peripheral microvasculature dysfunction, such as diabetes and cardiovascular conditions. In comparison with previously reported results, the developed DW RSOM system was able to retrieve three-dimensional maps of the oxygenation changes for the first time at unprecedented resolution through the whole skin depth visualizing oxygenation in the skin microvasculature including the capillaries.

The technical advances of RSOM presented herein allow to significantly extend the range of applications accessed by the technique. Owning to the improved operation and designs of the handheld RSOM system, which incorporated several laser sources and ultrasound transducers enabling imaging of previously inaccessible skin features and monitoring of hemodynamic processes throughout the skin, the developed imaging system can be readily tested in the clinic with an aim to be translated into the clinical routine. Furthermore, the devised methodological approaches for performing pre-clinical and clinical studies establish new pathways for future applications of RSOM in functional and morphological imaging of the skin.

Zusammenfassung

Die *in vivo* Bildgebung der Haut gewinnt in den Bereichen der Medizin und Biologie an großem Interesse und ist für die Detektion funktioneller sowie morphologischer Veränderungen unerlässlich, welche nicht nur Einblicke in die Hautfunktion, sondern auch in die Pathophysiologie kutaner Erkrankungen sowie die Manifestation von Diabetes, Herz-Kreislauf-Erkrankungen und metabolischen Syndromen liefern. Die meisten verwendeten Techniken sind jedoch in ihrer Leistungsfähigkeit stark eingeschränkt und liefern keine ausreichend umfassenden Informationen zur Physiologie und Morphologie der Haut. Beispielsweise ist die optische Mikroskopie auf eine Eindringtiefe von lediglich 200 µm beschränkt; die optische Kohärenztomographie, die Laser-Doppler-Bildgebung, die Laser-Speckle-Kontrast-Bildgebung und kommerzieller Ultraschall scheitern an der Visualisierung feiner Strukturen in der menschlichen Haut, wie dermale Mikrogefäße, Pilosebaceous-Einheiten oder Unterhautfettschichten, welche für viele kutane, systemische oder metabolische Erkrankungen relevant sind, aufgrund geringer Auflösung, Sensitivität oder Kontrast. Dies macht die Entwicklung neuer, umfassenderer Methoden erforderlich, welche für die Beurteilung von Hautfunktionen und -morphologie sowie zur Visualisierung der molekularen Zusammensetzung und unterschiedlich großer Hautstrukturen notwendig sind.

In dieser Arbeit wurde die sogenannte Raster-Scanning Optoacoustic Mesoscopy (RSOM) Technologie weiterentwickelt und für die Hautbildgebung erforscht, um so die Herausforderungen und Limitationen der heutzutage konventionell verwendeten Modalitäten zu überwinden. Die Erzeugung von Kontrast basiert bei RSOM auf der Absorption von Licht und der darauffolgenden Generierung von Ultraschallwellen im Gewebe. Chromophore in der Haut, wie zum Beispiel Hämoglobin, Melanin, Lipide oder Wasser weisen eine ausgeprägte Absorption von Licht auf und können somit direkt durch RSOM nachgewiesen werden. Darüber hinaus können diese Chromophore aufgrund ihrer einzigartigen Absorptionsspektren und unter der Verwendung verschiedener Anregungswellenlängen voneinander unterschieden werden. Durch die Detektion der generierten hochfrequenten Ultraschallsignale erreicht die optoakustische Bildgebung ein hohes Tiefe-zu-Auflösung Verhältnis von ~200, wodurch die Darstellung sehr feiner Strukturen über die gesamte Hauttiefe ermöglicht wird. Bislang war es mittels RSOM bereits möglich, die Oxygenierung von dermalen Mikrogefäßen sowie Melanin in hoher Auflösung zu erfassen. Es sind jedoch weitere Untersuchungen und Optimierungen erforderlich, um hiermit auch hämodynamische Prozesse in den Mikrogefäßen zu evaluieren, einschließlich Sauerstoffdynamiken, um andere biologisch relevante Absorber wie Wasser oder Lipide nachzuweisen, und auch Talgdrüsen, ganze Haare, den Wassergehalt in der Epidermis

und subkutanes Fett zusätzlich zu den zuvor genannten Mikrogefäßen und der Melaninschicht abzubilden. Daher fokussiert sich die technische Entwicklung in dieser Arbeit auf die Implementierung von RSOM mit mehreren Wellenlängen sowie auf seine Anwendbarkeit zur Untersuchung dynamischer Prozesse in der Haut. In Bezug auf die Hardware besteht der Fokus in der gleichzeitigen Kopplung und Operation mehrerer in ein System integrierter Lichtquellen sowie in der Implementierung von 24 MHz und 55 MHz Ultraschalltransducern. Die methodischen Aspekte dieser Arbeit liegen in der Entwicklung robuster und präziser Verfahren zur Quantifizierung von extern induzierten Blutvolumenänderungen in der menschlichen Haut, der Darstellung von Hautmerkmale vom sichtbaren zum kurzwelligen Infrarotbereich und der Überwachung kurzfristiger Änderungen der Sauerstoffversorgung in den Mikrogefäßen der Haut, einschließlich der Kapillaren. Die erzielten technischen Entwicklungen werden durch translationale Anwendungen belegt, wie die Verfolgung der hitzeinduzierten hyperämischen Reaktion, die Charakterisierung von vaskulären Veränderungen als Reaktion auf eine speziell vaskulär-ausgerichtete photodynamische Therapie und die Durchführung eines Tests zur postokklusiven reaktiven Hyperämie (PORH) zur Extraktion klinisch relevanter Parameter.

Zum ersten Mal wurde außerdem ein handgehaltenes klinisches RSOM verwendet, um mikrovaskuläre Perfusionsänderungen in der menschlichen Haut als Reaktion auf lokale Hyperthermie und Arzneimittelbehandlung zu untersuchen. Um die mikrovaskuläre Reaktion auf lokale Erwärmung hervorzurufen, wurde intern ein Temperaturkontrollsystem (TCS) entworfen und gebaut. Hierbei haben bildgebende Verfahren, die aus einem TCS-gekoppeltem RSOM bestehen, eine bisher nicht sichtbare Vasodilatation einzelner Gefäße über die gesamte Hauttiefe als Reaktion auf eine fokale Erwärmung offenbart. Mit hoher Präzision hat sich gezeigt, dass sich der Durchmesser der Gefäße um das 1,56-fache vergrößert, während sich das Gesamtblutvolumen um das Zwei- bis Dreifache vervielfacht. Die Performance von RSOM erwies sich bei der Detektion der Dynamik einzelner Mikrogefäße als besonders geeignet und deckte Mechanismen auf, die zum Verstehen von Vasodilatation und der Rekrutierung von Mikrogefäßen in behaarter Haut als Reaktion auf äußere Reize unerlässlich sind. Die hier entwickelte Methode soll neue Erkenntnisse über mikrovaskuläre Reaktionen im Zusammenhang mit bedeutenden Krankheiten liefern.

Um eine erhöhte Anzahl nachweisbarer Chromophore zu erzielen, wurden die spezifischen Absorptionsspektren von intrinsischen Chromophoren der menschlichen Haut über einen ausgedehnten Bereich vom sichtbaren (VIS) bis kurzwelligen Infrarot (SWIR)-Spektrum umfassend untersucht. Basierend auf den gewonnenen optoakustischen Spektren und der überlegten Auswahl von Anregungswellenlängen, konnte das entwickelte RSOM System

mit ultraweitem Spektrum und Bandbreite (UWSB) die Verteilung von Lipiden, Hämoglobin, Melanin und Wassergehalt in der menschlichen Haut *in vivo* visualisieren. Darüber hinaus konnte das UWSB RSOM, basierend auf den Absorptionsspektren der detektierten Chromophore, eine Reihe von weiteren Hautmerkmalen visualisieren, was zu einer zusätzlichen Darstellung von Mikrogefäßen, vollständigen Haaren, Talgdrüsen, subkutanem Fett, der Melaninschicht und des Wassergehaltes führte. Die Auflösung der nicht-invasiven Bildgebung von Lipiden, Haaren und des Wassergehaltes verbesserte sich im Vergleich zu früheren Berichten der optoakustische Bildgebung um mehr als das Doppelte und erreichte ~10-30 µm. Die in dieser Arbeit gezeigte beispiellose Performance von UWSB RSOM zur Detektion von Merkmalen über die gesamte Hauttiefe, die mit hoher Auflösung selbst unter das subkutane Fett reicht, soll neue Ansätze für die Erkennung und Diagnose systemischer Erkrankungen sowie für andere klinische und biologische Anwendungen liefern.

Die Detektion von Änderungen in der Oxygenierung in der Haut wurde durch eine Aufrüstung des RSOM Systems mit zwei Lasern mit hoher Frequenz bei Wellenlängen von 515 nm und 532 nm ermöglicht. Das RSOM System mit zwei Wellenlängen (DW) zeigte ein komplexes Muster von Änderungen in der Oxygenierung über einen Zeitraum von 25 Stunden nach anti-vaskulärer Krebstherapie in Mausmodellen, und identifizierte erstmalig eine Anflutung von Sauerstoff kurz nach Beginn der Therapie. Darüber hinaus zeigte die Translation von DW RSOM auf Oxygenierungsstudien am Menschen großes Potential zur Überwachung von Sauerstoffänderungen in kutanen Mikrogefäßen. Die Genauigkeit dieser Messungen wurde mittels eigens entwickelter Sensitivitätsmetrik bewertet, welche eine robuste Überwachung der Oxygenierungsänderungen in der kutanen Mikrovaskulatur ermöglichte. Des Weiteren wurden die optoakustischen Signale, welche nur dem Blut ohne Melanin zugeschrieben wurden, basierend auf der Metrik unter Verwendung von nur zwei Wellenlängen segmentiert, während frühere Ansätze mindestens drei Wellenlängen benötigten. Die Oxygenierungsänderungen, die in der Unterarmhaut sowie den Kapillarschlingen und Mikrogefäßen der Nagelfalz gemessen wurden, erleichterten die Berechnung klinisch relevanter Oxygenierungsparameter, wie Sauerstoffverbrauch, Wiederherstellungszeit und Zeit bis zum Höchstwert. Diese können neue Erkenntnisse zum Verständnis einer Reihe von Krankheiten liefern, die mit Funktionsstörungen der peripheren Mikrovaskulatur verbunden sind, wie Diabetes und Herz-Kreislauf-Erkrankungen. Im Vergleich zu zuvor berichteten Ergebnissen konnte das hier entwickelte DW RSOM erstmalig dreidimensionale Bilder von Oxygenierungsänderungen mit hoher Auflösung über die gesamte Hauttiefe generieren und die Oxygenierung in den Mikrogefäßen, einschließlich der Kapillaren, sichtbar machen.

Die hier dargestellten technischen Fortschritte von RSOM ermöglichen eine enorme Erweiterung des Anwendungsbereiches für diese Technologie. Aufgrund der verbesserten Bedienung und des optimierten Designs des handgehaltenen RSOMs, welches mehrere Laserquellen und Ultraschalltransducer enthält, die die Bildgebung bisher nicht-detektierbarer Merkmale der Haut und die Überwachung hämodynamischer Prozesse durch die gesamten Hautschichten ermöglicht, kann das entwickelte Bildgebungssystem problemlos in der Klinik getestet werden, mit dem Ziel der Überführung in die klinische Routine. Darüber hinaus eröffnen die entwickelten methodischen Ansätze zur Durchführung präklinischer und klinischer Studien neue Wege für zukünftige Anwendungen von RSOM in der funktionellen und morphologischen Bildgebung der Haut.

Glossary

1D, 2D, 3D	1-, 2-, 3-dimensional
AMP	Amplifier
ANSI	American National Standards Institute
AR	Axial resolution
BCC	Basal cell carcinoma
BZ	Biological zero
CARS	Coherent anti-Stokes Raman scattering
CCD	Charged Coupled Device
DAQ	Data acquisition
DNA	Deoxyribonucleic acid
DPSS	Diode-pumped solid state
DW RSOM	Dual-wavelength RSOM
FOV	Field of view
GPU	Graphical processing unit
GUI	Graphical user interface
Hb	Deoxygenated hemoglobin
HbO_2	Oxygenated hemoglobin
HCA	Nitric oxide scavenger
HFUS	High frequency ultrasound
HGb	Hemoglobin
HIV	Human Immunodeficiency Virus
IU	Interface unit
LDF	Laser Doppler flowmetry
LDPI	Laser Doppler perfusion imaging
LR	Lateral resolution
LSCI	Laser speckle contrast imaging
MIP	Maximum intensity projection
MM	Multiphoton microscopy
MSOT	Multispectral optoacoustic tomography

NADH	Nicotinamide adenine dinucleotide (NAD) + hydrogen (H)
NADPH	Nicotinamide adenine dinucleotide phosphate
Nd:YAG	Neodymium-doped Yttrium Aluminum Garnet
NIR	Near-infrared
NIRS	Near-infrared spectroscopy
OA	Optoacoustics
OAI	Optoacoustics imaging
OCT	Optical coherence tomography
OMAG	Optical microangiography
OPIND	Index of optoacoustic features
OPO	Optical parametric oscillator
OT	Optoacoustic tomography
PBV	Partial blood volume
PC	Personal computer
PORH	Post-occlusive reactive hyperemia
PVDF	Polyvinylidene fluoride
RCM	Reflectance confocal microscopy
RGB	“Red Green Blue” color-scheme
ROI	Region of interest
RSOM	Raster-scanning optoacoustic mesoscopy
SCC	Squamous cell carcinoma
SF	Sensitivity field
SHG	Second harmonic generation
SIR	Spatial impulse response
SRC	Stimulated Raman scattering
SWIR	Short-wave infrared region
TBV	Total blood volume
TCS	Temperature control system
UB RSOM	Ultra-wideband raster-scan optoacoustic mesoscopy
UV	Ultraviolet

UWSB RSOM	Ultra-wide spectrum and bandwidth raster-scan optoacoustic mesoscopy
VIS	Visible range
VTP	Vascular-targeted photodynamic therapy

List of Tables

Table of Figures

Table of Contents

1. Introduction

1.1. Motivation for morphological and functional imaging of skin

The visualization of morphology and monitoring of physiological functions of skin *in vivo* can significantly benefit diagnosis and treatment of cutaneous and systemic diseases through their manifestations in skin. Despite the prominent contrast achieved by optical microscopy techniques, complex laminous structure of skin reaching 5 mm in depth and characterized by strong light scattering limits their application. The cohort of diffuse optical modalities (optical coherence tomography, laser Doppler imaging, laser speckle contrast imaging, etc.) and ultrasound imaging do not exhibit resolution, sensitivity, or contrast to visualize fine skin features, e.g. dermal microvasculature, pilosebaceous unit or subcutaneous fat. Therefore, the challenges of the skin imaging can be attributed to developing new imaging modalities that enable assessment of skin functions and visualization of skin features varying in size and molecular composition.

The main objective of this work is to develop and explore an imaging method that could deliver for the first time label free imaging capabilities to visualize concurrently skin microvasculature, pilosebaceous unit, epidermis and subcutaneous fat and assess physiological functions of skin, such as blood volume changes, vasodilation, and oxygenation alterations in microvascular bed. The imaging method is based on raster-scanning optoacoustic (photoacoustic) mesoscopy (RSOM), which capitalizes on the detection of the ultrasound waves generated through the photoacoustic effect. As the acoustic scattering is few orders of magnitude less than optical scattering, optoacoustic imaging breaks the optical diffusion limit achieving a high depth-to-resolution ratio while preserving strong optical contrast. Besides, the multispectral excitation of the skin chromophores enables their separation based on their unique absorption spectra. In summary, this work focuses on achieving new methods for functional and morphological imaging of skin by means of RSOM [1,2].

Functional skin imaging concerns retrieving the information about the blood dynamic in the microvasculature including blood volume changes, absorption of chemicals, oxygenation and metabolic activity. The rate of such changes is usually in the range from few seconds to minutes. The challenge in achieving functional skin imaging herein is to address the problem of rapid microvascular changes assessed by RSOM while preserving high resolution-to-depth ratio and to develop a method that has a potential to be transferred to clinical bedside, particularly for monitoring changes in blood volume and oxygenation of microvasculature.

The retrieval of the distribution and shape of skin appendages and structures is provided by morphological (structural) imaging. Imaging modalities exploit various physical phenomena as their underlying contrast mechanism. Such physical phenomena may occur when electromagnetic or pressure waves encounter matter, inducing, for example, reflection, scattering, or absorption. The contrast in optoacoustics is based on the absorption of light followed by the generation of ultrasound waves. The focus of the morphological imaging herein is to explore light absorption properties of skin biomolecules in a broad spectral range, to expand the number of molecules detected by RSOM, and to optimize approaches for imaging of skin structures and appendages based on their molecular composition through the whole skin depth.

This chapter is dedicated to give a brief introduction to the clinical importance of the skin imaging. The review on the conventionally employed techniques for skin imaging outlines their limitations, whereas the results achieved by RSOM help to identify the next steps of the development. Furthermore, the objectives of this thesis are defined to further improve multi-wavelength RSOM and push its limits towards morphological and functional imaging of skin.

1.2. Clinical relevance of skin imaging

Skin diseases have been reported to carry a significant disease burden worldwide [3], while their prevalence is predicted to exceed occurrence and to be similar in cost of diabetes and cardiovascular diseases. The economic burden of skin diseases has been estimated to be of 85$ billion of direct and 11$ billion of indirect losses in the US alone making them important for public health consideration. Skin diseases were ranked 18th globally in DALYs (index of disability-adjusted life years) and 4th in non-fatal global burden disease [4]. They lead to pain, decreasing quality of life, psychological morbidity and significantly increase financial burden. Additionally, they are often a manifestation of systemic diseases, diabetes, metabolic syndrome and cardiovascular diseases and, if detected at a very early stage, can lead to improvement of diagnostics and treatment approaches of systemic diseases.

The increasing incidence of melanoma and non-melanoma skin cancer by 2.6% over the last decades [5] requires better diagnosis in order to prevent metastasis of the melanoma and malignant neoplasms (keratinocyte carcinomas, namely basal cell carcinoma (BCC), squamous cell carcinoma (SCC) and to decrease mortality rate. Skin cancers correspond to 60% of all skin-related deaths [6]. Increasing incidence, mortality rate, and growing burden of skin cancers may be regarded as melanoma epidemic [7,8]. Non-invasive imaging techniques can aid diagnostic accuracy and reduce number of required excisions of suspicious lesions [9]. Despite of improving and developing new non-invasive techniques for skin cancer detection, the histopathological analysis is still a gold standard in the assessment of skin cancers. Melanoma volume and tumor progression in depth play crucial role in tumor assessment, which help to identify stage of the cancer and, therefore, the therapeutic measures [10]. Furthermore, tissue hypoxia is associated with a wide range of tumors including skin cancer promoting tumor growth, and can be an indicator of malignancy of the cancer [11,12]. Another indicator of melanoma aggressiveness is presence of the adipocytes in the proximity to the cancer cells. Melanomas proliferate in dermis without metastasizing before they reach fat cells that trigger metastatic initiation [13]. Non-invasive imaging with lipid specific contrast of non-melanoma tumors and their differential diagnosis can aid their detection, lead to the reduced number of surgeries, cost of medical interventions and to adjustment of a treatment plan accordingly [14].

Inflammatory skin diseases, e.g. atopic eczema, contact dermatitis, urticarial, seborrheic dermatitis, psoriasis, and acne often appear in the presence of infection, allergy or autoimmune conditions [15]. Pathogenesis of inflammatory skin diseases is still not unraveled precisely because of their often similar manifestations and, therefore, requires further investigation [16].

Inflammatory skin diseases often associated with changes in microvascular morphology and functional changes. As an example, establishment of psoriatic plaque is characterized by promoting angiogenesis, increase in the blood flow even in unaffected skin, and structural changes of capillary loops from arterial to venous phenotype [17]. While atopic eczema and psoriasis are manifested through different immune responses, their diagnosis can be ambiguous leading to inaccurate treatment [18]. Therefore, identification of specific biomarkers attributed only to psoriasis or atopic eczema using non-invasive imaging techniques can improve their diagnosis and reduce treatments cost [19].

Human skin is the first outpost that interacts with pathogens and prevents them via immune responses from penetrating to inner organs. Disruption of physiological control over the immune system can lead to the development of autoimmune diseases [20]. While histopathology along with visual assessment remain the gold standard to diagnose autoimmune diseases, non-invasive monitoring can benefit their detection by reducing the number of required incisions and improving therapeutic approaches. For example, assessment of hair follicle has a diagnostic potential in cutaneous lupus and alopecia areata, since it is believed to be a reservoir for epidermal stem cell [21]. Today's approach for studying hair follicle involves semi-invasive method trichogram (hair plucking) and requires removal of number of hairs for further analysis. Systemic sclerosis is characterized by the hardening of connective tissue and damage of the microvasculature, leading to reduced blood flow and ischemia. However, the etiology of the systemic sclerosis is still unknown. Therefore, assessment of microvasculature structural and functional changes may help to improve classification of the disease severity and progression [22].

Cardiovascular diseases, as well as diabetes and metabolic syndrome can lead to microvascular dysfunction and changes in skin microvascular morphology [23–25]. Furthermore, early detection of systemic diseases based on skin manifestations is considered a promising direction for facilitating more effective treatment [26]. This is hardly surprising given that the skin is regulated by metabolic and homeostatic processes and is systemically affected by various health conditions. For example, obesity and diabetes are associated with abnormalities in the dermal microvascular bed, reflecting poor skin perfusion and impaired endothelial function [27–29]. Congestive heart failure [30,31], atherosclerosis [32] and metabolic syndrome [33] may be associated with altered vascular responses, which can be measured as an impairment in heat-induced vasodilation and associated increase in skin perfusion, known as hyperemia [30]. Thus, measuring the vascular response to heating may uncover generalized systemic vasculature dysfunction associated with the progression of different diseases [34,35], and could provide better cardiovascular risk assessment than the Framingham Risk Score [36].

Subcutaneous fat morphology has been reported to correlate with cardiovascular risk factors [37], while functional parameters of lipids can be linked to insulin sensitivity and weight loss [38]. Up to 50% of people with diabetes suffer xerosis cutis (dry skin) and hair loss, which is reflected in dysfunction of lipid-rich sebaceous glands and abnormal hydration state of the stratum corneum [39,40]. Elevated glucose level in diabetes is known to impair microvasculature function and may lead to hair loss and dysfunction of other skin components [41]. It has been shown that Type 2 diabetes can cause changes in microvascular hemodynamic and vessel density in skin as well as reduced thickness of adipose tissue and density of hair follicles [42]. Additionally, certain metabolic disorders can be distinguished based on reactivity of dermal microvasculature to pressure-induced and acetylcholine-induced (endothelium-dependent) vasodilation accompanied by metaflammation in dermal white adipose tissue [43].

Transdermal drug delivery has been considered as an alternative to oral drug delivery and to hypodermal injections. Oral drug delivery can pose a problem when pharmaceutical ingredients are absorbed by the digestive system and broken down in liver reducing longitudinal effects of the drugs. Hypodermal injections are painful, may require professional assistance and increase the risk of disease transmission through re-use of needles. At the same time, transdermal delivery approaches offer self-administration and precise dosage control over extended period of time [44]. However, the protective function of the stratum corneum can act as a barrier for transdermal drug delivery and topical application of cosmetics, particularly hydrophilic drugs, peptides and macromolecules. Therefore, the use of non-invasive imaging modalities can significantly benefit the discovery of drugs suitable for transdermal applications by monitoring their progression through the epidermis and deeper in the tissue.

1.3. Skin imaging techniques and their limitations

Skin imaging is still a growing field with many encouraging results, however, most of the developed techniques are yet to be utilized in clinics and still under-go research trials. In this section the techniques conventionally employed in skin imaging will be reviewed to outline their performance, solutions they bring and their limitations. Furthermore, the state of art of optoacoustic mesoscopy and its challenges in terms of morphological and functional skin imaging will outline the basis for this thesis.

Reflectance confocal microscopy

Optical microscopy imaging techniques have been considered for non-invasive skin assessment in dermatology. For example, Reflectance confocal microscopy (RCM) is widely employed in clinical routine and has been recently approved for reimbursement of treatment [45]. RCM is based on the detection of tightly focused light back-scattered from the interfaces of structures with different refractive indices, besides a spatial filter (a pinhole) is used to reject the back-scattered light originating from out-of-focus planes [46]. RCM achieves 2-5 µm of axial resolution and 0.5-1 µm of lateral resolution, but it is limited to a depth of 200 µm in skin imaging [45].

Since the contrast of RCM is given by the light reflected in the tissue, RCM has been able to deliver mainly morphological information on cellular and nuclear level in the epidermal layers and the superficial reticular dermis *in vivo* [47]. Because of a superficial penetration depth, RCM has been found suitable primarily for the cutaneous diseases that are characteristic for the epidermis and the upper dermis, e.g. contact dermatitis, onychomycosis, bacterial folliculitis, warts, and psoriasis [48]. For example, RCM has revealed more than two-fold vasodilation of the capillaries at the epidermal-dermal junction and the dermal papilla in psoriatic skin in comparison to healthy one [49]. Furthermore, RCM has been reported to show a two-times improved specificity to non-melanocytic and to non-pigmented melanocytic lesions of around 90% [45,50]. Despite the proven clinical value of RCM, the penetration depth of only 200 µm in cutaneous tissue and inadequate ability to distinguish melanocytes from keratinocytes or impaired differentiation of the epidermal-dermal junction limit the further translation of the technique to the clinical applications that require greater imaging depths and better specificity to the skin structures [45].

Multiphoton microscopy

Multiphoton microscopy (MM) provides molecular specificity to several skin endogenous fluorophores based on the multiphoton excitation (e.g. NADH/NADPH, melanin, keratin and elastin) and on the second harmonic generation (collagen) [51]. The conversion of multiple photons into one photon of higher energy can be attributed to different phenomena underlying light-matter interaction: multiphoton fluorescence and higher harmonic generation. Multiphoton fluorescence relies on the high intensity optical irradiation, which may result in coherent absorption of two or more photons followed by the emission of de-exciting fluorescence photons. Second harmonic generation (SHG) is based on the elastic scattering at non-centrosymmetric structures of the several photons converted into one photon of double frequency. *In vivo* imaging of melanoma legions compared with melanocytic nevi showed that multiphoton techniques are able to identify crucial biomarkers of the malignant lesions with specificity up to 97% [52]. Despite the high resolution of 0.3 µm in lateral plane and 1 µm in axial and pronounced sensitivity to the skin molecules, MM suffers the shallow imaging depth around 200 µm similar to RCM [51].

Raman microscopy

Raman scattering microscopy capitalizes on the inelastic scattering of the incident photons providing the information about vibrational spectral signatures of the probed molecules. The probability of the inelastic scattering is 1 in 10 million of elastically scattered photons, which makes the detection of these events a difficult task and requires long integration times and/or high light energies in real spectroscopic or imaging systems. Coherent anti-Stokes Raman (CARS) spectroscopy and stimulated Raman spectroscopy (SRS) take advantage of multiphoton coherent excitation of molecular vibrational modes to achieve much stronger vibrational signals [53,54]. The CARS and SRC signals are particularly sensitive to C-H vibrational modes at the resonance wavelength around 2,800–3,100 cm^{-1}, which makes them suitable for imaging of skin structures rich with lipid content, such as stratum corneum, sebaceous glands, nerves and adipocytes [55]. Current technical development techniques based on Raman scattering allows video rate imaging of biological tissue in epi-detection mode, which is particularly important for imaging of living tissue *in vivo*. However, the penetration depth is intrinsically limited by the focusing of the light in highly scattering tissue and by the weak generated signals. As the result, the penetration depth in skin does not exceed 150 µm at resolution of few micrometers [54].

Laser Doppler flowmetry

Laser Doppler flowmetry (LDF) is based on the detection of the Doppler shifts caused by the dynamic laser light scattering on the moving red blood cells in tissue [56] and provides clinically relevant relative parameters of the blood flow in tissue, such as flux, velocity and concentration of the moving blood cells. Therefore, LDF has shown a capability to detect hyperemic response in human forearm skin locally heated to 35-43 ºC [57,58], where bulk blood flow was recorded with spatial resolution of ~1.0 mm^3 at depth down to 4 mm [59]. In order to enable spatial measurements of relative skin perfusion values associated with thermally induced hyperemia, the laser beam of the laser Doppler perfusion imaging (LDPI) system is scanned over a region of interest generating perfusion maps of the heterogeneous tissue [60,61]. However, the so called "biological zero" (BZ) signal attributed to Brownian motion, vessel activity and other moving structures in the tissue is present in both LDF and LDPI measurements and has a strong impact on the blood flow signals. Therefore, in order to achieve the quantitative analysis of the blood flow the BZ signal has to be taken into account. While there have been several attempts to approach this problem, the further investigation of the processes involved in the laser Doppler signal generation and accurate estimation of the BZ signal are required [59].

Laser speckle contrast imaging

Laser speckle contrast imaging (LSCI) is based on the analysis of the fluctuation of the speckle patterns produced by the phase shifts in scattered light induced by moving red blood cells (or other moving entities) and recorded by a CCD camera [62]. Intensity of the speckle pattern fluctuates more rapidly in the regions of increased blood flow; this leads to blurring of the speckle pattern when it is integrated over exposure time (typically 1 to 10 ms) of the CCD camera. By acquiring an image of the speckle pattern and quantifying the blurring of the speckles, spatial maps of relative blood flow can be obtained. LDPI and LSCI typically characterize superficial flow as they rely on photons scattered from the surface of the imaged tissue. Furthermore, LSCI allows acquisition of skin perfusion maps over a large region with higher temporal resolution than LDPI, however, it has been reported that in order to improve the repeatability of blood flow measurements using LPDI or LSCI, the techniques require further development [60,61].

Optical coherence tomography

Optical coherence tomography (OCT) uses low-coherent light back-scattered from the interfaces of tissues with different refractive indices. By using so-called "coherence gating", which is based on interferometric principles, the photons that undergo multiple scattering events are rejected, achieving high resolution with relatively deep penetration (1-1.5 mm). Since the contrast is based on refractive index heterogeneity, conventional OCT images provide mainly morphological information, while the retrieved oxygenation parameters in mouse skin were poor [63]. Conventional OCT has been reported to resolve the stratum corneum, dermis and hair follicles achieving resolution better than 20 µm in lateral and below 5 µm in axial axis [64], but in general is prone to subjective differentiation of the skin structures and falls short in resolving subcutaneous fat and blood vessels [65]. Optical micro-angiography (OMAG), an extension of conventional OCT, has been able to visualize blood flow in human skin microvasculature. However, the penetration depth of OMAG for microvasculature imaging is limited to 400 µm and the axial resolution is strongly affected by imaging artefacts in the axial direction [66].

Ultrasound microscopy

Alternatively to optical imaging modalities, high-frequency ultrasound (HFUS) imaging has shown applicability in dermatology [67]. Analogous to OCT, imaging contrast of HFUS is provided by the waves reflected from the interfaces of tissues, but uses ultrasound instead of photons and, thus, detects changes in acoustic impedance. In this matter, HFUS is similar to OCT and OMAG and cannot provide information of the molecular composition of skin. Resolution and imaging depth are inversely related in HFUS and related to the bandwidth of the transducer. For instance, 20 MHz central frequency transducer allows 10 mm imaging depth with 30 µm axial resolution, whereas transducers of 55 MHz central frequency achieves 10 µm axial resolution at depths down to 3 mm [68]. The variation of the ultrasound refractive index among dermal structures is rather weak, which leads to the poor contrast of ultrasound imaging making the visualization of microvasculature angiogenesis and inflammation strongly hampered [69]. Recent development of ultrafast ultrasound localization microscopy (µULM) allows the imaging of microvessels below 10 µm in diameter [67]. However, to visualize the microvasculature, µULM requires injection of contrast agents. The weak contrast of HFUS significantly impedes segmentation and visibility of skin structures in the acquired images [70]. While HFUS can resolve the border of the fat layer, low acoustic impedance heterogeneity of epidermis does not allow differentiation of epidermal layers or dermal microvasculature [71].

1.3.1. Optoacoustic imaging of skin

Photoacoustic effect is based on the absorption of non-ionizing modulated electromagnetic waves by molecules followed by the conversion of the absorbed energy into heat and generation of ultrasound waves, which are referred as an optoacoustic (photoacoustic) signal. Until the 1990’s the photoacoustic effect was primarily applied to spectroscopic analysis of gases. However, further development of the laser and detector technologies, in particular high power and fast pulsed light sources and broadband ultrasonic detectors, allowed utilization of the technique for medical and biological imaging [72]. Optoacoustic imaging (OAI) possesses several key features that can be used to fulfil this resolution gap while preserving sufficient penetration to image through the whole skin depth [73].

First, the contrast in OAI is based on the absorption of incident light by molecules composing biological tissue. Many endogenous chromophores in skin, e.g. such as hemoglobin, melanin, collagens, lipids and water exhibit strong absorption of light in visible and near infra-red spectral regions and can be detected directly [74]. The ability to visualize skin microvascular based on the hemoglobin contrast can provide insights into vessel angiogenesis during tumor development, while obesity and diabetes are associated with abnormalities in the dermal microvascular bed, reflecting poor skin perfusion and impaired endothelial function [27–29]. Imaging of pilosebaceous glands that are rich in lipid content as well as hair based on melanin contrast can reveal condition associated with xerosis cutis and hair loss [39,40]. Subcutaneous fat morphology can correlate with cardiovascular risk factors [37] and functional parameters of lipids are linked to insulin sensitivity and weight loss [38].

Second, tomographic approaches of OAI capitalize on ultrasound diffraction-limited resolution that is defined by the acoustic scattering of the tissue, which is about three orders of magnitude less than the optical scattering [75,76]. Therefore, the ratio of resolution-to-penetration depth is similar to that of purely ultrasound imaging techniques while the contrast is optical [76]. OAI modalities have achieved the resolution of 100 µm at several centimeters in depth [77], whereas decreasing the penetration depth to few millimeters the resolution can be improved to several micrometers maintaining the high depth-to-resolution ratio of approximately 200 [76,78]. Such scalability is extremely important to bridge the resolution gap and to achieve high resolution imaging through the whole skin depth [79]. Therefore, OAI can potentially be utilized to provide complete maps of skin structure and appendages at different skin depths down to subcutaneous tissue, including improved delineation of skin tumors and changes in microvascular morphology.

Third, skin chromophores express characteristic spectral signatures that can be probed over a broad electromagnetic spectral range [80]. OAI can take advantage of multi-wavelengths excitation to visualize hemoglobin, melanin, lipids, proteins, and water and to retrieve their relative concentrations. Discrimination of skin chromophores can allow monitoring of melanoma progression towards fat tissue that has been reported to trigger metastasis [13]. Moreover, low oxygen saturation of skin tissue can be associated with malignant skin tumors and promoting tumor growth [11,12].

Until today, there are numerous reports on utilizing OAI for skin imaging. Many of the developed setups share similar design that employ a single element detector, which is scanned over the region of interest, and illumination system for delivering the light to the tissue. Most of the employed detectors are based on the piezoelectric technology. However, there are several reports on the interferometric detection based on Fabry-Perot interferometric sensors making such OAI systems fully optical [81–83]. Besides, linear transducer arrays have been also considered for skin imaging by OA [84].

The first attempts to perform skin imaging using OA were carried out in 1999. The OAI system employed a piezoelectric transducer working in backward mode with 250 µm lateral resolution and 15-20 µm axial resolution at the depth down to 4 mm [85]. This work postulated the direction for improving skin imaging with OA technology by reducing lateral resolution of the employed detectors. Consequently, the next developed skin imager had significantly higher central frequency of 50 MHz denoting lateral resolution of 45 µm in the focus [86]. The system was able to deliver images of the resolved microvasculature of human skin as well as oxygenation parameters of the vessels. Despite promising results of the developed setups, translation of the OAI systems from bench to bedside were significantly limited by the repetition rate of the lasers, which did not exceed 10 Hz leading to long acquisition times of 50 min for an 8x8 mm^2 field of view. In clinical routine a long acquisition procedure may pose unwanted stress on the patient complicating the imaging. Besides, the imaged site of the body has to be fixed to avoid motion artefacts, which is not possible in the presence of breathing motion in abdominal area or back. Furthermore, imaging of physiological parameters such as heat induced hyperemia and oxygenation changes is often a rapid process that cannot be performed under the condition of long acquisition times. The reported bandwidth of the employed transducers (70%) allowed visualization of microvasculature located in the deeper dermis leaving aside imaging of the vessels located at the epidermal-dermal junction including the capillary loops.

Further development of the laser sources operating at repetition rates higher than 1 kHz led to substantially faster acquisition times [87]. Imaging at 561 and 570 nm has been used to assess relative oxygenation changes during 15 min in response to ischemic events, however, the analysis of the oxygenation changes was based on 2-dimensional scans rather than volumetric images [88]. Implementation of the Fabry-Perot interferometric detector in the optoacoustic imaging allowed monitoring of vasomotor circulatory changes in deep dermal vessels induced by thermal stimuli achieving only 100 µm lateral resolution [81]. Despite tremendous progress in imaging of skin microvasculature, the OAI systems mentioned above have failed to resolve skin structures, such as hair, sebaceous glands, subcutaneous fat, and water content. Multispectral optoacoustic tomography (MSOT) has demonstrated sensitivity to lipids associated with imaging hair follicles *in vivo* at 1300 nm [89] or subcutaneous adipose tissue in the human breast at 930 nm [90]. Nevertheless, MSOT achieves resolution in the 100-300 µm range, which is not optimal for skin imaging.

To summarize, skin imaging by means of OAI systems mentioned above has not fully addressed the imaging problem which is aimed to fulfil this resolution gap while preserving sufficient penetration to image through the whole skin depth [79]. To be more specific, employed detectors could not capture fine microvasculature at the epidermal-dermal junction; physiological imaging has been only performed on 2-dimensional images lacking volumetric information; the translation into the clinics is hampered by the size of the devices, while miniaturization is achieved at the expense of resolution and sensitivity; the number of imaged skin components has been limited to skin vasculature and melanin rich tumors.

1.3.2. RSOM in morphological and functional imaging (state of art)

In order to tackle these challenges, a raster-scanning optoacoustic imaging (RSOM) system was introduced and developed at the Institute of Medical and Biological Imaging, Helmholtz Zentrum, Munich, Germany [91]. The system enabled imaging of the mouse skin acquired in reflection mode employing a transducer operating at 98 MHz central frequency with 20-180 MHz bandwidth and achieving 18 µm lateral and 4 µm axial resolution [91]. The development of the handheld OAI system, termed Ultra-Broadband RSOM (UB-RSOM), showed unprecedented performance visualizing vasculature in the deep dermis and capillary loops located at the epidermal-dermal junction and melanin deposited in the epidermis [92]. UB-RSOM handheld device was reported to achieve 4.5 µm and 18.4 µm axial and lateral resolution, respectively. UB-RSOM helped to devise a new index of optoacoustic features (termed, OPIND) that provided quantitative analysis on severity of psoriatic plaques based on information extracted from volumetric optoacoustic images, e.g. epidermal thickness, blood volume, density and diameter of the capillary loops.

UB-RSOM images acquired *in vivo* are often deteriorated by the presence of various motion patterns including involuntary motion (muscle spasm, tremors, etc.) and motion caused by breathing. To compensate for the unwanted skin motion a correction algorithm based on skin surface tracking was developed [93]. The algorithm relied on the presence of melanin in the epidermis and showed 5-fold improvement in resolution comparing to non-corrected images. In order to compensate for site-specific skin displacement an automated motion correction algorithm was proposed [94]. The algorithm was based on site specific information about the motion which significantly improved the quality of the corrected images acquired from the back and other prone to motion body parts.

Improved performance and presented clinical value of UB-RSOM has enabled translation of the device into clinics where several studies addressing clinical questions have been performed. For example, UB-RSOM has been applied to measure systemic sclerosis-relevant biomarkers identified from volumetric images of the nailfold microvasculature [95]. Implementation of an optical parametric oscillator (OPO) showed that UB-RSOM has been able to retrieve the distribution of melanin in the epidermis and oxygenation of the dermal microvasculature [96].

1.4. Present challenges of 3D morphological and functional skin imaging

Assessment of the skin in dermatology heavily relies on inspection of skin palpation, odor and history of ones' diseases that significantly enhances diagnosis. However, visual inspection of the skin remains the main contributing factor to the decision making in dermatology [97]. Dermatoscopy has proved to increase the accuracy of skin cancer recognition by 50% comparing to an unaided eye [98], although suspicious lesions are still recommended to be inspected by histopathological analysis. In general, accuracy of diagnosis is dependent on the qualification of the dermatologist, which requires sufficient training. One of the main limitation of dermoscopic observation is lack of 3D and functional information. 3D images can help to identify the depth, boarders and a volume of the tumor [10], while assessment of hair follicles *in vivo* may be preferable in diagnosis of cutaneous lupus and alopecia areata [21]. Changes in microvascular function, such as blood flow and oxygenation on a single micro vessel level, can be associated with malignancy of skin cancers, or be a manifestation of cardiovascular and systemic diseases [24,25]. Such information is essential for disease diagnosis and development of therapeutic strategies and cannot be obtained via dermoscopy nor via histology. The shortage of complete information may lead to false diagnosis leading to increased burden on patients as well as medical cost.

	Contrast	Penetration depth, mm	Lateral resolution, µm	Axial resolution, µm	Field of view, mm^2	Imaging Speed
Reflectance confocal microscopy	Light reflection	0.2	1	2-5	0.5x0.5	30 fps [99]
Multiphoton microscopy	Light scattering	0.2	0.3	1	0.35x0.35	0.8 fps [100]
Raman microscopy	Inelastic scattering	0.15	1-5	1	0.25x0.25	10 min per 3D image [101]
Laser Doppler flowmetry	Dynamic light scattering by moving red blood cells	4.3 [59]	~1000	-	70x70	14 fps [102]
Laser speckle contrast Imaging	Dynamic light scattering by moving red blood cells	0.3	300 [103]	-	90x90	8 fps
High frequency ultrasound	Ultrasound reflection	10	200	20	6x12	1-8 fps [68]
Optical coherence Tomography	Low-coherent light reflection	0.4 mm for microvasculature	3-15	3-10	6x6	10 fps (FOV 1.2 mm^2) [104]
Raster-scanning optoacoustic mesoscopy	Light absorption	1.5 - 5	5	20	4x2	1 min per 3D image

Table 1 Technical characteristics of relevant methods used for skin imaging.

In Section 1.3 several imaging methods have been described that aim to aid diagnosis and prediction of skin conditions in dermatology, as well as to overcome/complement limitations of solely visual inspection of skin with an unaided eye or with dermatoscopy. The summary of technical characteristics of relevant skin imaging techniques is presented in Table 1. Despite the prominent optical contrast and high resolution of optical techniques, strong light scattering reinforced by the varying refractive indices of the skin layers significantly limits the penetration depth of RCM, MM, and Raman microscopy to few hundreds micrometers in skin. LDF and LSCI can capture bulk perfusion parameters of skin tissue but do not resolve single vessels. OCT was not able to resolve skin microvasculature thought the whole skin depth, while poor contrast of HFUS limits the differentiation of epidermal layers and cutaneous vessels.

UB-RSOM has been able to address many challenges of skin imaging posed by other techniques. For example, UB-RSOM has successfully visualized skin microvasculature and its oxygenation state, melanin layer in epidermis at high resolution through the whole skin depth. However, UB-RSOM imaging has been performed only in visible spectral range and was not able to capture skin structures rich with lipids and water. Functional information of microvascular oxygenation in skin has been retrieved only for one-time point, whereas physiological imaging often requires monitoring of rapid changes of blood volume and oxygenation state. Therefore, several challenges have to be addressed to improve performance of UB-RSOM in terms of morphological and functional skin imaging.

1.5. Objectives of the thesis

This thesis is focused on the further development of raster-scanning optoacoustic mesoscopy that aims to tackle present challenges and limitations of the techniques employed for skin imaging. The technical development herein is focused on the multi-wavelength implementation of the RSOM as well as its applicability to study hemodynamic processes. The achieved technological advances facilitate functional and morphological skin imaging in dermatology and relevant medical and biological fields. Thus, the objectives of the thesis can be presented as follows:

- **Development of a multiple laser optoacoustic mesoscopy system, including detectors, optics and software control that can achieve previously unmet capacity for multi-wavelength acquisition.**
- **Development of a method for robust monitoring of rapid blood volume changes caused by external stimuli in skin microvasculature at single-vessel resolution.**
- **Increasing the number of detected skin chromophores by state of the art ultra-wide spectrum and bandwidth RSOM system capable of acquiring signals at wavelengths from VIS to SWIR and of exploring the absorption properties of skin.**
- **Concurrent imaging of the main skin features *in vivo*: skin microvasculature, sebaceous glands, subcutaneous fat, the melanin layer, the whole hair, and water content.**
- **Development of a new method for monitoring fast oxygenation changes in skin microvasculature including capillaries (the smallest vessels in the human body).**

1.6. Outline of the thesis

It has been shown that RSOM has been able to tackle the resolution gap of skin imaging and to extract crucial biomarkers of psoriasis [79]. However, the further development and investigation of RSOM in clinical and pre-clinical settings are required in order to address present challenges of morphological and functional imaging of skin. Chapter 1 introduced the clinical importance of skin imaging and reviewed the currently developed techniques that try to solve the skin imaging problem and highlighted their limitations, while the outlined performance achieved by RSOM shows the direction for further development. The next six chapters of this thesis explain the advancements achieved in this work, which resulted in the great expansion of the abilities of the RSOM technique in the scope of morphological and functional skin imaging. Such new abilities enable measuring important medically relevant parameters that have not been accessible before.

Chapter 2 will give a brief introduction to the anatomy and function of skin which are essential for understanding the role of the imaged skin structures, their complexity in terms of molecular composition and functional responses of skin to external and internal stimuli. The optical properties of the skin are described with respect to the sources of contrast of optoacoustic mesoscopy and obstacles faced to achieve morphological and functional imaging.

Chapter 3 elaborates on the theoretical background of the optoacoustic signal generation, the acoustic and optical inverse problems, which are discussed in the scope of optoacoustic mesoscopy. Furthermore, the current developmental status of the raster-scanning optoacoustic mesoscopy system, which addresses the first objective of this thesis is presented. The technical advances of RSOM include **simultaneous operation and control of the optical parametric oscillator operating in the optical range from 420 to 2000 nm, two fast-repetition rate lasers operating at 532 and 515 nm, and implementation of 55 MHz and 24 MHz transducers**. Additionally, the fast reconstruction approach based on the universal back-projection formula, pre- and post-processing of the detected signal [105], will familiarize the reader with the steps required to improve image quality.

Chapters 4 to 6 are focused on the applications of the state of the art RSOM system, experimental aspects and results of morphological and functional imaging. **Chapter 4 describes the applicability of RSOM to the functional measurements of skin microvascular response to external stimuli** and addressed the second objective. The developed temperature control method allows robust and precise control over the thermal stimuli without interference with the imaging procedure. The results show prominent blood volume changes in skin bulk as well as vasodilation of single vessels through the whole skin depth. In Chapter 5, the performance of the ultra-wide spectrum and bandwidth RSOM system is studied in terms of visualization of skin chromophores in the optical spectrum from visible to short-wave infrared, which aim to address the third and the fourth objectives. The results suggest that the **UWSB-RSOM system is able to capture, hemoglobin, lipids, melanin, water, and lipids. Furthermore, the skin structures, such as dermal microvasculature, melanin layer, pilosebaceous unit, water content, and subcutaneous fat are concurrently imaged**. Finally, the multispectral RSOM system employing a 500 Hz OPO and the dual-wavelength RSOM for monitoring oxygenation changes in skin is presented in Chapter 6 and addresses the fifth objective. The microvascular responses to the VTP therapy in mouse skin and to the occlusion challenge in human skin are captured by DW RSOM in great detail. The conducted experiments highlight the capabilities of **optoacoustic mesoscopy to perform functional imaging of skin and visualize oxygenation in dermal microvasculature including capillary loops addressing the fifth goal of this thesis.**

2. Skin anatomy, functions and optical properties

2.1. Introduction

This chapter is dedicated to give a brief overview on the anatomy and function of skin and to elaborate on skin optical properties. The complexity of the skin in terms of multi-layered structure complemented with various skin appendages will be presented to lay out the imaging problem. The skin layers, epidermis, dermis, and hypodermis are segmented based on the approximate gradient of their structural composition, which also defines their unique optical properties. Skin functions are discussed in Section 2.2.3 to outline possible approaches for their assessment by optoacoustic imaging. The skin structures are identified to emphasize their involvement in certain skin functions and to draw the interest for their monitoring by functional optoacoustic imaging. The complexity of the skin optical properties is described in detail finally rendering the applicability of optoacoustic imaging to retrieve morphological and functional information.

2.2. Skin anatomy and function

The skin is the outermost organ of the human body covering from 1.2 to 2.3 m^2 and weighting from 3.5 to 10 kg. The multi-layered structure and complex functions of skin protect inner organs from harsh environmental conditions and intruding antigens, maintain temperature balance, provide sensory information and produce essential vitamins such as vitamin D.

2.2.1. Skin layers

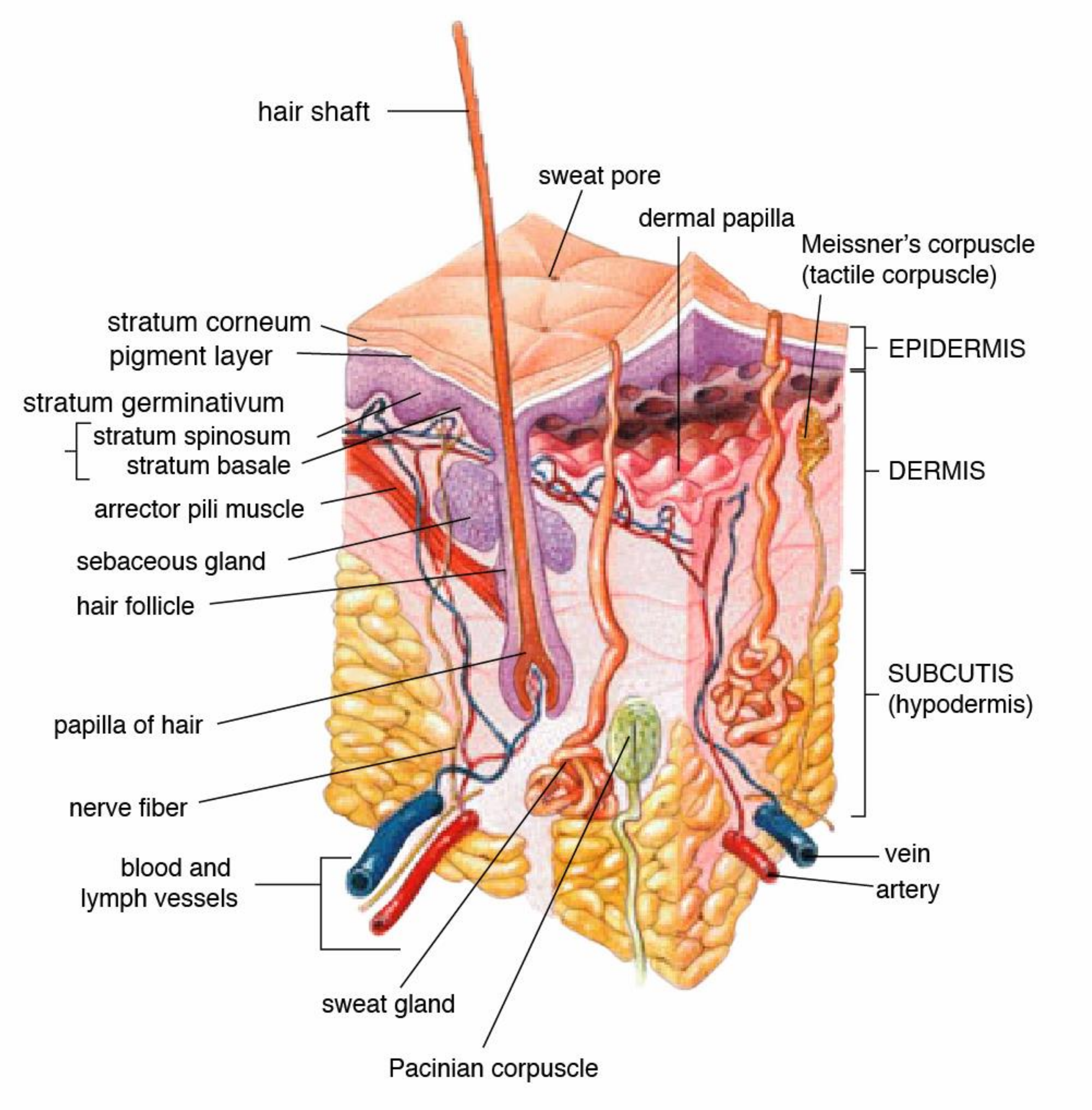

Figure 2.1. General structure of skin and skin layers by US-Gov (https://no.m.wikipedia.org/wiki/Fil:Skin.png) [Creative Commons BY-SA 3.0 (http://creativecommons.org/licenses/by-sa/3.0)], via Wikimedia Commons

In general, skin can be subdivided into three distinct layers: stratified bloodless epidermis, rich in microvascular network and connective tissue dermis and lipid-saturated hypodermis, which are depicted in Figure 2.1. At the epidermal-dermal junction, a 200 nm thin basement membrane supports epidermis and regulates cell traffic and transport of bioactive molecules [106]. The membrane plays an important role in healing of wounds and proliferation of cancer from epidermis to dermis.

The epidermis is composed mainly of keratinocytes corresponding to 95% of the contained cells, whereas the remaining 5% consist of melanocytes, Langerhans cells and Merkel cells. The epidermis is arranged in five layers: stratum corneum, stratum lucidum, stratum granulosum, stratum spinosum, and stratum basale (from outer surface inwards). stratum corneum is 20 µm thick and consists of dead keratinocytes, which have high lipid and protein content of ~20% and ~60% respectively [74]. The stratum basale is built up of brick-shaped keratinocytes, melanocytes of dendritic cell type, Langerhans and Merkel cells [107]. Keratinocytes proliferate to the skin surface and divide to terminal differentiation; melanocytes` main function is production of melanin pigment. The pigment is distributed to the neighboring keratinocytes to protect their nuclei from harmful ultra-violet radiation that can potentially destroy DNA of the cells, therefore, melanin has high absorption coefficient with a peak at around 350 nm [108]. Merkel cells play important role in sensory function and transmit information from skin to the nerves, while Langerhans cells are part of the immune system. The thickness of the epidermis ranges from 30-150 µm in hairy skin and reaching 600 µm glabrous (hairless) skin. The glabrous type of skin is characterized by the presence of sense organs within the dermis and by the lack of skin appendages such as hair follicles and sebaceous glands, while hair follicles and sebaceous glands can be found in abundance in hair-bearing skin, but encapsulated sense organs are missing [109].

The dermal layer is usually subdivided into the papillary dermis and reticular dermis. The papillary dermis is in direct contact with epidermis through the basement membrane and has extensive network of microvasculature and sensory nerve endings. The superficial microvascular network reaches up to 2 mm below the skin surface. The size of microvessells in the papillary dermis ranges from 10 to 35 µm making up from 2 to 4% of blood volume fraction in the skin [74]. At the dermal papilla nutritive capillary loops arise to the epidermal-dermal junction from a terminal arteriole and descend to connect to a post-capillary venule in the horizontal plexus. The vessels of reticular dermis range from 40 to 50 µm and are characterized by the presence of valves, which are involved in the forward pulsation of blood [110]. The dermis is mainly composed of connective tissue consisting of extracellular collagen and elastin fibers. Collagen is the main structural component of the dermis and corresponds to about 70% of dermis dry mass [107].

The hypodermis layer is characterized by a rich content of adipocytes arranged into fat lobules. Adipocytes vary in their diameter from 15 to 250 µm increasing in case of obesity. Subcutaneous layer may contain up to 80% of total fat content for lean individuals [107]. The thickness of subcutaneous adipose tissue has been reported to range from 1 to 17 mm in healthy individual and depends on the site of the body and gender [111]. The hypodermis structure is supported by fibrils stretching from the dermis to strengthen the connection between the layers. The metabolic function of subcutaneous fat is reinforced by the network of blood vessels and nerves passing through in the spaces between adipocytes [74].

2.2.2. Skin appendages

Human skin contains appendages that take part in certain skinfunctions, such as thermoregulation, protection from mechanical impact, sentience, as well as exocrine and immune functions.

The sebaceous glands are responsible for secretion of sebum to the skin surface and usually attached to the hair follicles. The sebum consists of a complex mixture of various lipids, such as squalene, glycerol, cholesterol and fatty acids, the main function of which is to sustain water balance in moisture loss and to protect skin from infection [112]. Sebaceous glands play an important role in the skin immune responses [113] and are known to have residing stem cells that are produced by sebocytes. However, the location of the stem cells and their molecular markers are not well defined [114]. The structure of sebaceous glands is represented by the multiple acinar components that converge towards excretory duct. In the mature state, the acinus of the glands is filled with lipid droplets and inversely proportional to the size of the adjacent hair [115].

The sweat glands are divided into eccrine and apocrine glands. They are located in dermis and total in 1.5 – 4 x 10^6 glands in a human body. In contrast to other appendages such as hair and sebaceous glands, the sweat glands are present in most of the parts of the human skin including palms of hands and soles of feet. The eccrine sweat glands realize thermoregulatory function by delivering water and hypotonic fluid to the surface of the skin where the water is evaporated cooling down the skin and blood in the dermis [116]. The secretory component of the eccrine glands is located in the deep dermis and surrounded by fat. Apocrine sweat glands are located mostly in the axillary and perineal regions and less numerous then eccrine glands. They produce protein-rich product that can develop odor when exposed to bacteria [116]. The sweat duct is a coiled structure that extends towards the epidermis where it is straightened [117].

The hair extends from the deep dermis or even subcutaneous fat to above the skin surface. The hair papilla located at the bottom of the hair is supplied with nutrients by the blood vessels. The arrector pili muscle is attached to the hair bulb at the base of the hair and is responsible for the "goose bumps" effect. Hair bulge is located on the side of the hair follicle and is known to conceal epithelial and melanocytic stem cells that give growth to hair follicles and sebaceous glands [107]. The hair color is defined by the melanin pigment and depends on the ratio of eumelanin and pheomelanin. The melanin accumulated in the hair is produced in the epidermis and the hair bulb [118]. The hair development is divided in three stages: anagen, catagen, and telogen. The active growth and pigmentation of the hair only occurs during the anagen phase, which can last up to 7 years. During the catagen phase hair structure undergoes several changes that mark the transition into telogen phase. In telogen phase, the hair is cornified and shed. Afterwards, the new group of cells descends to form a new hair [117].

The structure of the nail is similar to the hair and consists of a dense keratinized plate (nail plate) and a stratified squamous epithelium (nail bed). The nail is generated by the nail matrix, which consists of nerves, lymph and blood vessels and defines the size of the nail. The main function of the nails is to protect fingers' and toes' extremities and to enhance their sentience. The nail is often considered impenetrable, however, the nail permeability is higher than of the skin and therefore has to be taken into account when using cosmetics, transdermal drug delivery and working with aggressive chemicals [119].

2.2.3. Skin function

The function of skin is generally subdivided into following categories: barrier, temperature regulation, endocrine, immune, exocrine, and sentience. In order to execute its functions, the skin along with appendages is structured in a certain way to carry out multiple physiological processes. For example, the ability to withstand mechanical impact and prevent irreversible damage is owned to the rich composition of the skin with collagen and elastin. Collagen is a main component of the extracellular matrix accounting for more 70% of the skin's dry mass. It is characterized by great tensile strength that prevents skin from tearing and is critical for the attachment of the epidermis to dermis [120]. Another extracellular matrix fibrous protein is elastin. Elastin can be stretched by more than its full resting length and helps the tissue to restore its shape after mechanical impact. Subcutaneous fat functions as a physical barrier reduces impact on the muscle tissue and inner organs [121].

Permeability of the skin is controlled by the 15 µm thick epidermal layer called stratum corneum. The organization of the stratum corneum can be describe as “brick-and-mortar”, where “bricks” are dead corneocytes filled with filamentous keratin and “mortar” is lipids that regulate the permeability of the skin to avoid excessive loss of water or allow evaporative cooling when needed [122] [123]. Abnormal “mortar” lipid organization can be result of skin condition such as psoriasis, atopic dermatitis, and burns and, therefore, assessment of the transdermal water loss is of clinical interest [123].

Skin cancers are prevalent in light-skinned persons and exceed the occurance of other cancers [7]. The main cause of the skin cancers is excessive exposure to UV light. One of the mechanisms to prevent penetration of harmful UV radiation is production of melanin in the epidermis. The skin is classified in 6 photo-types from very light and sensitive (phenotype 1) to heavily pigmented and insensitive (phenotype 6) to UV light [124]. However, there is an indication of other mechanisms apart from melanin production to protect from UV light. For example, in people with vitiligo, increased expression of p53 tumor suppressor mechanism can decrease incidence of the non-melanoma cancer [125].

Immune function of skin is intrinsically intertwined with disruption of permeability barrier or mechanical barrier [126] [127]. Tape stripping of the stratum corneum is followed by the significant increase in density of the Langerhans cells (immune cells), while lower concertation of the immune cells in sun-exposed skin is compensated by the increase in the cell volume [128]. Furthermore, immune function of the skin is enriched by the fact, that Langerhans cells play crucial role in preventing HIV-1 from being transmitted to T-cells by capturing and degrading HIV-1 [129].

Excessive exposure to UV radiation can lead to decomposition of compounds crucial for reproduction system, such as vitamin B. In contrast, decreased production of vitamin D, which is involved in calcium metabolism, is associated with lack of sunlight. Therefore, adaptive evolution mechanism led to variation of pigmentation in humans located in parts of the world with different light exposure levels. Furthermore, depending on the period of the year, human skin developed the ability to vary the amount of melanin [130].

Skin thermoregulatory function is one of the main coping mechanisms to preserve the body core temperature within the limited window as a response to environmental temperature changes or internal temperature disbalance. Environmental thermal stress causes skin to change its temperature first, while the core temperature changes appear during endogenous thermal alterations. Temperature-sensitive neurons in the skin activate heat-conserving or -dissipating regulatory mechanism to maintain core temperature. The heat-conserving mechanism include cutaneous vasoconstriction and decrease of the blood flow that prevents heat dissipation from the surface of the body [34]. The heat-dissipating mechanism relies on vasodilation and increase of the blood flow of the skin microvasculature and sweat production through the sweat glands. The major contributor to the cutaneous vascular heat exchange is blood flow through the capillary loops located at the epidermal-dermal junction close to the skin surface [110]. It has also been reported that arteriovenous anastomoses located in deeper dermis is less crucial for the heat exchange, while it plays a major role in tissue viability during long cold exposure [131].

The change in the internal or external state of the organism is monitored by the somatosensory system. Thermoreceptors (temperature) are represented by the sensors that detect temperature changes and play an important role in maintaining core temperature of the body. Nociceptors (pain) respond to the potentially damaging stimuli such as excessive thermal or mechanical impact. Mechanoreceptors (preassure) are responsible for detection to pressure and vibration and enable fine motor control in the presence of various mechanical irritants from slow to fast [132].

2.3. Skin optical properties

As discussed in Section 2.2, skin is a multilayered highly heterogeneous organ consisting of many structures and appendages that are responsible for various skin function. The complexity of the skin defines its richness in molecules and morphological structures thereby determining its optical properties and characteristics. In the following section, the most dominant optical absorbers intrinsic to the skin are discussed and reviewed towards their utilization for OA contrast from VIS to SWIR. Furthermore, optical scattering, refractivity, and anisotropy of the skin are discussed with respect to their effects on OA imaging. While optical properties of skin can be estimated for certain conditions, they cannot be considered static [133]. Moreover, the results on the optical properties of the skin obtained *in vivo* and *ex vivo* often report different findings, therefore, have to be used with caution [80].

2.3.1. Absorption

The absorption coefficient describes the decrement of the light propagating through a light-absorbing medium per the distance:

$$\mu_a = -\frac{1}{T}\frac{\partial T}{\partial L} \qquad 2.1$$

where T (dimensionless) stands for the portion of the transmitted light through the length ∂L(cm), or commonly also referred as absorption. Therefore, the absorption can be expressed as:

$$T = e^{-\mu_a L} \qquad 2.2$$

Alternatively, the molar extinction coefficient (ε), which is intrinsic property of a chromophore, defines how strongly the light is attenuated for a certain chemical component at a particular wavelength and is measured in $cm^{-1}M^{-1}$:

$$T = 10^{-\varepsilon CL} \qquad 2.3$$

where C is the concentration in $mol \cdot L^{-1}$ or M. Therefore, the absorption coefficient expressed via extinction coefficient is:

$$\mu_a = \varepsilon \cdot C \cdot ln(10) \qquad 2.4$$

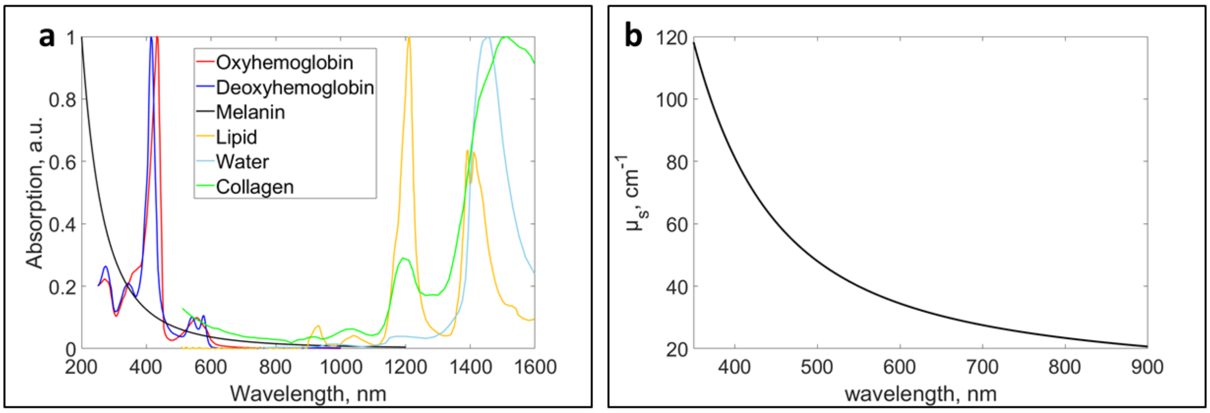

Figure 2.2. (a) Normalized absorption spectra of the main skin chromophores: oxy- and deoxyhemoglobin, lipids, water, and collagen. (b) Average scattering coefficient for skin plotted based on the Expression 2.5.

Skin chromophores can be uniquely identified from the measured signal based on their absorption spectra. In this work the visible, near infrared, and short-wave infrared range are explored in terms of optoacoustic imaging. The main absorbers, which exhibit high absorption in these spectral region, are melanin, hemoglobin, lipids, and water (Figure 2.2). In general, the absorption properties of skin vary per individual basis and the method used for their evaluation, thus, the estimation of the absorption spectra by different groups showed often a notable variance [133]. Furthermore, while the experiments performed *ex vivo* can provide more robust result on the skin absorption, the extraction and preparation of the samples may alter the spectral composition, e.g. by depleting the sample of water or blood.

One of the most prominent absorbers in the human skin are red blood cells (erythrocytes) that contain hemoglobin protein (HGb), with the fraction of only 0.2-4% in the dermal layer [74]. Hemoglobin is responsible for carrying up to four oxygen molecules bound to the heme complex and can exist in oxygenated (HbO_2) and deoxygenated state (Hb). The absorption spectrum of HGb changes when bound to O_2 (Figure 2.2a). The average Hb concentration in blood is often assumed to be around 150 g/l = 2.33×10^{-5} M, however can vary for men, women, and children [80]. It can be clearly seen that the absorption of blood is the strongest in the range from around 300 nm to 600 nm. In the NIR the absorption of hemoglobin is rather low with a slight increase at around 900 nm. The absorption spectra of hemoglobin are not presented in the SWIR in the Figure 2.2a due to very sparse and unreliable data [80]. Blood can be found in abundance in dermal layer, where dermal microvasculature forms several plexuses terminated by the capillary loops at the epidermal-dermal junction. The diameter of the vessels increases with depth from 6 µm and riches more than 100 µm for the vessels piercing the subcutaneous fat layer [134].

Melanin is a pigment that gives color to the skin and hair and represented by two monomers such as eumelanin and pheomelanin. Oftentimes, the spectrum of melanin layer in the skin described by the spectrum of melanosome, which, in principal, is a combination of eumelanin and pheomelanin. Therefore, another way to represent the melanin spectrum is via their respective extinction coefficients [80]:

$$\mu_{melanin} = \varepsilon_{eumelanin} C_{eumelanin} + \varepsilon_{pheomelanin} C_{pheomelanin} \qquad 2.5$$

where $\varepsilon_{eumelanin} = (2.37 \times 10^{4} cm^{-1} M^{-1}) e^{-0.0056\lambda}$ and $\varepsilon_{pheomelanin} = (1.01 \times 10^{5} cm^{-1} M^{-1}) e^{-0.0087\lambda}$, $C_{eumelanin}$ and $C_{pheomelanin}$ are concentrations of eumelanin and pheomelanin, respectively. The corresponding absorption spectrum of melanin derived from the power law is shown in Fig.1a, however, the approximation by the power law is reported to be unreliable for wavelength above 800 nm [135]. Eumelanin constitutes up to 90% of total melanin in the skin with concentrations of 5-40 mM, whereas the concentration of pheomelanin is 0.3-2.5 mM [136,137] in the stratum basale and decreases almost 10-fold towards the stratum corneum. The eumelanin concentration for different types of hair has been reported to lay in the range from 0.02 to 5.74 mg/mL, while the concentration of pheomelanin varies from 0.02 to 1.33 mg/mL [138].

Lipids can be found throughout the skin with the highest fraction of up to 86% (0.85g/g) in the hypodermis [139]. They also appear in dermis with the relatively stable fraction of 2-4%. Furthermore, the sebaceous glands and keratinocytes produce a complex mixture of lipids that is delivered to the surface of the skin [140]. The absorption of skin in the SWIR is attributed mostly to overtones of the stretching vibrational mode of the C-H bond in lipids, the N-H bond in proteins, and to the first overtone of O-H stretching in water and is shown in Fig.1a. for the NIR and SWIR [141,142].

The protein content in superficial and reticular dermis is primarily represented by collagen, hence, in many reports the protein spectra are specified for collagen with an absorption peak of 1.54 cm^{-1} at 1200 nm and of 5.22 cm^{-1} at 1510 nm [143,144]. The collagen dry fraction in skin has been reported to change with depth constituting concentrations in the range 2-4 µg/mm^{2} [144] (0.4-2.5 mg/ml [145]).

Water is the most abundant chromophore in human skin accounting for 70.2±5.2% on average in dermis and around 10% in hypodermis [146]. The water is distributed rather homogenously in dermis, whereas in the epidermis it is gradually increasing in its volume fraction from 30% in stratum corneum to almost 75% at the epidermal-dermal junction [147]. The absorption of water is negligible in visible range with a minor peak at around 960 nm in the NIR, and increases drastically in SWIR above 1400 nm dominating over the absorption of the other chromophores (Figure 2.2a) [142].

2.3.2. Scattering

The spatial distribution of light due to scattering is determined by the size of the scattering particles. It is generally accepted to define Rayleigh scattering as the scattering on particles roughly 10 times smaller than the wavelength of the scattered light. Rayleigh scattering is characterized as isotropic and weak compared to the scattering on the particles of the same order or larger than the wavelength. If the size of scattering particles considerably larger than the wavelength, the scattering is characterized as highly forward–directed and commonly referred as Mie scattering. Thus, longer wavelengths are more prone to the forward–directed scattering and exhibit greater imaging depth [133].

The main contributors to scattering in the skin are filamentous proteins: keratin in the epidermis and collagen in the dermis [74] [133]. The collagen fibers fluctuate in size with depth (100 nm in average), thereby, in the papillary dermis the small collagen fibers are highly backscattering, while deeper in the dermis the fiber bundles increase in size causing more prominent forward-scattering, thus “pushing” the light deeper into the skin. Since the skin contains both types of scatterers (smaller and larger than wavelength), it has been proposed to describe the scattering in the tissue by combining Mie and Rayleigh scattering and fitting the data from the multiple studies with the following empirical expression [80]:

$$\mu_s' = a'\left(f_{Ray}\left(\frac{\lambda}{500(nm)}\right)^{-4} + \left(1 - f_{Ray}\right)\left(\frac{\lambda}{500(nm)}\right)^{-b_{Mie}}\right) \qquad 2.6$$

where fitted parameters $a' = 48.0 \pm 10.6$ (cm^{-1}), $b_{Mie} = 0.702 \pm 0.351$, $f_{Ray} = 0.409 \pm 0.178$ represent the skin scattering, and $a' = 19.3 \pm 9.1$, $b_{Mie} = 0.447 \pm 0.263$, $f_{Ray} = 0.174 \pm 0.111$ are the average parameters for the tissue saturated with fat. The scattering coefficients reported for the fatty tissue depend significantly on the type of the connective tissue, which explains high standard deviation of the fitted parameters [148].

2.3.3. Refractive index

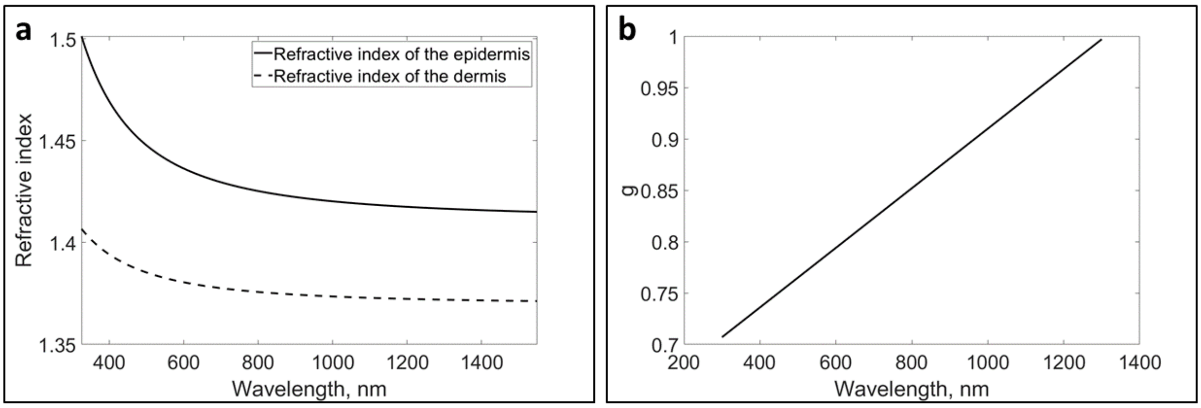

Figure 2.3 (a) Refractive index of skin; solid graph represents refractive index of the epidermis, dashed graph represents refractive index of the dermis. (b) Anisotropy factor of skin.

The refractive index of the material is a dimensionless number that defines the speed of light. Furthermore, the refractive index determines reflection and refraction of light at the boundary of two media, governs photon migration within the tissue [74]. In general, the variations in refractive index lead to light scattering, however, due to complexity of the modelling, refractive index and light scattering are often treated as independent variables. Furthermore, the refractive index is wavelength dependent. The actual estimation of the refraction index is complicated by the high heterogeneity of skin. It has been reported that the values for refractive indices of skin lay in the range between $n = 1.33$ (refractive index of water) and $n = 1.514$ (refractive index of dry tissue mass) [80]. It must be noted, that values of the refractive index in tissue acquired *in vivo* may fluctuate significantly from the values of *ex vivo* due to change in hydration of the sample. The refractive index of skin can be approximated assuming that the skin consists of 70% of water and 30% of proteins. It has been suggested to estimate skin refractive index by the following expression:

$$n_{skin}(\lambda) = 0.7(1.58 - 8.45 * 10^{-4}\lambda + 1.1 * 10^{-6}\lambda^2 - 7.19 * 10^{-10}\lambda^3 + 2.32 * 10^{-13}\lambda^4 - 2.98 * 10^{-17}\lambda^5) + 0.3 * 1.5 \qquad 2.7$$

with the assumption that the refractive index of protein is constant ($n = 1.5$) over the whole spectral range [149].

The refractive indices of fresh human dermis and epidermis were measured *ex vivo* at eight wavelengths in the range from 325 to 1550 nm using a reflectometer system [150]. To determine the actual refractive index for a given wavelength, the data were fitted into the Cauchy dispersion equation:

$$n_r = A + \frac{B}{\lambda^2} + \frac{C}{\lambda^4} \qquad 2.8$$

where $A = 1.4114$, $B = 8.73974 \cdot 10^3$ and $C = 7.9394 \cdot 10^7$ for epidermis; $A = 1.3696$, $B = 3.9168 \cdot 10^3$ $C = 2.5588 \cdot 10^3$ for the dermis (Figure 2.3a). Furthermore, it has been verified, that the stratum corneum, does not substantially affect the refractive index values, because of its relatively small thickness [150]. The higher A-value of the refractive index may be attributed to reduced concentration of water in the epidermis. In fact, the water content is the lowest in the stratum corneum (30%) increasing with depth to 75% at the epidermal dermal junction [147].

2.3.4. Anisotropy

The anisotropy factor defines the relation between light scattered in forward and backward direction and can be calculated from the scattering function [151]. Thus, the anisotropy factor values lay in the range from -1 to 1, where, -1 corresponds to the backward scattering, 0 is fully isotropic scattering and 1 is forward scattering. The estimation of the high values of anisotropy factor is impeded due to the fact that the most of the scattered radiation in skin is primarily in the range from 0 to 30 degrees [74]. In the skin, the anisotropy factor is defined by the orientation and size of the scatters, *e.g.* primarily collagen fibers in dermis and keratinocytes in the epidermis. An empirical formula has been proposed to estimate the anisotropy factor for dermis and epidermis in the range from 300 to 1300 nm [151]:

$$g_{epidermis} \sim g_{dermis} = 0.62 + \lambda \times 0.29 \times 10^{-3} \qquad 2.9$$

Figure 2.3b shows that the anisotropy factor of skin is 0.765 at 500 nm increasing for longer wavelengths and reaching 0.968 at 1200 nm, which characterizes more prominent forward scattering and may promote deeper penetration depth.

2.4. Conclusion

In this chapter, the anatomy, functions and optical properties of skin in scope of optoacoustic imaging have been introduced. The skin is subdivided into three distinct layers: epidermis, dermis and hypodermis. The epidermis is a bloodless outer layer consisting of brick-like keratinocytes, which proliferate toward the surface of the skin and transformed into corneocytes of the stratum corneum. The dermis is characterized by the presence of rich vascular network embedded into connective tissue. Sensory organs, sweat and sebaceous glands, hair follicles are also found in abundance in the dermal layer. Hypodermis consists mostly of fatty tissue with larger ascending arterioles and descending venules to provide nutrition to the upper layers of the skin and to carry out other vital functions. Skin appendages in human skin are pilosebaceous unit, which consists of sebaceous glands, hair, hair follicle and arrector pili muscle, sweat glands, and nail. The skin appendages are involved in skin functions, such as thermoregulation, protection from mechanical impact, sensation, and exocrine and immune functions. The barrier function aims to reduce mechanical damage to the skin, to retain skin permeability, to protect from harmful UV radiation, and to prevent pathogens from penetrating though the skin and infecting inner organs. Skin thermoregulatory function regulates body core temperature through various coping mechanism, which include blood flow and sweat. Endocrine function is responsible for production a vital vitamin D, which is produced as a result of exposure of the skin to the sun light. The nerve endings located in dermis are responsible for sensation of external stimuli that can be potentially dangerous and represent the sentient function of the skin.

The light absorption of skin is primarily governed by hemoglobin, melanin, lipids, proteins and water. The distribution of which can help to identify skin structures based on their molecular composition. For example, dermal microvasculature is filled with hemoglobin, while the stratum basale and hair can be recognized by the presence of melanin; the subcutaneous tissue is rich in fat content, whereas water accounts for almost 70% of the skin composition. The absorbers can be recognized based on their spectral characteristics. The absorption properties of the main skin chromophores are discussed for a broad optical range from VIS to SWIR, *e.g.* hemoglobin dominate in visible, while melanin absorption extends from visible to NIR; lipids, proteins, and water govern the absorption in SWIR. Anisotropy, refractivity, and scattering are intrinsically intertwined shaping the light fluence in tissue, which is particularly important for quantitative imaging [152].

3. Background Methodology of RSOM

Section 3.5 contains adapted text passages and figures from the publication by Berezhnoi and Aguirre et al. [2] © 2019 OSA Publishing.

More information on the permission to reproduce textual material and illustrations can be found in appendix B.

3.1. Introduction

This chapter is dedicated to give a brief introduction to basic principles of optoacoustic imaging and to outline acoustic and optical inverse problems in scope of optoacoustic mesoscopy. Furthermore, ultra-wideband spectrum and bandwidth RSOM instrumentation, signal preprocessing, and a reconstruction method are discussed to present the operation principles of the technique. The developed technique and methods are utilized to address the challenges of morphological and functional skin imaging introduced in Section 1.4. The presented instrumentation evolved from an early version of the RSOM setup [153] and later developed single-wavelength handheld extension of the modality [92].

3.2. Principles of optoacoustic signal generation

As it has been previously mentioned in Section 1.3.1, the optoacoustic modalities operate capitalizing on the photoacoustic effect, which involves a local pressure increase in response to the absorbed non-ionizing electromagnetic energy. The localized pressure perturbations induce an ultrasound wave propagating in the elastic tissue. Upon the light absorption, de-excitation of the absorbing molecules results in the initial fractional volume expansion dV/V of the tissue and can be expressed as a function of pressure and temperature changes:

$$\frac{dV}{V} = -\kappa \Delta p(\vec{r}) + \beta \Delta T(\vec{r}), \qquad 3.1$$

where $\kappa = -1/V(\delta V/\delta P)_T$ denotes the isothermal compressibility, and $\beta = -1/V(\delta V/\delta T)_P$ stands for the isobaric coefficient of the thermal volume expansion [154]; $p(\vec{r})$ and $\Delta T(\vec{r})$ are localized pressure (Pa) and temperature changes (K), respectively. The isothermal compressibility in biological tissue can be described as

$$\kappa = \frac{C_P}{\rho v_s^2 C_V}, \qquad 3.2$$

where C_P is a heat capacity at constant pressure and C_V is a heat capacity at constant volume ($J/kg \cdot K$); ρ and v_S denote the mass density(kg/m^3) and speed (m/s) of a propagating acoustic wave, respectively. The thermal expansion coefficient varies depending on the material, can change as a function of temperature and is found to be around $\beta = 10^{-4}/°\mathrm{C}$ in skin at 37℃ [155].

The initial pressure change $\Delta p(\vec{r})$ that is generated in response to absorbed light energy is maximized when the conditions of thermal and stress confinements are met [156]. The thermal confinement relates to the thermal diffusivity of the tissue and requires the duration of the eliminating light pulses to be shorter than the time scale of the heat dissipation (the thermal relaxation time):

$$t_{th} = \frac{d^2}{D}, \qquad 3.3$$

where, d is the characteristic length (m) of the heated tissue volume and D is the thermal diffusivity of the tissue.

In similar manner, the mechanical confinement determines the width of the light pulse that has to be shorter than the stress propagation of the heated volume. The time that is required of the stress to propagate in the heated volume is called stress relaxation time and can be expressed as follows:

$$t_s = \frac{d}{v_S}, \qquad 3.4$$

where v_S is speed of sound in the heated tissue (m/s) and d, similar to expression 3.3, is the characteristic length of the heated tissue volume (m).

Thermal diffusivity of water is in the range from $0.14 - 0.15\ mm^2/s$, thus, the thermal relaxation time for a sphere with 10 μm diameter is $t_{th} = 10^2/0.14 = 714\,\mu s$. Similarly, the stress relaxation time can be evaluated taking $v_S = 1500\ m/s$,which is typical for water, and $d = 10\,\mu m$, as a result $t_s = 10\,\mu m/1500\ m/s = 6{,}7\,ns$ [157].

Illuminating absorbers with the sufficiently short light pulses that meet thermal and mechanical confinements, the partial volume's change in the Expression 3.1 can be neglected. Therefore, the initial pressure change can be expressed as:

$$\Delta \mathrm{p}(\vec{r}) = \frac{\beta \Delta T(\vec{r})}{\kappa}. \qquad 3.5$$

Assuming that all the deposited energy is transferred into the temperature increase and other non-thermal relaxation, e.g. fluorescence, can be omitted, the localized temperature change can be expressed as:

$$\Delta T(\vec{r}) = \frac{\mu_a(\vec{r})\phi(\vec{r}, \mu_a, \mu_s, g)}{\rho C_V}, \qquad 3.6$$

where the $\phi(\vec{r}, \mu_a, \mu_s, g)$ is the light radiance integrated over all directions and time, also known as the light fluence (W/cm^2); μ_a – absorption coefficient, μ_s- scattering coefficient, and g-

anisotropy factor, which were described in detail in Section 2.3. Substituting ΔT in (3.5) from the Equation 3.6 leads to the initial pressure change expressed as:

$$\Delta \mathrm{p}(\vec{r}) = \frac{\beta \mu_a(\vec{r}) \phi(\overrightarrow{r}, \mu_a, \mu_s, g)}{\kappa \rho C_V} = \frac{\beta v_s^2 \mu_a(\vec{r}) \phi(\overrightarrow{r}, \mu_a, \mu_s, g)}{C_P} = \Gamma \mu_a(\vec{r}) \phi(\overrightarrow{r}, \mu_a, \mu_s, g), \qquad 3.7$$

where Γ is the dimensionless Grüneisen parameter, which describes the efficiency of photoacoustic effect.

3.3. Acoustic forward problem

In case of the elastic and inertial tissue, the initial localized pressure change $\Delta p(\vec{r})$ provokes an acoustic wave, for which, the propagation in a homogeneous liquid medium can be described by the initial value problem and is formulated as follows:

$$\begin{gathered}(v_s^2\nabla^2 - \frac{\partial^2}{\partial t^2})p(\vec{r},t) = 0,\\ p_0(\vec{r}) = \Delta p(\vec{r}) = \Gamma\ (\vec{r})H(\vec{r}) - first\ initial\ condition,\\ \left.\frac{\partial p(\vec{r})}{\partial t}\right|_{t=0} = 0 - second\ initial\ condition,\end{gathered} \tag{3.8}$$

where $H(\vec{r},t)$ - is the absorbed energy density (Jm^{-3}). The first initial condition relates to the presence of sources for optoacoustic wave generation, while the second initial condition indicates that the velocity of particles is zero at $\mathrm{t} = 0$. Therefore, the optoacoustic wave generation and propagation obeys the following equation:

$$\frac{\partial^2 p(\vec{r},t)}{\partial t^2} - v_s^2\nabla^2 p(\vec{r},t) = \Gamma\frac{\partial\Gamma\mu_a(\vec{r})\phi(\vec{r},\mu_a,\mu_s,g,t)}{\partial t} = \Gamma\frac{\partial H(\vec{r},t)}{\partial t}. \tag{3.9}$$

It can be noted, that the right side of the Equation 3.9 contains the derivative of the absorbed energy density, often referred as the heating function, which leads to the conclusion that only upon the time varying excitation the optoacoustic signal can be generated.

In order to find the solutions to the linear differential equation describing the propagation of the optoacoustic wave in the inhomogeneous media (Equation 3.9), the Green's function can be used. In general, the Green's function can be described as the response of a linear differential operator to a delta function:

$$(\nabla^2 - \frac{1}{v_s^2}\frac{\partial^2}{\partial t^2})G(\vec{r},\vec{r}',t,t') = -4\pi\delta(\vec{r}-\vec{r}')\delta(t-t'), \tag{3.10}$$

where $\vec{r}'$ is the position of the point source of the acoustic wave and t' is the time of initial pressure rise. Therefore, the solution to the equation (3.10) is:

$$G(\vec{r},t,\vec{r}',t') = \frac{\delta(\mathrm{t}+\frac{|\vec{r}-\vec{r}'|}{v_S}-t')}{|\vec{r}-\vec{r}'|}. \tag{3.11}$$

Physically, the Green's function defined in the Equation 3.11 describes a spherical wave, which originates at a position $\vec{r}$ and time t and propagates decreasing in the amplitude with distance. Now, the general solution for the acoustic wave propagating in homogeneous media (3.9) can be derived using the solution obtained for the Green's function in the Equation 3.11:

$$p(\vec{r},t) = G(\vec{r},t) * \left(-\frac{\Gamma}{v_s^2}\frac{\partial H(\vec{r},t)}{\partial t}\right) =$$

$$\frac{\Gamma}{4\pi v_s^2}\iiint d\vec{r}' \int dt' \frac{\delta\left((t-t')-\frac{|\vec{r}-\vec{r}'|}{v_S}\right)}{|\vec{r}-\vec{r}'|}\frac{\partial H(\vec{r}',t')}{\partial t'} = \frac{\Gamma}{4\pi v_s^2}\iiint \frac{d\vec{r}'}{|\vec{r}-\vec{r}'|}\frac{\partial H(\vec{r}',t')}{\partial t'}\bigg|_{t'=t-\frac{|\vec{r}-\vec{r}'|}{v_S}}. \qquad 3.12$$

Since the heating function is considered to comply with the thermal and mechanical confinements, and the speed of light is assumed instant in comparison to other physical processes that take place in generation and propagation of the optoacoustic waves, the heating (source) function $H(\vec{r}',t')$ can be represented as a multiplication of two functions $H(\vec{r}',t') = H(\vec{r}')H(t')$. Taking into account the first initial condition in (3.8) and considering $H(t')$ an instant heating function (ultra-short light pulse), $H(\vec{r}',t')$ can be expressed as:

$$H(\vec{r}',t') = \delta(t')\frac{\Delta p(\vec{r}')}{\Gamma} = \mu_a(\vec{r}')\phi(\vec{r}',\mu_a,\mu_s,g)\delta(t'). \qquad 3.13$$

The solution for the acoustic wave propagation from (3.12) is modified by substituting $H(\vec{r}',t')$ with right part of the Equation 3.13:

$$p(\vec{r},t) = \frac{\Gamma}{4\pi v_s^2}\iiint \frac{d\vec{r}'}{|\vec{r}-\vec{r}'|}\mu_a(\vec{r}')\phi(\vec{r}',\mu_a,\mu_s,g)\frac{\partial\delta(t')}{\partial(t')}\bigg|_{t'=t-\frac{|\vec{r}-\vec{r}'|}{v_S}}. \qquad 3.14$$

The Equation 3.14 describes the acoustic wave generated through the photoacoustic effect and propagating in the tissue. The bipolar N-shaped pressure signal is attributed to the time derivative and can be explained as a converging spherical wave propagating through the center of the source and diverging after. Therefore, the width of the pulse will be determined by the size of the absorber, while the amplitude of the propagating acoustic wave is proportional to the light absorption coefficient and fluence (μ_a, ϕ) and is inversely proportional to the distance from the source.

3.4. Image formation

The optoacoustic tomography (OT) capitalizes on acoustic resolution imaging and allows visualization of the chromophores up to few centimeters deep in tissues. Usually, detection schemes include 1- or 2-demensional arrays of the detectors or, alternatively, a single detector scanned over a surface. Conventionally, the detectors utilized in the OT are based on the piezoelectric crystals, however, the detectors based on polyvinylidene difluoride (PVDF) or interferometric sensors have also been considered for optoacoustic imaging [158,159]. The OT, ultimately, targets to achieve quantitative imaging of the 2- or 3-dimentional distribution of tissue chromophores based on the detected optoacoustic signals [160]. Hence, in terms of skin imaging, mapping the tissue chromophores can help do identify skin structures and retrieve information about functional parameters, as it has been discussed in Chapter 2 and will be further studied in Chapters 4-6 [96]. Essentially, challenges of the quantitative imaging with OT can be split into 2 problems: acoustical inverse problem and optical inverse problem.

3.4.1. The acoustic inverse problem

The acoustic inverse problem relates to mapping (reconstructing) the positions of the chromophores/absorbers in the tissue from the detected acoustic signals [161], which can be achieved by inverting the Equitation 3.14 and retrieving $\Gamma\mu_a(\vec{r}')\phi(\vec{r}',\mu_a,\mu_s,g)$. In general, the solutions to this problem are challenged by system design, acoustic properties and inhomogeneities of the probed tissue. For instance, the real tissue is characterized by the inhomogeneous density and varying speed of sound, which, if not taken into account, may lead to the incorrect mapping of the sources of the optoacoustic waves. Furthermore, frictional losses in tissue and heat diffusion may lead to the frequency-depended attenuation of acoustic waves propagating in tissue, which is estimated to be $0.75\,dB/(cm\cdot MHz)$ for soft tissue. The frequency-dependent attenuation can be particularly prominent in mesoscopic application operating in ultra-wide bandwidth 10-200 MHz, due to narrowing of the bandwidth of the generated optoacoustic signal, which may lead to smearing of the visualized features and general distortion of the images at depth [162]. It has been shown, that accurate reconstruction of the tissue absorbers requires that the imaged object is fully enclosed, meaning that the generated optoacoustic signals are detected from all the directions [163]. However, in real-life scenario the full coverage of the imaged object is not possible due to practical limitations, such as size and geometry of the object. Therefore, most of the optoacoustic imaging systems use limited-view detection schemes, which encompass only partially the imaged object leading to incomplete acquired data and distortion of the images [164].

In order to achieve precise reconstruction of the optoacoustic images, more realistic tissue properties and the geometry of the detection schemes must be taken into account [165,166]. Many reconstruction approaches have been developed for ultrasound and computed tomography, which allowed adoption of reconstruction algorithms at early development stage of OT [167]. However, fast advancement of the OT technique incorporating various geometries of the detectors as well as unique reconstruction challenges attributed exclusively to OT, such as propagation of the broadband optoacoustic waves in tissue and their diffraction, led to the rise of new computational approaches intending to solve the acoustic inverse problem. The acoustic inverse problem can generally be divided into following categories: time-domain algorithms, frequency-domain algorithms, time-reversal approach, and model based algorithms [161].

3.4.2. The optical inverse problem

The next step in achieving quantitative optoacoustic imaging consists in retrieving the absorption coefficients assuming that the initial pressure distribution are recovered precisely and the optoacoustic imaging system is calibrated, so that $p_0(\vec{r}) = \Gamma\,(\vec{r})H(\vec{r})$. In order to estimate the absorbed optical energy density $H(\vec{r})$, the reconstructed initial pressure distribution cannot be simply divided by the Grüneisen parameter $\Gamma\,(\vec{r})$, since the Grüneisen parameter is spatially varying and depends on the tissue properties, such as specific heat capacity C_p and volume thermal expansivity β. For example, the Grüneisen parameter of the fat is $\Gamma \approx 0.9$, while for blood it is just 0.25 [168]. Therefore, the known values of the Grüneisen parameter for different tissue types are crucial to achieve the quantitative optoacoustic imaging.

The optical inverse problem in optoacoustic imaging consists in finding the concentrations of the chromophores $c_n(\vec{r})$ with known extinction coefficient spectra $\alpha_n(\lambda)$ from the measured absorbed optical energy density (the deposited heat energy) $H(\vec{r})$, and can be formulates as

$$H(\vec{r},\lambda) = \phi(\vec{r},c_n,\mu_s,g,\lambda)\mu_a(\vec{r},\lambda) = \phi(\vec{r},c_n,\mu_s,g,\lambda)\sum_{n=1}^{N} c_n(\vec{r})\alpha_n(\lambda), \qquad 3.15$$

where $\phi(\vec{r},c_n,\mu_s,g,\lambda)$ – is the light fluence. The absorption coefficient $\mu_a(\vec{r},\lambda)$ is linearly mapped to the concentrations of the N chromophores $c_n(\vec{r})$, therefore the concentrations can be retrieved if the absorption coefficient is known at least for N wavelengths. In order to recover concentrations of the chromophores from the measured optoacoustic data, it is appealing to assume that the light fluence is known as well and the absorbed energy density $H(\vec{r})$ is a linear function of the chromophore concentrations. If this was true, the chromophore concentrations could be recovered using a linear matrix inversion. However, the light fluence depends on the concentrations of chromophores as well as spatially dependent optical properties of the tissue in a non-linear way, therefore it cannot be in general assumed that $H(\vec{r},\lambda)$ is linearly proportional to $c_n(\vec{r})$ [152]. Furthermore, the decrease in the absorption coefficient at a certain location will lead to the reduced absorbed energy in that location, therefore, the light fluence will increase in the proximity to that region. However, the scattering coefficient can change in such a way, that it will compensate the change of the light fluence leading to increased absorbed energy $H(\vec{r})$. This example demonstrates that different values of tissue optical properties may lead to several solutions making the problem of retrieving the chromophore concentrations ill-posed. In some simple imaging scenario when a homogeneous and non-scattering media are considered, the unknown light fluence can be estimated analytically. However, under real imaging conditions, numerical models are required to describe the light propagation in the tissue [152]. Alternatively, it has been suggested to represent the fluence as a set of spectral base function circumventing the need for *a priory* knowledge on the optical properties of tissue, which led to more accurate estimation of oxygenation parameters deep in tissue by MSOT [169].

3.5. UWSB RSOM instrumentation

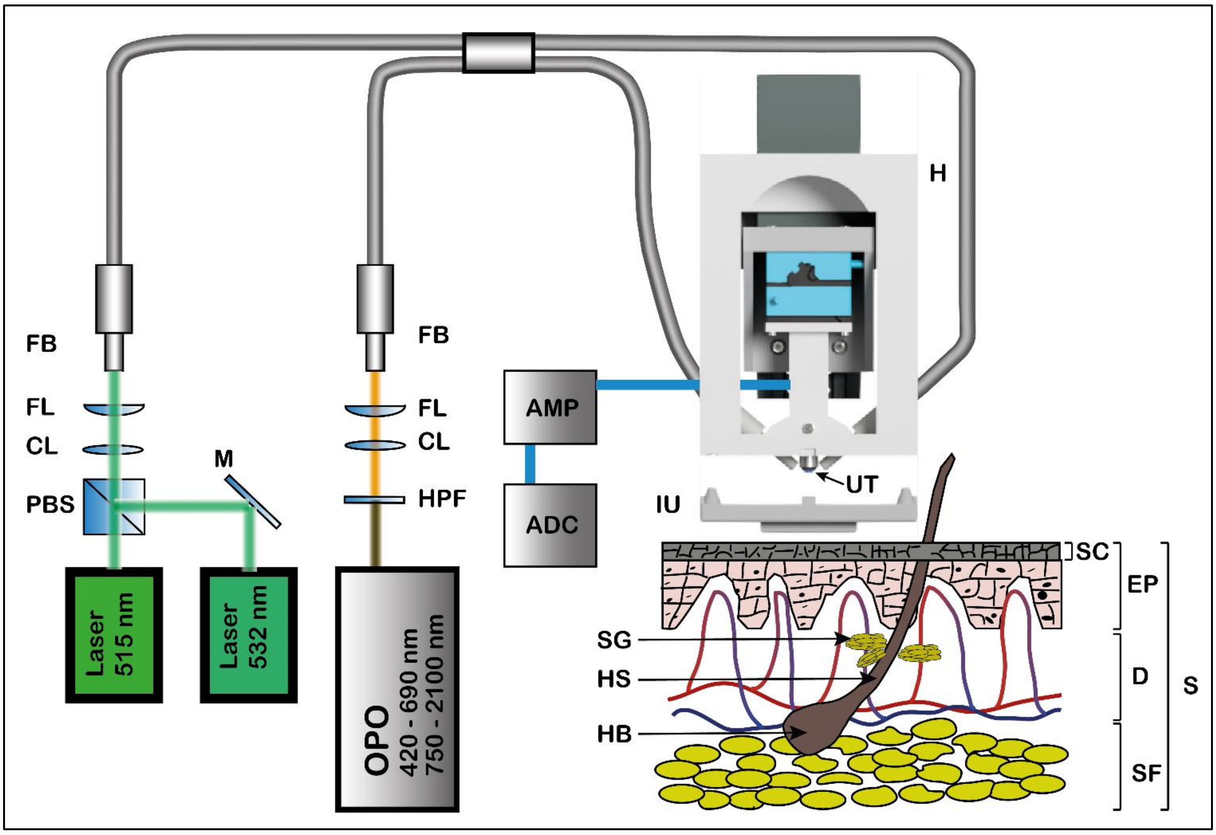

Figure 3.1 Schematic of UWSB RSOM. Abbreviations: ADC – analog-to-digital converter, AMP – 60 dBm amplifier, CL – collimating lens, D – dermis, EP – epidermis, FB – fibre bundle, FL – focusing lens, H UWSB RSOM holder, HPF – high-pass filter, HS – hair shaft, HB – hair bulb, IU - detachable interface unit, M -mirror, PBS-polarizing beam splitter, S – schematic of human skin, SF – subcutaneous fat, SG – sebaceous glands, UT – ultrasound transducer. Adapted from Berezhnoi et el. [2] © 2019 OSA Publishing. Reproduced with permission.

Figure 3.1 and illustrates the main components of the UWSB RSOM system developed in this work. The optoacoustic signals are generated by illumination of the tissue with up to 120 µJ high energy nanoseconds light pulses. Depending on the imaging problem, different light sources or combinations of the light sources can be used. The diode pumped high energy solid state Nd:YAG laser emits nanosecond laser pulses to optical parametric oscillator (SpitLight OPO, InnoLas Laser GmbH, Krailling, Germany), which achieves tunable light pulse generation in the range from 420 nm to 690 nm (signal), and from 730 nm to 2000 nm range (idler). The width of the emitted light pulses is 6 ns at a repetition rate of 100 Hz.

Alternatively, the OPO (SpitLight DPSS EVO 200 OPO, InnoLas Laser GmbH, Krailling, Germany) operating at 500 Hz repetition rate was implemented for the mouse experiments. The tunable range of the 500 Hz OPO is from 410-2500 nm. Light sources based on OPOs can generate high energy nanoseconds pulses at wavelengths, that can be tuned in a broad spectra range, however, the repetition rates above 100 Hz of the OPOs inflict special requirements on the acquisition procedure. The OPOs are susceptible to high per pulse energy fluctuations. A rotating non-linear optical crystal, which serves to tune an emitted optical wavelength, is prone to mispositioning at high repetition rates leading to even stronger fluctuations of the energy, especially when the scanned wavelengths are far apart spectrally. In order to overcome these challenges, the energy fluctuations are mitigated, first, by implementing wavelength tuning for each 2-dimensional scan (B-plane), second, by recording energy values of each pulse with a photodiode. Tuning wavelength per B-plane instead of per pulse helped to avoid mispositioning of the crystal and, therefore, to significantly reduce fluctuations of the energy. Furthermore, the acquired data were corrected by the pulse energies recorded with a photodiode.

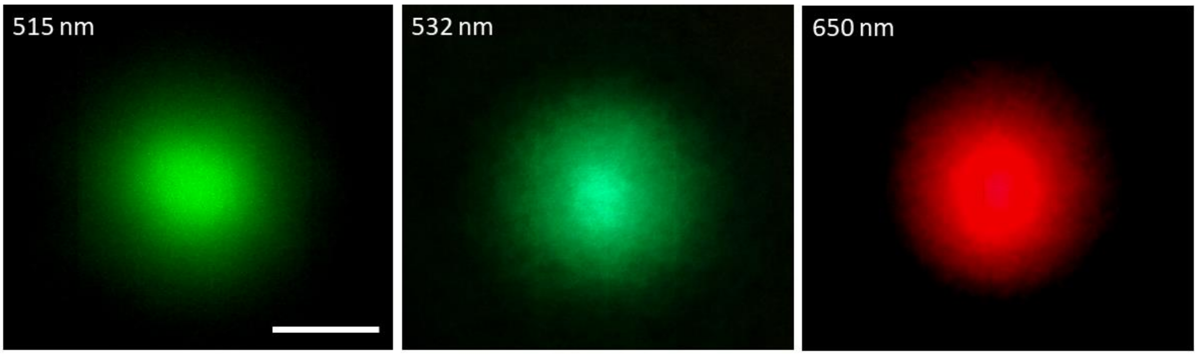

Figure 3.2 Illumination pattern at the output of the fiber bundles for the three wavelengths, each of them corresponding to a different laser source. Scale bar 5 mm.

To achieve fast acquisition times, the system incorporates two fast single-wavelength lasers: Wedge HB.532, Bright Solutions, Pavia, Italy; Flare NX 515-0.6-2, Coherent, Germany). The laser operating at 532 nm has a pulse width of 0.9 ns and a tunable repetition rate of up to 10 kHz, while the 515 nm laser achieves tunable repetition rate of up to 2 kHz with 1.2 ns pulse width. The triggering of the fast single-wavelength lasers was controlled by the piezoelectric stages (M683, Physik Instrumente, Karlsruhe, Germany), which were programmed to generate a trigger signal each time reaching certain positions along fast-scanning axis. The trigger signal was sent to trigger the 532 nm laser and to an arbitrary waveform function generator. The function generator produced another trigger signal delayed by 250 µs to the initial trigger event and sent to the 515 nm laser. Thus, the generated interleaved light pulses were 250 µs apart.

The light delivery to the imaged region was achieved via a custom-made fiber bundle (CeramOptec, Riga, Latvia). The fiber bundle is a 2×2 beam splitter, which allows coupling of the fast single-wavelength lasers into one of the inputs of the fiber bundle, while the OPO is coupled into another input. In this work the fast lasers are mainly used for imaging of fast changing parameters such as vasodilation and oxygenation changes induced by external stimuli by allowing scanning the region of interest (4×2 or 4×1 cm^2) in less than one minute (40-60 s). In principle, all three laser sources can be used during a single acquisition procedure. The illumination is co-aligned by the two outputs of the fiber bundle and appears as a spot characterized by the Gaussian profile 100 µm below the focus of an installed transducer (Figure 3.2). The diameter of the illumination is approximately 5 mm so that the sensitivity field of a transducer is filled with diffuse light and the fluence distribution depends only on the optical properties of the illuminated tissue. It must be noted, that for the *in vivo* experiments the maximum output energy delivered to the surface of the skin via the fiber bundle did not exceed safe exposure limits 20 mJ/cm^2 , which are defined for human skin [170].

The detection of broadband optoacoustic signals is achieved utilizing spherically focused piezoelectric transducers. For most of the performed experiments two spherically focused piezoelectric transducers are employed. One transducer is made of lead zirconate titanate (24 MHz, Sonaxis) and has a central frequency of 23.9 MHz with a bandwidth of 15.5-32.3 MHz and a 6 mm focal distance. The focusing of the 24 MHz transducer is attained by a curved sensing area. Another transducer has a central frequency of 55 MHz with a bandwidth of 14-114 MHz and a focal distance of 3 mm, which is achieved by an acoustic focusing lens, and is also made of lead zirconate titanate (55 MHz, Sonaxis, Besancon, France).

The axial and lateral resolution of the 24 MHz transducer were calculated as a half-width half-maximum of a measured 10 µm diameter surgical suture constituting 33 µm and 53 µm, respectively. The theoretical axial resolution can be calculated using the following expression [171]:

$$AR = 0.6\frac{c}{f}, \qquad 3.16$$

where AR denotes the axial resolution, c is the speed of sound (1520 m/s), f is the frequency, therefore for 32 MHz frequency the axial resolution is equal 28.5 µm. The theoretical lateral resolution of 48.5 µm is determined as follows:

$$LR = 1.02 \cdot \frac{F \cdot c}{f \cdot D}, \qquad 3.17$$

where LR – lateral resolution, F – focal length (6 mm), c- speed of sound (1520 m/s), f-frequency (32 MHz), D – element diameter (6 mm). The measured axial and spatial resolution for 55 MHz transducer are 8.6 µm and 29.6 µm, respectively, while their theoretical values calculated using the Equations 3.16 and 3.17 are 7.6 µm (axial) and 13.6 µm (lateral).

In order to perform tomographic imaging, a transducer and fiber bundles are scanned concurrently so that the center of the illumination patter is always slightly below the focal point of the transducer. The scanning is performed by using high precision piezoelectric stages (M683) in a 2-dimensional raster-scanning manner. The scanning is done in “snake-manner” and can be described as follows: the transducer and the fiber bundles are scanned along x-axis (fast axis) continuously, when a limit position of the fast axis is reached, the position along y-axis (slow axis) is shifted by a pre-defined step size, so that the region of interest at the end of the acquisition is covered. The step size for each of the axes is set to be at least two times smaller than the lateral resolution of the employed transducer in order to satisfy the Nyquist-Shannon sampling criterion, meaning that the temporal sampling and spatial sampling must be at least 2 times higher than the largest detected frequency. In terms spatial sampling, for the 55 MHz transducer, the selected step size is 15 µm, while for 24 MHz transducer it is 20 µm. The lasers are actively triggered by the stages at each position of the fast axis generating excitation pulses that induce optoacoustic signals. The recorded signals at each position are referred as A-lines and represent 1-dimensional time signal. The set of A-lines recorded along the fast axis are called a B-plane.

The detected optoacoustic signal is amplified using a low-noise amplifier (AU-1291, MITEQ, Hauppauge, New York, USA). The low-noise amplifier with a 63 dB amplification, a noise figure of less than 1.4 dB, and a 0.001-500 MHz bandwidth is crucial for optoacoustic imaging, since such amplifier exhibits amplification of the weak and broadband optoacoustic signals while preserving low additive noise.

Amplified analog signals are digitized by a digital acquisition card (DAQ; EON-121-G20; Gage Applied Technologies, Montreal, Canada) with a sampling rate of 1 GS/s. The sampling rate is selected in order to satisfy the Nyquist-Shannon sampling criterion as described above. However, for the finite number of samples and non-ideal low pass filtering, the oversampling of the acquired data is usually performed with a factor 2 or 4. Taking into account the highest frequency of the 55 MHz transducer (114 MHz), the sampling frequency has to be above $f_{samp} = 502\ MHz$. Therefore, in this case the sampling frequency of the DAQ was set to 1 GS/s. The triggering of the DAQ is achieved by capturing approximately 5% of energy of the generated light pulses. Each light pulse is detected by a photodetector and transmitted to the trigger input of the digitizer initiating acquisition of the corresponding time signal. The length of the recorded A-lines (1300 to 3300 samples at GS/s repetition rate) is determined by the required imaged depth, which usually is 2-5 mm.

The fiber bundle outputs, transducer, and moving stages are enclosed in a compact 3D-printed scanning head made of polylactic acid material (Figure 3.1). The scanning head is connected to an articulated arm (Noga, Israel) for free-movement positioning. The interface unit (IU) is detachable and is affixed to the scanning head using magnets. Such design allows easy and precise positioning of the small and lightweight IU on the region of interest avoiding handling of the relatively heavy scanning head during the positioning procedure. The IU is attached to the skin with double-sided tape, additionally, a 10 µm thick transparent foil can be used to avoid contamination in clinical studies. A small compartment in the interface unit is filled with a water or deuterated water to couple optoacoustic waves from the skin to the transducer. Furthermore, if the foil is used, the ultrasound gel is applied to ensure coupling between the skin-foil-coupling medium interface. When operating in the NIR region above 900 nm the deuterated water is preferred due to increased absorption of the water.

3.6. Image pre-processing and reconstruction

Acquired optoacoustic signals are transferred from the DAQ to the PC for further processing and reconstruction. In order to improve signal quality prior reconstruction, several steps are required.

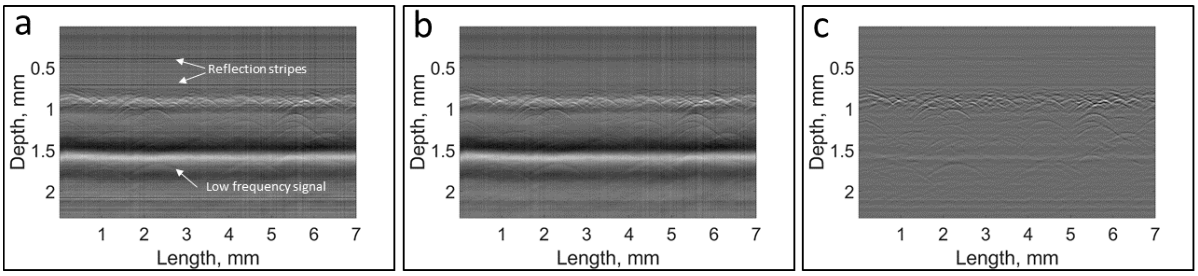

Figure 3.3 Preprocessing of the acquired optoacoustic signals.A single B-plane of an optoacoustic measurement of the human skin. a) Raw signals before the preprocessing; arrows indicate high intensity reflection signals caused by the light reflected from the skin and hitting the surface of the transducer and low frequency reflections of the signals inside the acoustic lens b) the horizontal stripes are filtered using spatial filtering; c) the signals are filtered using exponential filter in the range from 14 to 120 MHz.

The light illuminating the skin is partially reflected from the skin surface back to the transducer heating the active element and generating a high-intensity piezoelectric signal. When using the 55 MHz transducer, which has an acoustic focusing lens, the generated signal travels several times within the lens producing multiple parasitic signals that interfere with optoacoustic signal from the tissue. The reflection signal appears at the same time position since the speed of light is considered instant comparing to the speed of sound. When a B-scan is formed, the reflection signal appears as horizontal lines parallel to the lateral scanning plane (Figure 3.3). In order to suppress the horizontal lines a frequency filter in the Fourier space is applied [93]. The filter is designed in such a way that high frequency, which have a broad spectrum along k_y at k_x=0 in the Fourier domain are suppressed, while low frequency components are preserved. Mathematically, the filter can be expressed as follows:

$$f(k_x, k_y) = \begin{cases} 1, \ k_x \neq 0 \\ \exp(-\frac{k_y^2 \sigma^2}{2}), \ k_x = 0 \end{cases}, \qquad 3.18$$

where σ is the parameter that can be adjusted to ensure that only high frequency components corresponding to the horizontal lines are filtered out.

Aside from the high-intensity and -frequency signal that is generated by the reflected light hitting the transducer surface, in the case of skin imaging, optoacoustic signal detected by the 55 MHz transducer contains a low frequency parasitic signal that is characterized by the reflection of the generated inside tissue optoacoustic signal inside the focusing lens

(Figure 3.3). A bandpass filtering is required to suppress the frequencies which lay outside the bandwidth of the employed transducer. Throughout this work an exponential filter of the 4th order was implemented to filter the optoacoustic signals:

$$f_{filter}(f) = (\exp(-\left(\frac{f}{f_{high}}\right)^4)) \cdot (1 - \exp(-(\frac{f}{f_{low}})^4)), \qquad 3.19$$

where $f_{high}$is higher cut-off frequency and f_{low} is lower cut-off frequency.

The next step to obtain 3D maps of chromophores requires the reconstruction of the acquired optoacoustic signals. The reconstruction of the RSOM data is based on the universal back projection formula, which is described by the following expression [167] and it is an analytical solution of the Equation 3.13:

$$p_0(\vec{r}) = \int \frac{d\Omega}{\Omega}(2p(\vec{r}_0, t) - 2t\frac{\partial p(\vec{r}_0,t)}{\partial t}), \qquad 3.20$$

where $\vec{r}_0$ denotes the vector pointing to the position of the transducer, $t = |\vec{r} - \vec{r}_0|$ is a spatial distance from the source of the reconstruction point to the transducer, and $d\Omega$ is the solid angle of the transducer with respect to the reconstruction point. The direct term $p(\vec{r}_0, t)$ dominates the solution for the sources close the detector, while the derivative term $t\frac{\partial p(\vec{r}_0,t)}{\partial t}$ is larger for the distant sources and represents a ramp filter suppressing lower frequencies. The normalized angle $\frac{d\Omega}{\Omega}$ describes the contribution of each detection element to the reconstruction, or how much of the wave front from a reconstruction point is captured at a certain position of the detector. This solution is exact for spherical, cylindrical and planar geometry of the detectors if the following assumptions are valid: thermal and stress confinement are satisfied; the sound propagates in the homogeneous, isotropic, liquid-like medium where acoustic and light attenuation are not taken into account; the detection aperture is infinite in respect to the size of ROI; the detection consists of infinitely small omnidirectional point-like detectors that have infinite bandwidth.

However, the transducers employed in the RSOM system are conditioned to the limited bandwidth and aperture. Additionally, the detection plane cannot be considered infinite in respect to the size of the scanned region. As it has been mentioned above, the detection geometry of the RSOM system can be represented by a single transducer moving in the raster-scanning manner in the plane. Therefore, at each position $\vec{r_i}|_{i=1:N}$ on the plane an optoacoustic time signal is recorded. The RSOM transducers are spherically focused either by an acoustic focusing lens (55 MHz transducer) or by curving the detection surface (24 MHz transducer). Therefore, a virtual point like detector with a defined aperture can be assumed in the focal point of a transducer [172]. The virtual detector is shifted by the focal distance along z-axis normal to the detection surface of the transducer, thus the time coordinate transformed to space coordinates can be written as:

$$\vec{t} = (\vec{\mathrm{t}}_{samp} - t_{foc}) \cdot v_S, \qquad 3.21$$

where $\vec{\mathrm{t}}_{samp}$ is a time vector corresponding to the discrete time points, t_{foc} is the time, which takes acoustic signal to propagate from the focal point to the transducer. Another consideration, which has to be taken into account, is that the focus of the transducer has a finite size. In order to calculate the width of the focal zone at -6 dB level, the following expression can be used [173]:

$$d_{foc} = 1.02 \frac{F_d v_S}{fD}, \qquad 3.22$$

where F_d is the focal length of a detector, D is the diameter of the detector, f is a frequency of the detector at which the beam diameter is calculated. It can be seen from the Equitation 3.22, that the frequency detected by the employed transducer determines the size of the virtual detector.

The reconstruction can be also improved by incorporating a 3-dimentional sensitivity field (SF) of a transducer. The SF can be expressed as a convolution of the spatial impulse response (SIR) with an ultrasound signal, which has the bandwidth matching to the one of the detector; alternatively, the SIR can be experimentally measured. The SIR can be estimated by integrating delta impulses $\delta(t)$ over the transducer surface for each point in space $\vec{r}$ [174]:

$$SIR(t, \vec{r}) = \int \frac{\delta(t - |\vec{r}_d - \vec{r}|)}{|\vec{r}_d - \vec{r}|} dS(\vec{r}_d), \qquad 3.23$$

where $\vec{r}_d$ is the position of infinitesimally small element on the surface S. The central frequency of a spherical absorber is obtained using the following expression [105]:

$$f_c = 0.8 \frac{v_S}{2R_S}, \qquad 3.24$$

where R_S denotes the radius of the absorber. In order to calculate the size of the absorber that generates the broadband optoacoustic signal, the expression (3.24) can be transformed into [105]:

$$R_S = 0.8 \frac{v_S}{(f_{high} + f_{low})}. \qquad 3.25$$

The analytical solution for a propagating ultrasound wave generated by a spherical absorber is determined as follows [154]:

$$p_{gen}(t, R_S) = p_0 \frac{r - t}{2r} \cdot H(R_S - |r - t|), \qquad 3.26$$

where H is the Heaviside function, r is the radial coordinate originating in the center of the source. As the result, the SF of the transducer expressed as a peak-to-peak amplitude of the convolved SIR is:

$$SF(\vec{r}) = \max\left(SIR(t,\vec{r}) * p_{gen}(t,R_s)\right) - \min(SIR(t,\vec{r}) * p_{gen}(t,R_s)), \qquad 3.27$$

where $p_{gen}(t,R_s)$ is a generic optoacoustic signal with a bandwidth matching to the bandwidth of the detector.

The simulation of the sensitivity field is performed in the Field II simulation program using expression 3.27 [105,175]. The simulation consists of splitting the concave surface of a transducer into N finite elements and detecting the response for each of N detectors to the received signals from different position in ROI. The wave front of a pressure wave reaches each of N elements at different time points constituting the response of the transducer as an average for all N finite elements, which also determines the directivity and the magnitude at each point of the SF.

Despite the simplicity of the universal back-projection formula, its implementation is impeded by the complexity of the numerical calculations. However, parallel processing using a GPU can significantly reduce the time required for the reconstruction due to linearity of the algorithm. The bottleneck of the GPU processing is its memory size, while the speed of the reconstruction depends primarily on the number of transfers of the data from and to GPU. Therefore, the digitized optoacoustic signals must be split along depth into slabs of a certain size to match the memory capacity of the GPU. Finally, only the voxels inside the sensitivity field are reconstructed, which significantly reduces the number of operations [105].

3.7. Image post processing

The RSOM imaging is characterized by the ultra-wide bandwidth of the utilized transducers. This allows to detect and resolve the features ranging in the size from less than ten to hundreds micrometers. However, due to the higher energy absorbed by the bigger object the generated signal will have a higher amplitude than the signal from a smaller structure, considering the same absorption coefficient [154]:

$$|p_0| = \Gamma \mu_a d, \qquad 3.8$$

where Γ is the Grüneisen parameter, μ_a is the absorption coefficient, and d represents the size of the object (diameter for a sphere, or thickness for a slab).

Another aspect that alters the detected frequency content of an optoacoustic signal is acoustic attenuation of the media where the signal is propagating. It has been shown that the attenuation coefficient of sound for various media obeys the power law and can be expressed as:

$$\alpha_s = \alpha_{s0} |\omega|^n, \qquad 3.99$$

where α_{s0} and n are real positive constants, and ω is the angular frequency of the propagating wave. α_{s0} for many tissues ranges from 0.5 to 1 $dB/(cm \cdot MHz)$, while n is 2 for water and typically 1 for tissue. The Equation 3.29 shows that attenuation coefficient increases exponentially for higher frequencies with increasing depth.

The prevalence of the low frequency signal due to frequency-dependent attenuation in tissue and stronger signals generated by larger objects will lead to the obstruction of small features in the reconstructed images by larger ones, therefore leading to deterioration of the image quality. In order to circumvent this problem, the frequency content of the detected optoacoustic signals can be divided into separate bands. Further, signals corresponding to different bands are processed and reconstructed independently. Ringing artifacts arising due to bandwidth filtering, can be avoided by ensuring the relative bandwidth for each sub-band is constant:

$$\frac{BW_1}{f_{c1}} = \frac{BW_2}{f_{c2}} = \cdots, \qquad 3.30$$

where BW_i denotes sub-band i, f_{ci} is the central frequency for i-band. In order to define which sub-bandwidths are to be used, the relative bandwidth ($BW_{\%}$) and the first cutoff frequency (f_1) must be selected. The second cutoff frequency is calculated as follows:

$$f_2 = \frac{2+BW_{\%}}{2-BW_{\%}} f_1. \qquad 3.31$$

Thus, for the 55 MHz transducer 100% the relative bandwidth and 14 MHz the first cutoff frequency (f_1) are selected. The second cutoff frequency from the Equitation 3.31 is $f_2 = 42\,MHz$. Similarly, the second sub-band BW_2 can be identified as $f_3 = (2 + BW_{\%})/(2 + BW_{\%})\,f_2 = 126\,MHz$ [91].

The reconstructed images corresponding to different bands can be independently denoised using thresholding of the signals based on the maximum value or more sophisticated methods to remove background noise, such as “rolling ball” method. Furthermore, each band can be equalized in terms of intensity of the signals to enhance the contrast. Finally, two or more reconstructed images corresponding to different sub-bands can be color-coded and combined into a composite image improving visualization of the fine structures.

3.8. Conclusion

In this section the UWSB RSOM instrumentation along with the underlying basic principles of acoustic signal generation, the main challenges of the optical and acoustic inverse problems have been introduced. The principles of the optoacoustic signal generation include absorption of modulated electromagnetic signal by the skin chromophores followed by generation of acoustic signals. The acoustic inverse problem relates to identifying (reconstructing) the positions of the chromophores/absorbers in the tissue from the detected acoustic signals [161]. Assuming the sources of the acoustic signal are mapped unambiguously, the optical inverse problem in optoacoustic imaging consist in finding the concentrations of the chromophores $c_n(\vec{r})$ from the measured absorbed optical energy density $H(\vec{r})$. I

In order to perform morphological and physiological imaging of skin, the UWSB RSOM system was developed. The system is based on the previously reproted UB RSOM setup and is upgraded by an optical parametric oscillator, two fast single-wavelength lasers and two transducers (25 MHz and 55 MHz). The OPO operates in a broad optical spectral range spanning from 420 to 2000 nm, which can be particularly suitable for identifying the main skin chromophores, such as hemoglobins, melanin, lipids and water in a concurrent manner. The fast single-wavelength lasers can operate at repetition rates over 1 kHz at 515 nm and 532 nm wavelengths, which is advantageous for the imaging of the fast changing parameters, such as blood volume and oxygenation of skin microvasculature. The UWSB RSOM can incorporate two transducers, performance of which depending on the imaging problem improves visualization of certain skin structures. The reconstruction procedure in the RSOM system utilizes a universal back-projection formula accelerated by GPU computing. In order to achieve high quality imaging, the detected optoacoustic signals are filtered in terms frequency content to match the bandwidth of the transducers and the parasitic reflection signals are removed by spatial filtering. Furthermore, the bandwidth-specific visualization is implemented to highlight fine features attributed to high frequency signals.

Based on the characteristics and performance of the UWSB RSOM system introduced in Section 3.5, the system can be implemented for detection of the intrinsic skin chromophores (hemoglobin, melanin, water, lipids) and skin structures based on their absorption properties. Furthermore, fast scanning times achieved by implementing the fast repetition rate lasers can be applied for monitoring fast changing parameters of the skin microvasculature, such as oxygenation and blood volume changes.

4. RSOM for assessment of the blood volume changes

This chapter contains adapted text passages and figures from the publication by Berezhnoi et al. [176] © 2018 WILEY-VCH.

More information on the permission to reproduce textual material and illustrations can be found in appendix B.

4.1. Introduction

In Section 1.2 and Section 2.2 it has been discussed that morphology and response of skin microvasculature to physical and pharmacological trials may reveal specific vasculature dysfunction as well as general systemic pathologies. This is not surprising given that the skin is the largest organ of the human body and is subject to general metabolic and homeostatic regulations as well as impairments due to systemic diseases. Thus, the complementary use of dermal vascular tests with other diagnostic methods could help to better evaluation of the disease, with prospect of improved treatment.

The blood flow (and blood volume) increase due to focal hyperthermia in the non-glabrous skin is attributed mainly to vasodilation and vascular recruitment [58]. Physiologically, this is rather a complex and multi-phasic process, which involves rapid early dilation, reaching the peak in 2-3 min, followed by 2-3 min moderate decline of vascular perfusion. The intermediate phase of the hyperemic response in skin to the external focal heat stimulus comprises middling dilation that plateaus [58]. Sustained heating generally results in a “die away” trend observed approximately after 40 min [177]. There are two main mechanisms considered to be responsible for the vasodilatory response: axon reflex and release of Nitric Oxide mediators [178]. The early phase is thought to be due to the fast neural response, which involves the axonal reflex, followed by slower vasodilation due to release of neuro-mediators and vasodilator substances [179]. To derive clinical value from the characterization of the hyperemic process, it is important to analyze the dynamics at the level of microvessels under physiological and pharmacological interventions.

Profuse vascularization of the skin and the strong light absorption characteristics of blood provide strong contrast for the use of optical imaging within the visible region for visualizing the morphology and functionality of the skin. Optical imaging methods such as Doppler flowmetry (LDF) [58], Laser Doppler Perfusion Imaging (LDPI) [60] and laser speckle contrast imaging (LSCI) [180] have taken advantage of these, and were widely employed for capturing and characterizing the skin microvasculature and physiological dynamics. In experiments consisting of heating a small region of the forearm in the 35^0-43^0C temperature range, increments of blood flow in the human skin were observed with LDF. The signal displayed an initial transient increase followed by a plateau [57,58], generating two dimensional maps related to flow values [60]. The LDPI local thermal hyperemia measurements improved the reproducibility in inter-day experiments, by accounting for skin heterogeneities [61]. Another method which also was used for heat hyperemia tests is LSCI [180], which also provides 2D blood flow maps. In terms of local thermal hyperemia assessment, LSCI showed better reproducibility in inter-day measurements and was used for reactive measurements compare to LDPI [61]. The primary limitation of these methods is related to the diffusive nature of the light, which due to scattering of photons leads to corruption of the signal incoming from vessels obtaining the averaged value of blood flow in ~1 mm^3 region, compromising the imaging depth and resolution. Thus, there is an unmet need in improved structural and functional imaging of skin in order to rigorously test and to derive solid clinical value from hyperemic measurements [34,35]. Such tools could therefore boost translational research in the many important diseases that affect the tone of the vascular bed with the view of ensuring the viability of the healthcare system.

With its central ability to break the light diffusion resolution limit through combining light excitation with ultrasonic measurements, optoacoustic mesoscopy provides improved skin imaging and enables data acquisition through the whole skin depth yielding 4 μm axial and 20 μm lateral resolution [181]. From such images, perfusion related parameters could be obtained and assessed with great precision. Consequently, RSOM has the potential to impact clinical decision making by allowing assessment of the microvascular responses to thermal stimulations. To investigate this premise, clinical UB RSOM was combined with a method conceived to obtain precise control of the heating at the skin surface while not interfering with the imaging procedure.

4.2. RSOM imaging system and acquisition protocol

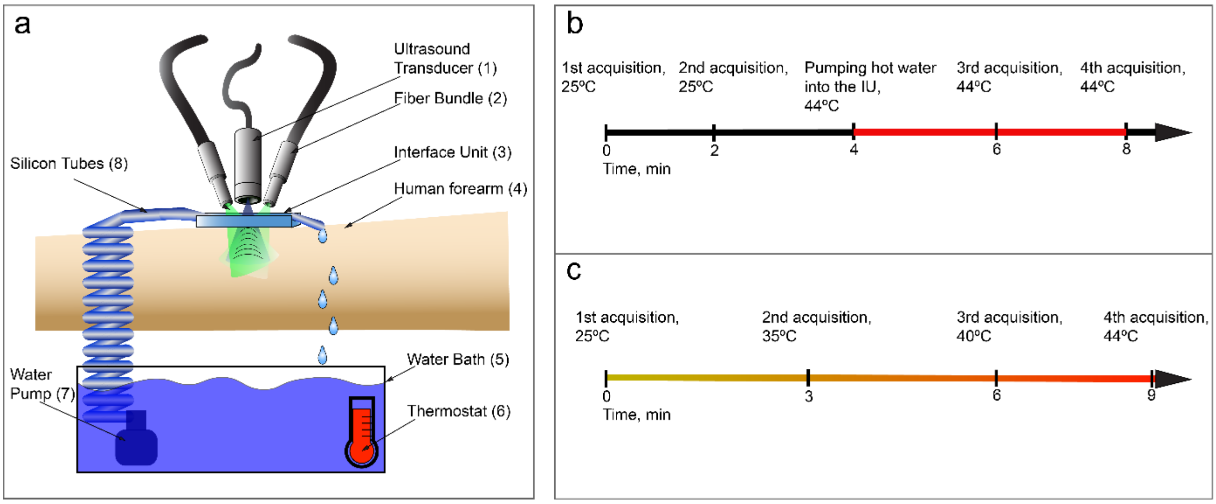

Figure 4.1 Schematic of the RSOM system and experimental protocol for assessment of the heat induced hyperemia. (a) Custom-built handheld RSOM system featuring a precise temperature control system for focal heating. The ultrasound transducer (1) and fiber bundles (2) are raster-scanned together over the ROI on the skin surface. The interface unit (3) contains coupling medium and is in direct contact with the forearm (4). Water (5) in a thermostated bath (6) is pumped (7) via silicon tubes (8) through the interface unit. (b) Schematic of the timing of RSOM measurements during rapid heating experiments. The red line indicates a water temperature of 44 °C in direct contact with the skin surface. (c) Schematic of the timing of RSOM measurements during gradual heating experiments. Adapted from Berezhnoi et el. [176] © 2018 WILEY-VCH. Reproduced with permission.

In order to assess skin microvascular functional changes in response to focal heating of the skin surface the hand-held clinical RSOM built in-house [182] was combined with a system for precise control of the heating stimulus (Figure 4.1a). The clinical RSOM system is described in detail in Section 3.5.

Following the acquisition procedure describe in Section 3.5, the detector along with the two outputs of the fiber bundle were raster-scanned by precise piezoelectric stages collecting signals from a 4 mm × 2 mm ROI with a 15 µm step size. To comply with the safety limits of the laser exposure according to the American National Standard for Safe Use of Lasers (ANSI) [183] the output light energy delivered to the skin surface did not exceed 3.75 µJ/mm^2 at 500 Hz repetition rate.

The heat mediated vasodilation was induced by a built in-house designed temperature control system (TCS). The system allows to select a temperature range that varies from room temperature (25 ˚C) up to 50 ˚C with 1 ˚C precision. The TCS consisted of a water bath, a thermostat, a water pump, a thermometer, and silicon tubes (Figure 4.1a). The temperature in the water bath could be adjusted to the desired values by means of the thermostat. Once the water reached the desired temperature, it was pumped from the water bath into the IU. Besides, if the water in the IU reached a certain level, it dripped into the water bath naturally, without any significant disturbance for the subject being measured. Therefore, by constantly pumping the water from the bath to the IU, a closed circuit was created in which the water at the IU would reach the temperature of the water bath in a few seconds, remaining constant afterwards. The temperature in the water bath was constantly monitored and adjusted to the desired values in a precise manner.

The image preprocessing and reconstruction were performed corresponding to the steps described previously in Sections 3.6 and 3.7. The reconstruction parameters were adjusted assuming a constant speed of sound in the reconstructed volume. To avoid instability of the measurements caused by temperature variations of the coupling medium, the speed of sound values was taken as in water at the temperature of the coupling medium (for example 1525 m/s for 25 ^{0}C and of 1585 m/s for 44^{0}C). The representation of reconstructed 3D data is performed by taking the MIP along one of the dimensions. The high frequency band MIP occupies the green channel of a RGB images whereas the low frequency band MIP occupies the red channel. Thanks to the frequency band equalization, the different objects are discriminated on the images depending on their size, the smaller vessels appearing in green and the bigger in red [182].

To assess the hyperemic response to local heat in the skin of 6 healthy non-smoking volunteers, one female and five males were recruited in the study. All volunteers were aged between 25 and 35 years and signed in a written informed consent before participation. They spent about 30 minutes seated in a chair prior the measurements to acclimatize to the room environment. The forearm was positioned at least 10 cm below the heart level to avoid blood flow alterations attributed to the risen forearm. Two types of imaging experiments were performed. Single temperature change measurements and gradual temperature increment measurements.

In the single temperature change measurements, the temperature of the coupling medium is raised from 25 °C to 44 °C and imaging is performed twice before and after skin heating. In the second type the temperature of the coupling media is raised gradually from 25 °C to 44 °C and several acquisitions are made at different temperature points (Figure 4.1b). In order to achieve imaging of the same ROI, the IU was affixed to the forearm throughout the acquisition procedure. The blood volume variations due to vascular heterogeneity in the skin were minimized by rigid image registration of the reconstructed images, where the vascular network and ink dots on the skin surface were used as references.

The blood volume in the skin was quantified over an ROI of approximately 4 mm x 2 mm x 0.75 mm in the x, y, and z axis, respectively. The ROI conveyed the skin situated below the epidermal-dermal junction. The size of the ROI was slightly modified in a per subject basis due to motion and the skin depth variations from subject to subject. The total blood volume (TBV) values were calculated by applying a threshold corresponding to 20% of the maximum intensity. Voxel values which fell below the threshold were discarded, while the values above the threshold were set to 1. Furthermore, the total blood volume was calculated as follow: $TBV = \sum V_i \times dV$ where V_i is the i-voxel's value and dV is the voxel volume. The partial blood volume was also calculated for each volunteer to avoid inter-subject variability of the blood volume using the following equation: $PBV_k = TBV_k/Vol_k$, where Vol_k is the volume of the ROI. The mean PBV and the standard deviation were obtained for 4 sets of measurements (2 – before local heating, 2 – during local heating) of each aspect of the forearm. Statistical analysis was performed using a paired-samples t-test.

To showcase the functionality of RSOM system in examining single blood vessels, the vessel's diameter calculations were performed using a cross-sectional MIP of the reconstructed images. The vessels were selected by an independent observer in the region of the horizontal plexus. The diameter was defined as a full-width half maximum obtained from a profile of a vessel in the direction of its radius, assuming that locally the vessel is a cylinder.

4.3. Results of heat induced hyperemia assessed by RSOM

In this study the skin of the volar and dorsal aspect of the human forearm was imaged to examine the reaction of cutaneous microvasculature to local hyperthermia. To ensure stability of the measurements irrespective to the site of the forearm and amount of melanin in the epidermal layer, the volar and dorsal aspects were chosen.

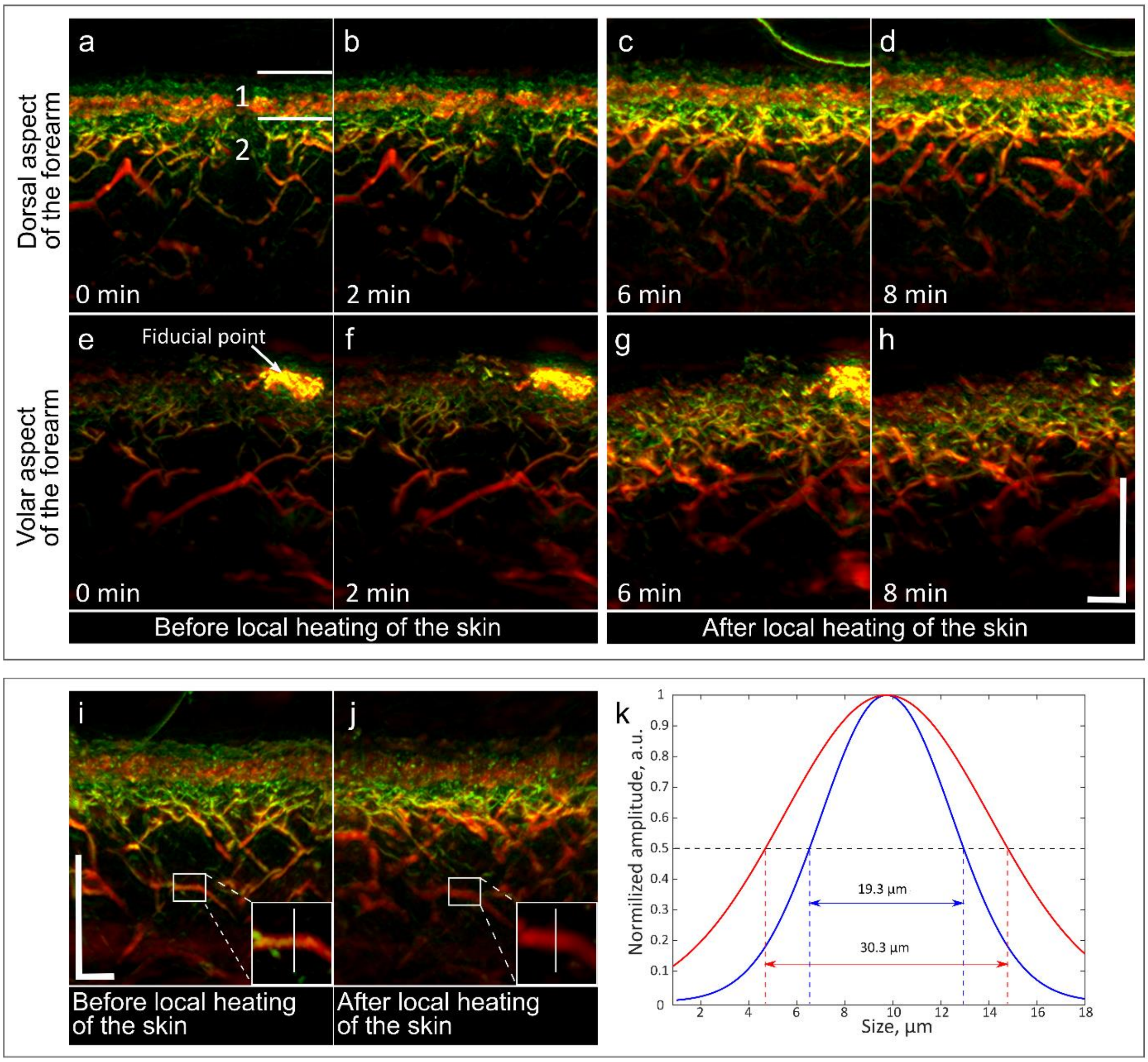

Figure 4.2 Optoacoustic imaging of the dermal vasodilation induced by thermal stimulation. Sagittal views of dorsal aspect of the forearm (A, B) before and (C, D) after local heating of the skin. Sagittal views of volar aspect of the forearm (E, F) before and (G, H) after local heating of the skin. A single vessel diameter (I) before and (J) after local heating. (K) A single vessel profile before (blue curve) and after (red curve) local heating. The compartments marked in (A) correspond to the epidermal layer (1) and the dermal layer (2). Scale bars: 500 µm. Adapted from Berezhnoi et el. [176] © © 2018 WILEY-VCH. Reproduced with permission.

For the anatomical references, the two compartments marked in Figure 4.2a comprise the epidermal layer (1) followed by dermal capillary loops, which are at the very top of the upper horizontal plexus and are connected to the vasculature network of the horizontal plexus (2). The anatomical structure of the skin depicted in Figure 4.2 is consistent with previous RSOM studies [184] and different layers of the skin can be distinguished. However, the layered structure of skin in the volar aspect of the human forearm (Figure 4.2e-h) is not so evident due to the low amount of melanin pigment.

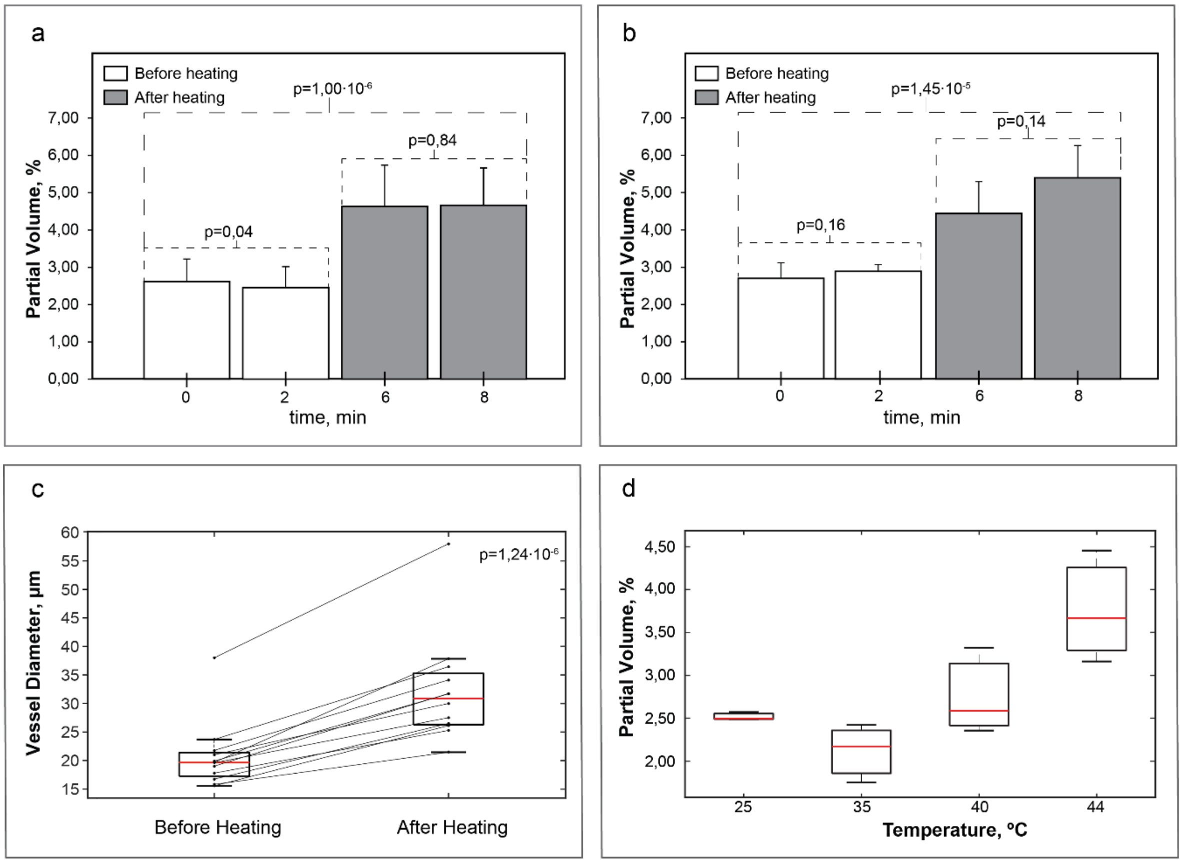

Figure 4.3 RSOM quantification of the heat-induced vasodilation. (a-b) The volar and dorsal aspects of the forearms of six healthy volunteers were imaged using RSOM before and after heating at 44 °C. Partial blood volume was measured in dermis of the (a) volar aspect and (b) dorsal aspect. (c) Blood vessel diameter was measured in 12 arbitrarily selected vessels in the dermal upper plexus of the volar forearm of multiple volunteers. Solid black lines connect diameters of the same vessel before and after heating. (d) Partial blood volume was measured in dermis while the temperature of the coupling medium at the skin surface of three volunteers was gradually heated from 25 °C to 44 °C over 9 min. Adapted from Berezhnoi et el. [176] © © 2018 WILEY-VCH. Reproduced with permission.

After 2 min of baseline imaging (Figure 4.2 a, b and e, f), local hyperthermia has been applied and cutaneous hyperemia is imaged (Figure 4.2 c, d and g, h) to determine the response of the vascular bed to increased temperature from 25 °C to 44 °C at the skin surface. Upon heating of the skin, an increase in vascular density all over the measured depth and a distinct color shift to red in deep layers was observed. The impression of a “red shift” can be related to vasodilation since it represents the low frequency content. In Figure 4.2e-h the bright yellow point marked with an arrow is a fiducial point used to perform image registration. The fiducial point is made out of ink and is shifted from image to image due to the slight motion of a participant during the experiment.

To define the physiological impact and meaningfully relate the effects of thermal stimulation on perfusion and blood supply of the skin tissue, the blood volume was assessed before and during focal heating of the skin. Six volunteers have been involved in this study. Figure 4.3 depicts quantitative parameters of the blood volume and vasodilation in the dermis of volar (Figure 4.3a) and dorsal (Figure 4.3a,b) aspects of the forearm before and during heating (white and grey, respectively). Statistically significant p values were defined to be below 0.01. The average partial blood volume in the skin of the volar aspect of the forearm before heating is 2.61±0.61% and 2.46±0.56% for the first and the second time point respectively (n=6, p=0.038, Paired Sample t-test). During the local heating, the partial blood volume increased significantly and plateaued at the level of twice as high as that before heating, with average values of the partial blood volume reaching 4.63±1.10% for the first and 4.66±1.00% (p=0.83) for the second measurement, respectively (Figure 4.3a). Similar baseline values have been obtained also from measurements of the dorsal aspect of the forearm, with calculated blood volume varying slightly between different imaging time points (2.70±0.41% and 2.89±0.18%, p=0.16). After applying local hyperthermia, the blood volume soars up to 4.44±0.86% and 5.40±0.86% (p=0.14), respectively (Figure 4.3b). The statistical evaluation of the data before and during focal hyperthermia determined the significance of the blood volume change with p values of 9.7×10^{-7} and 1.5×10^{-5} for the volar and dorsal aspects of the forearm respectively.

Figure 4.3c summarizes the vasodilation response to local hyperthermia of 12 randomly selected blood vessels from the dermal upper plexus of volar aspect of the forearm. Since blood vessels were selected arbitrarily for this analysis, their initial diameter varies. The left box plot consists of the initial vessel diameter data before application of focal hyperthermia to the surface of the skin. The median value of the initial vessel diameter is 19.3 µm. The box plot on the right displays the data after 4 min of focal heating of the skin surface with the median value of 30.8 µm. The average diameter expansion caused by focal hyperthermia is 1.56-fold with the standard deviation of 10% and p value less than 0.05. Considering the quadratic dependence between radius and volume, the average blood volume has been estimated to increase 2.4 times, which is close to previously calculated blood volume increase. This change is expected to lead to ~6 times increase of the blood flow, given the quadratic dependence of the flow on the radius, according to the Poiseuille’s law.

Monitoring of the temperature dependent changes of the blood volume demonstrated change in dermis for the gradual temperature increase of coupling medium from 25 to 44°C applied focally to the volar aspect of the forearm. Figure 4.3d shows that in all three volunteers, blood volume slightly decreased as temperature increased from 25 °C to 35 °C. On setting from 35°C, increase of blood volume followed linearly the temperature increase of the coupling medium up to 44°C.

4.4. Capsaicin-induced vasodilation

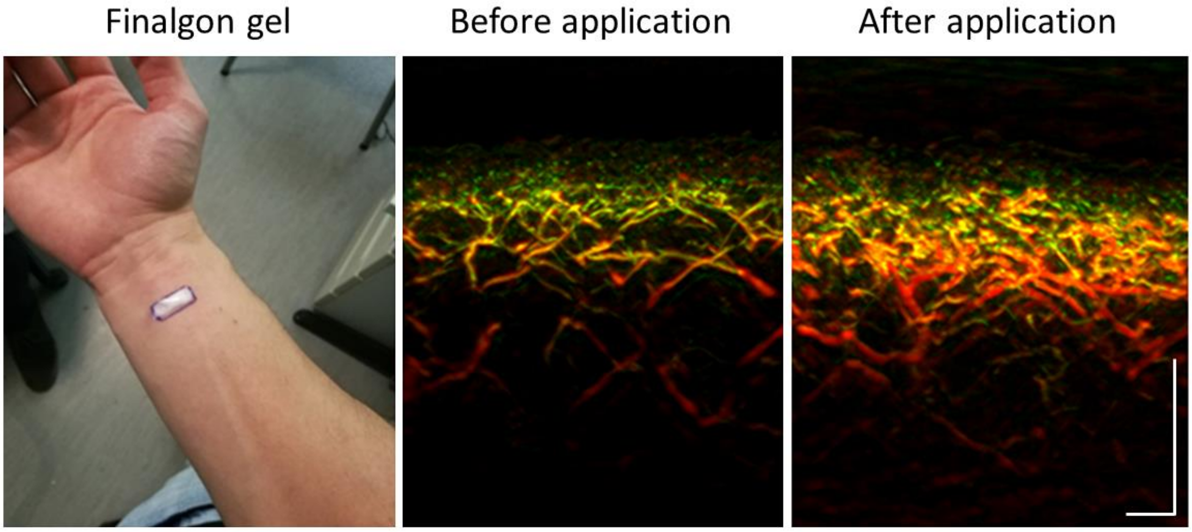

Figure 4.4 Assessment of the capsaicin-induced hyperemic response by RSOM. Left – topical application of the finalgon gel. Center- skin microvasculature before application of the cream. Right – skin microvasculature after application.

In order to investigate the ability of RSOM to capture changes in the human skin microvasculature to cutaneous application of pharmaceuticals, the capsaicin-induced hyperemic response was evaluated. Figure 4.4 shows the results of the hyperemic response in skin microvasculature induced by topical application of the Finalgon gel. One of the main components of the gel is capsaicin, which is known to produce strong burning sensation in humans causing hyperemic response [185]. The left image in Figure 4.4 shows a volunteer's forearm with the gel applied to the skin. In order to monitor the reaction of the skin microvasculature, the forearm skin was imaged with RSOM before the application of the gel and the imaged ROI was marked with ink. Next, the gel was applied topically and distributed evenly in the ROI. After 10 minutes the gel was removed with a towel and an identical ROI was imaged. The central image in Figure 4.4 shows human skin microvasculature at rest and before application of the gel. The dots at the skin surface correspond to the tip of the capillary loops extending into the epidermal-dermal junction from superficial vascular plexus. Similar to the previous local hyperthermia experiments, the “red shift” in Figure 4.4 (right) indicates a strong vasodilation effect induced by the effect of the gel. The vessels appear larger in the deeper dermis, while overall the microvasculature network is denser than before the capsaicin challenge. The hyperemic response to the capsaicin captured by RSOM confirms the results of the heat-induced hyperemia.

4.5. Conclusion

In this study, RSOM was utilized to image the response of dermal microvasculature to the confined hyperthermia and pharmaceutical intervention in human volunteers. In the confined hyperthermia test, the volar and dorsal aspects of the human forearm have been imaged. Up to 1.56-fold dilation of individual vessels has been observed after 4 min of heat application, that led to 2- to 3-fold increase of the blood volume in the human skin in response to the temperature rise from 25°C to 44°C. This is the first report analyzing the effect of hyperthermia on the dermal microvasculature with resolution of single microvessel dilation throughout the entire skin depth. The ability to study the dynamics at single cutaneous microvessels through entire skin depth is thought to be of great basic and translational relevance, rendering the RSOM system as a powerful tool for resolving features and physiological mechanisms not accessible by other imaging modalities, with potentials for diagnostics and clinical applications.

The increment in the skin blood volume of the human forearm upon heating shown here is in general agreement with the reports of other groups using LSCI and LDPI [57,58]. The main advantage of this work is the assessment of hyperemic process unfolding at the level of single vessels, proving the unprecedented capability of the clinical RSOM system to resolve exquisite vascularization and vascular dynamics through the whole skin depth. The performance of the RSOM system mitigates disadvantages, such as spatial uncertainty, penetration depth and resolution, of the pure optical methods, revealing skin structure and microvasculature distribution in dermis [182]. The tightly controlled hyperthermia method conceived for these experiments ensures precise temperature control, and can be readily translated to clinical routine.

Due to the timeline of the imaging protocol in heat induced vasodilation and RSOM acquisition time (40s), the captured responses herein fall around the first transient peak [58]. The rapid behavior of the peak could affect the obtained results adding uncertainty to the interpretation of the data. Nonetheless, the observed robust increase in the average blood volume is in a good agreement with the previous reports. However, the major step forward of this work is that the feasibility of resolving this cutaneous mechanism in response to local heating at the level of microvasculature was shown for the first time. The purpose of this work was to demonstrate new possibilities in physiological measurements of thermoregulatory function of skin and imaging of cutaneous microcirculation by means of RSOM.

The hyperemic response to a focal heat and capsaicin stimulus in the skin of the human forearm was assessed with unprecedented precision by means of a non-invasive clinical RSOM system. In the focal hyperthermia measurements, the RSOM system was coupled to a controlled local heating device. The hyperemia effects are visualized for the first time with single vessel resolution through the whole skin depth. The utilized method for the temperature control of local hyperthermia measurements is precise, practical, and can be employed in clinical trials. As a result of this research, a new tool for studying the mechanisms involved in skin response to external heating is presented. It can be expected that the presented method will expose the underlying physiological processes in thermoregulatory function which still remain poorly understood [186]. The described technology can be used in the clinic to link pathology with its effect in the microvascular tree function, which in turn can provide new tools for improved diagnosis of major diseases.

5. Increasing the number of skin chromophores and skin features detected by UWSB RSOM

This chapter contains adapted text passages and figures from the publication by Berezhnoi and Aguirre et al. [2] © 2019 OSA Publishing.

More information on the permission to reproduce textual material and illustrations can be found in appendix B.

5.1. Introduction

The ability to specifically detect key components of the skin in a non-invasive manner could help to detect and to diagnose skin pathology. For instance, imaging of hair follicles and attached sebaceous glands as well as skin microvasculature and the fat content of the epidermis can be crucial in monitoring and treatment of hair loss, acne, or sebostasis and xerosis [39]. The stratum corneum plays an important role in water retention function and permeability-barrier function of the skin. Lipid abnormalities in the stratum corneum are associated with dryness of the skin [187]. Changes in skin microvasculature play a central role in psoriatic inflammation [182]. In fact, detecting key components of the skin can reveal information about systemic pathology. For example, subcutaneous fat morphology correlates with cardiovascular risk factors [37]. Moreover, understanding of the skin penetration by drugs for treatment and cosmetic purposes can significantly ease the administration of drugs to the patients [188].

As it has been outlined in section 1.3, non-invasive assessment of key skin components at high resolution through whole skin depth is strongly impeded by penetration depth of microscopic techniques or by weak contrast and inability to differentiate molecular composition of mesoscopic techniques. However, the key skin features are rich in molecular composition with unique light absorption spectra, therefore, there is a potential for much better non-invasive techniques, that in principle could visualize such skin structures.

In section 2.3.1, the absorption properties of the main chromophores in skin are presented (Figure 2.2a). Oxy- and deoxyhemoglobin show prominent peaks in the visible range, while their absorption declines drastically in the NIR. The melanin absorption decays following the power law and, while in the visible range it is comparable to hemoglobin absorption, the melanin signal dominates at the wavelength above 600 nm. At the wavelength above 900 nm, lipids, proteins and water govern the absorption of skin with several distinct peaks. The absorption peaks are attributed to overtones of the stretching vibrational mode of the C-H bond in lipids, the N-H bond in proteins, and to the first overtone of O-H stretching in water. The absorption spectra of skin biomolecules overlap, making their separation a challenging task [169].

It has been hypothesized that using UWSB RSOM in the spectral range from VIS to SWIR could reveal hemoglobin, melanin, lipid and water content in human skin *in-vivo*. For that, optoacoustic spectra of skin acquired by UWSB RSOM were analyzed in ultra-broad range from 420 nm to 2000 nm. Furthermore, based on the information extracted from the analyzed optoacoustic spectra of the skin the most suitable wavelengths for optoacoustic imaging of particular chromophores and features of the human skin were identified. The aim herein was to perform volumetric imaging of the skin and to resolve its main components based on their molecular composition with high resolution through the whole skin depth. The OPO employed in the UWSB RSOM system allowed imaging at different wavelengths spanning the range from visible to SWIR spectrum. Hemoglobin, melanin, lipids and water can be detected based on their spectral features in human skin *in vivo*. The ability of UWSB RSOM to visualize skin microvasculature, subcutaneous fat, epidermal melanin layer, sebaceous glands, stratum corneum layer and hair shaft throughout the whole skin depth holds promise for skin assessment and diagnostics in clinical and cosmetic dermatology.

5.2. Experimental

To study the abilities of raster-scanning optoacoustic mesoscopy in the optical ranger from visible to SWIR, a previously introduced in Section 3.4 system was employed. The main components of the system are shown in Figure 3.1.

5.2.1. Optoacoustic spectra of skin assessed by UWSB RSOM

In order to fathom the best contrast for visualization of skin features in optoacoustic images, the optoacoustic spectra of the skin were acquired by UWSB RSOM across the spectral range from 420 nm to 2000 nm. The skin was imaged *in vivo* by scanning 2-dimensinal cross sections at each wavelength. The wavelengths were selected based on the known absorption spectra of the skin chromophores to outline the prominent spectral features. For example, the absorption of oxy- and deoxyhemoglobin has several distinct extrema in the visible range at around 540, 560 and 580 nm, while absorption of lipids has a peak at around 1210 nm. Each B-plane was carried out with an averaging of 10, from which the identified skin features were segmented and their optoacoustic spectra were analyzed by calculating their amplitude over the recorded spectrum. The optoacoustic signals were detected by a lens-less transducer with a bandwidth of 15.5-32.3 MHz and filtered out with a band-pass filter in the range from 10 to 35 MHz according to Section 3.6.

5.2.2. Imaging of skin features

In order to show various skin components based on their absorption spectra of the skin biomolecules, four scans of human forearm skin over 4×2 mm^2 ROI were performed. The first scan was done at 515 nm and 532 nm wavelengths in interleaved manner (see Figure 3.1, Section 3.5) Thus, the images corresponding to different wavelengths were inherently co-registered. The scans at 650 nm, 1210 nm and 1450 nm were performed successively for each wavelength. The acquisition time did not exceed 2 minutes for each scan with the step size of 30 µm along both fast and slow scanning axes at 100 Hz repetition rate of the laser.

In order to facilitate the precise registration of the images, a detachable interface unit (IU) was used. The IU was affixed to the skin using double sided tape during the whole acquisition procedure and could be easily attached and detached to the holder by magnets and guide cones (Figure 3.1). Furthermore, the use of the detachable IU assisted a prompt substitution of the utilized transducers during the acquisition procedure.

5.3. Optoacoustic spectra of skin *in vivo* assessed by UWSB RSOM

Optoacoustic imaging capitalizes on the ability of the molecules to absorb light and convert deposited energy into heat to generate a sound wave. Therefore, in order to perform imaging of skin structures, their optoacoustic spectra have to be analyzed to identify their spectral features. In general, light absorption properties of the biological tissue collected *ex vivo* often differ significantly from the properties of the intact tissue that has not undergone excision and sample preparation. The excision and preparation process (drying and slicing) alters physiology of the sample and, therefore, the light absorption properties. Furthermore, the data obtained from animal models often do not resemble the tissue properties of the human skin. Diffuse light based methods are significantly limited in resolution as a function of depth, therefore do not provide accurate *in vivo* measurements of the absorption properties.

Optoacoustic spectra throughout the whole depth of human skin using the UWSB RSOM system were assessed in an ultra-wide optical range from 420 to 2000 nm. For the first time a high-resolution depth specific skin optoacoustic spectra over such broad range *in vivo* were measured. High resolution performance of the imaging system allowed to identify spectra of epidermis, dermis and subcutis.

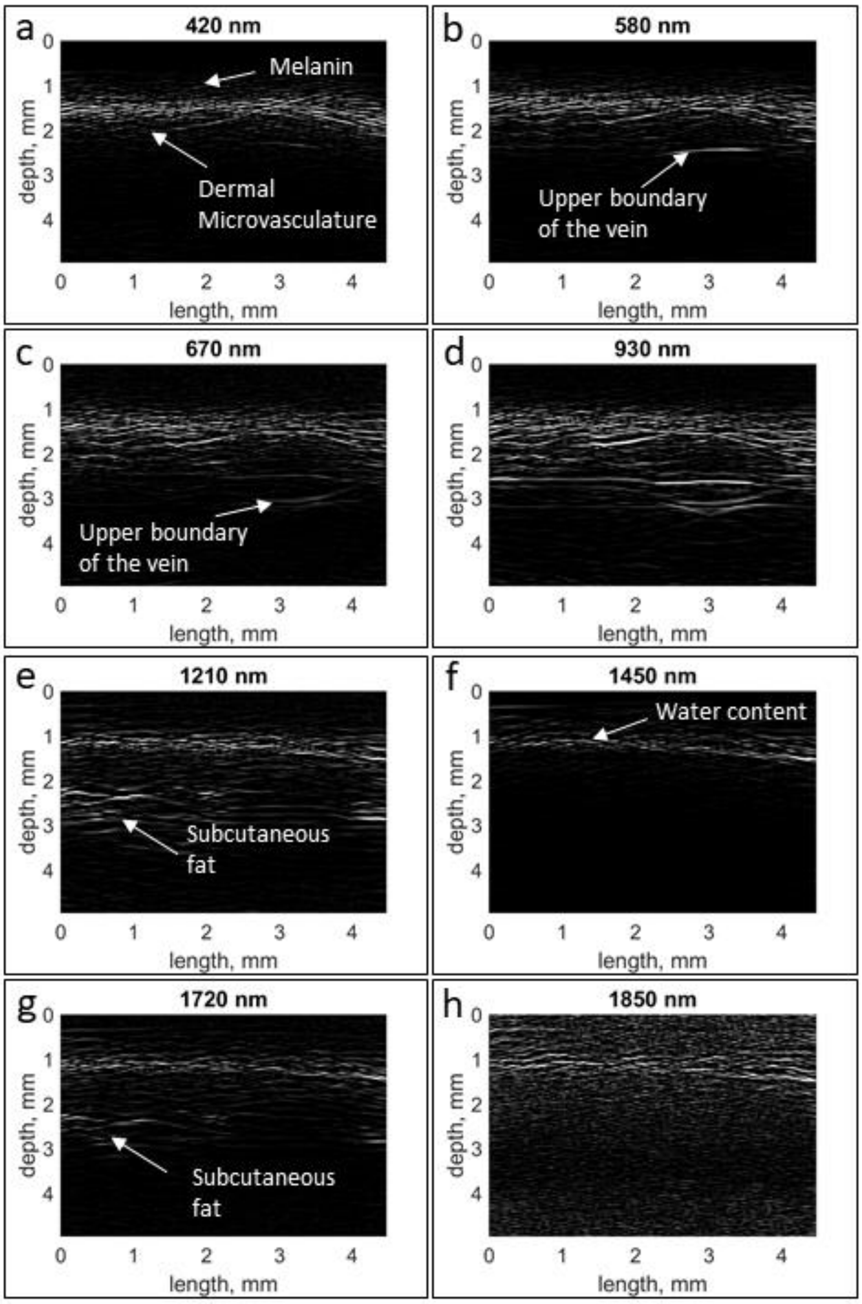

Figure 5.1 Skin features revealed by UWSB RSOM in the range from 420 to 1720 nm. In visible range (a-c) the dermal microvasculature and melanin are the most prominent absorbers. At 930 nm (d) the penetration depth is significantly increased and deeper lying vessels are visible (big vein). SWIR infrared is characterized by the strong absorption of the lipids and water (e-h), therefore subcutaneous fat and water in the epidermis become visible.

Figure 5.1 shows cross-sectional 2-dimensional scans of the human skin at different wavelengths. Figure 5.1a represents a B-plane acquired at 420 nm wavelength, where only superficial dermal microvasculature and melanin signal are visible due to shallow penetration of light at short wavelengths. Tuning to 540 nm wavelength reveals the upper boundary of a deeper lying big vessel at around 1.5 mm depth. Also, dermal microvasculature is visible deeper in the skin compare to 420 nm wavelength. At 670 nm and 930 nm the lower boundary of the big vessel starts to appear, which indicates deeper penetration depth of light at these wavelengths. As expected, 1210 nm wavelength reveals subcutaneous fat layer below upper dermal plexus and water content in the epidermis. Interestingly, the area occupied by the big vessel looks empty at 1210 nm because of low absorption of hemoglobin and is surrounded by subcutaneous fat. Due to strong absorption of water distributed evenly in skin, only water content of the epidermal layer generates optoacoustic signals. 1720 nm reveals another absorption peak attributed to overtones of a vibrational mode of C-H bond in lipids. At last, the signal is reduced significantly at 1850 nm wavelength, and only the signal from the upper layer of skin is visible.

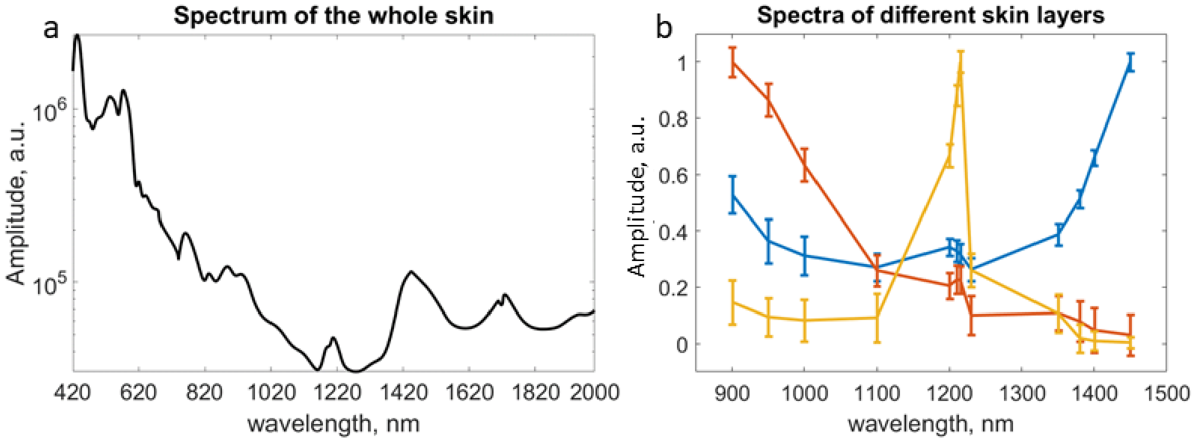

Figure 5.2 Optoacoustic spectra of skin from 420 nm to 2000 nm. (a) Optoacoustic spectrum of the whole skin. (b) Optoacoustic spectra of the skin layers: red-dermis, blue – epidermis, yellow – subcutaneous fat.

Figure 5.2 reveals optoacoustic spectra of the skin and skin layers retrieved from acquired B-planes in an ultra-broad spectral range from 420 nm to 2000 nm. Figure 5.2a shows the spectrum of the whole skin acquired over a spectral range from 420 nm to 2000 nm. The prominent features of hemoglobin absorption dominate in the VIS range rapidly declining in the NIR. In detail analysis of the absorption properties of skin layers in the range from 900 nm to 1450 nm indicates several pronounced spectral features depicted in Figure 5.2b. First, dermal layer has declining amplitude of the signal from 900 nm to 1500 nm (red), which is also resembles the spectrum of hemoglobin in this range. The prominent peak at 1210 nm wavelength corresponds to the subcutaneous fat layer (yellow), while spectrum of the signals from the epidermis (blue) resembles the absorption spectrum of water. The error bars in Figure 5.2b indicated the signal variation inside the segmented region.

5.4. Skin features assessed by UWSB RSOM

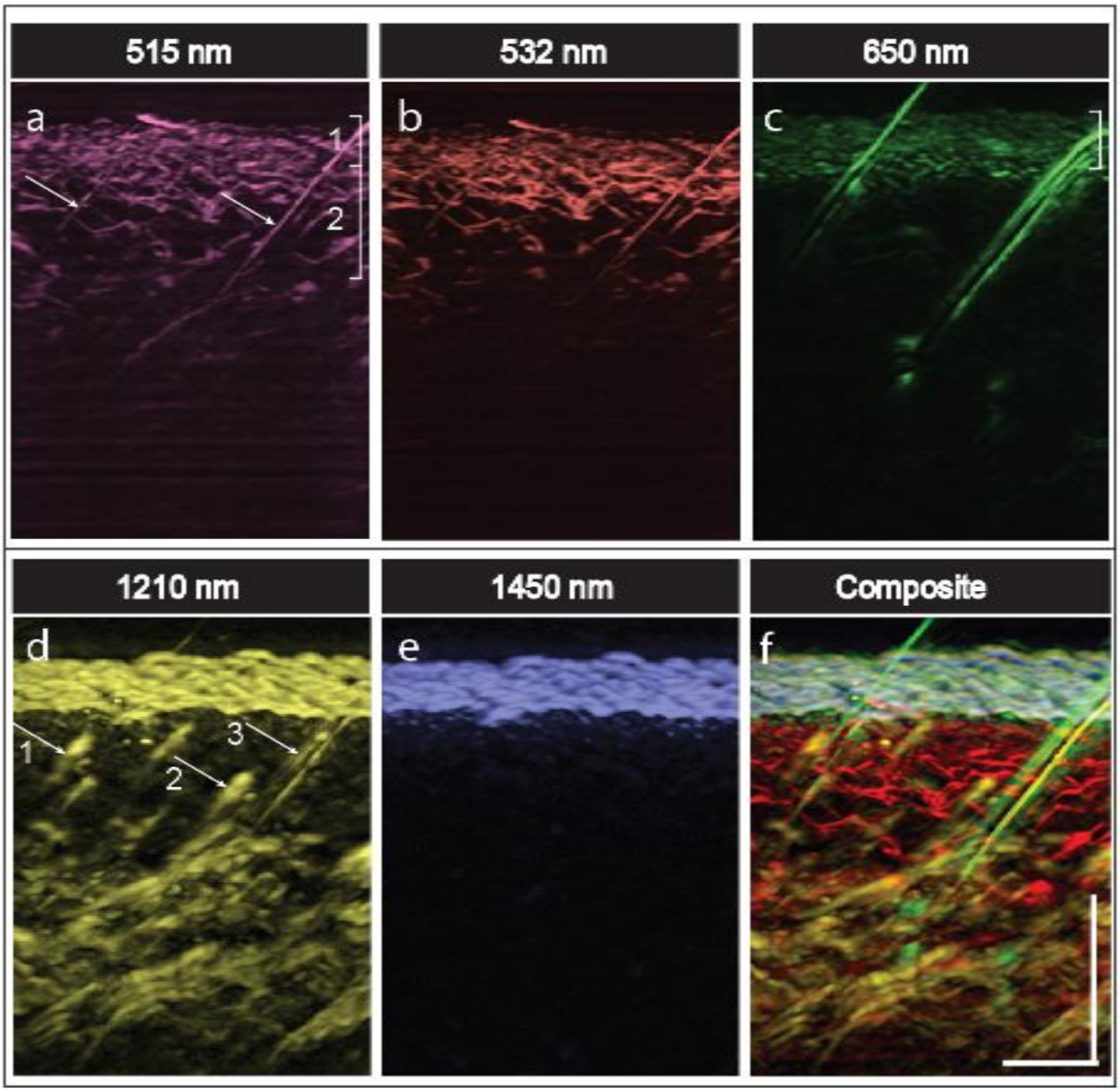

Figure 5.3 Cross-sectional images of the human skin using UWSB RSOM and an ultra-broad spectral region. (a, b) Distribution of blood and melanin in skin (a – 515 nm, b – 532 nm); arrows indicate the position of hair; compartment 1 – epidermis, compartment 2 – upper dermal plexus. **(c)** Melanin in epidermis and hair (650 nm). **(d)** Subcutaneous fat, sebaceous glands (marked with arrows 1 and 2) and water content in epidermis (1210 nm); arrow 3 – sebum content on the hair shaft. **(e)** Water distributed in epidermis (1450 nm); **(f)** Composite of images at all six wavelengths. All scale bars 1 mm. Adapted from Berezhnoi et el. [2] © 2019 OSA Publishing. Reproduced with permission.

In order to determine whether UWSB RSOM could detect a range of key skin components, the forearm skin of a healthy volunteer was measured using UWSB RSOM in the spectral region from VIS to SWIR. More specifically, the optoacoustic signals were collected at five wavelengths which emphasized absorption spectral features of various skin biomolecules.

Figure 5.3 shows MIPs along the sagittal direction of the reconstructed volumetric data sets each of them corresponding to acquisitions at different wavelengths. Figure 5.3a and Figure 5.3b show the MIPs acquired at 515 nm and 532 nm, respectively, using fast single-wavelength lasers (see Section 3.5). At these wavelengths the most prominent optical absorbers in the skin are melanin and hemoglobin, therefore the image shows the epidermal melanin layer (stratum basale) (Figure 5.3a, compartment 1), the dermal microvasculature (Figure 5.3a, compartment 2) and the hair shafts based on the melanin absorption (Figure 5.3a, marked with arrows).

After 577 nm the absorption of hemoglobin decreases significantly compare to the range from 540 to 577 nm, which leads to the dominance of melanin as the main light absorber in the skin producing high intensity optoacoustic signals. As a result, the UWSB RSOM image at 650 nm (Figure 5.3c) depicts primarily the melanin distribution in the epidermis and hairs. Thus, a complete hair with a hair bulb located in the middle of the image and melanin layer are captured.

Figure 5.3d shows an image acquired at 1210 nm, where lipids and water govern the main contrast. Thereby, the upper layer can be attributed to the mixture of water and lipid content in the epidermal layer. The structures indicated with arrows 1 and 2 in Figure 5.3d represent sebaceous glands surrounding hair shaft. Arrow 3 in points out at sebum covering the hair shaft and being delivered to the surface of the skin. Approximately 1 mm below the skin surface of the subcutaneous fat layer is observed.

Figure 5.3e corresponds to an optoacoustic image acquired at 1450 nm. The image indicates the water content encapsulated in the epidermal layer, since water has the strongest absorption of light at around 1450 nm. A prominent signal from below the epidermis is absent due to the limited bandwidth of the employed transducer.

Figure 5.3f shows a composite of the optoacoustic images acquired at different wavelengths. The red color in the Figure 5.3f corresponds to an optoacoustic image acquired in interleaved manner at 515 nm and 532 nm and reconstructed for both wavelengths simultaneously (see Section 3.6) and, therefore, the dermal microvasculature and melanin layer are visualized. Green color depicts signals acquired at 650 nm and represents melanin content in epidermis and hair. The yellow in Figure 5.3f shows the distribution of lipids in the skin bellow the epidermal layer and mix of water and lipid content in the epidermis. Optoacoustic image acquired at 1450 nm is shown in blue color.

5.5. Conclusion

The imaging capabilities of UWSB RSOM were explored in the spectral range from VIS to SWIR. For the first time, hemoglobin, melanin, lipids, and water content are visualized in a complementary manner. High resolution-to-depth ratio attainable by UWSB RSOM facilitates the imaging of the main skin components based on their molecular composition in human skin *in vivo*. For example, a complete hair follicle with attached sebaceous glands surrounded by the dermal microvasculature has been captured for the first time non-invasively and without any exogenous contrast agents. Furthermore, stratum basale and ultrathin stratum corneum are visualized based on the endogenous contrast.

The extended range of wavelengths in UWSB RSOM from VIS to SWIR reveals oxy- and deoxyhemoglobin, melanin, lipid and water. UWSB RSOM is able to retrieve optoacoustic spectra of the skin and skin features and to identify various skin biomolecules *in vivo* based on their characteristic spectra. Previously, multispectral RSOM has detected oxy- and deoxyhemoglobin, and melanin content in skin [96]. It has been reported that the multispectral optoacoustic imaging implementations detects hemoglobin, melanin and lipid content [189]. However, the water content was not shown, and the resolution (75 µm) was worse compare to the one obtained here with the transducers of 55 MHz central frequency (7 µm, axial resolution) and 23.9 MHz central frequency (22 µm, axial resolution). Expanding the optical range of UWSB RSOM to SWIR helped to identify lipid and water distribution because their absorption properties are most prominent in this range. Their absorption in this range is attributed to overtones of the stretching vibrational mode of the C-H bond for lipids and to the first overtone of O-H stretching for water [141]. The biomolecules' spectra often overlap making quantification and visualization of each biomolecule separately a challenging task [169]. The broad spectral range, analyzed herein, is used to facilitate separation of the biomolecules based on their spectral features, rather than unmixing them using computational approaches.

In this work, pilosebaceous unit with hair growing from subcutaneous fat and reaching up the skin surface and above is revealed. Melanin content gives strong contrast to a hair shaft from a hair bulb to the outside of the skin. Lipid content gives a contrast to visualize sebaceous glands, which allows to distinguish the glands from the other skin components. Additionally, the substance on the hair shaft imaged at 1210 nm wavelength can correspond to the deposition of sebum (Figure 5.3d).

The water content is captured in epidermis at both 1210 nm and 1450 nm and may not be visible in deeper skin regions due to the limited bandwidth of the used transducer. The water content below the epidermis might be distributed homogeneously with low variations in its concentration. In this case the transducer's bandwidth acts as a high pass filter rejecting the low frequency signals from the water content of the skin deeper regions. In addition, this effect is reinforced by limited-view artefacts [190]. High-resolution skin microvasculature is visualized based on the absorption characteristics of oxy- and deoxyhemoglobin in visible optical spectrum (Figure 5.3a). Herein, the utilized 515 nm and 532 nm wavelengths can be used to capture the changes in dermal oxygenation [88].

UWSB RSOM delivers increased number of detected endogenous chromophores as well as high-resolved imaging of the main skin components. This may lead to improvement in diagnosis and treatment monitoring of skin and systemic pathologies. While microscopic techniques are mainly limited in their penetration depth, and mesoscopic techniques fall short to provide molecular specificity, UWSB RSOM reveals hemoglobin, melanin, lipid, and water content in skin by utilizing their spectral features. Additionally, the main skin components are imaged through the whole skin depth with high resolution. UWSB RSOM, thanks to its ability to visualize various chromophores in complementary manner, can deliver new detection and diagnosis approaches to dermatology as well to other clinical and biological applications.

6. Functional measurements of skin oxygenation

This chapter contains adapted text passages and figures from the publication by Haedicke, Agemy, Omar, Berezhnoi et al. [191]. © 2019 Springer, Nature Biomedical Engineering.

Furthermore, this chapter contains text passages and figures from the manuscript in preparation by Berezhnoi et el. [192].

More information on the permission to reproduce textual material and illustrations can be found in appendix B.

6.1. Introduction

Oxygenation changes in skin microvasculature can be linked to various skin and systemic diseases. In fact, cancer development is associated with hypoxia due to fast metabolism of the fast dividing cells [193]; reduced blood flow and tissue oxygenation are associated with peripheral vascular disorder, which is one of the most common symptoms of the atherosclerosis [194,195]; skin microvasculature dysfunction is identified to be an early hallmark of diabetes even prior the onset of the disease [29]. Besides, the growth of the malignant tumors is strongly associated with tissue hypoxia and changes in microvascular structure feeding the tumor [11,12]. Skin microvascular dysfunction, in terms of poor skin perfusion and impaired endothelial function, is often a hallmark of the cardiovascular diseases, diabetes and metabolic syndrome [23–25]. Thus, diagnosis of systemic diseases at early stage based on skin manifestation may lead to improvement of therapeutical strategies facilitating more effective treatment [26].

Several non-invasive imaging modalities have been used to study microvasculature and hemodynamics in the skin. Optical modalities, such as LDI, LSCI and near-infrared spectroscopy (NIRS) have shown promising results in visualizing 2-dimensional maps of the blood flow and oxygenation induced by an occlusion test or heating [194]. Tumor necrosis induced by vascular-targeted photodynamic therapy have been imaged by contrast enhanced ultrasound, however, vascular network has not been visualized and contrast remained poor [196]. It has been previously reported that multispectral optoacoustic mesoscopy can image oxygenation at high depth-to-resolution ratio [96]. However, due to low repetition rate of the employed OPO operating at 100 Hz, the acquisition times of 13 minutes limit the use of the OPO for assessment of fast hemodynamic changes.

In order to push the limits of the raster-scanning optoacoustic mesoscopy in oxygenation measurements, first, the UWSB RSOM system equipped with the OPO operating at 500Hz repetition rate (see Section 3.5) was used for assessment of the mouse skin microvasculature, second, dual-wavelength approach was applied to monitor functional and morphological changes in microvasculature of human and mouse skin.

6.2. Oxygenation measurements in mouse skin

6.2.1. RSOM equipped with a 500 Hz OPO

Light sources based on OPOs can generate high energy nanoseconds pulses at wavelengths, that can be tuned in a broad spectra range. In this section the performance of an OPO operating at 500 Hz repetition rate (see Section 3.5) is investigated for raster scanning optoacoustic imaging of the oxygenation of the mouse skin microvasculature in the visible range.

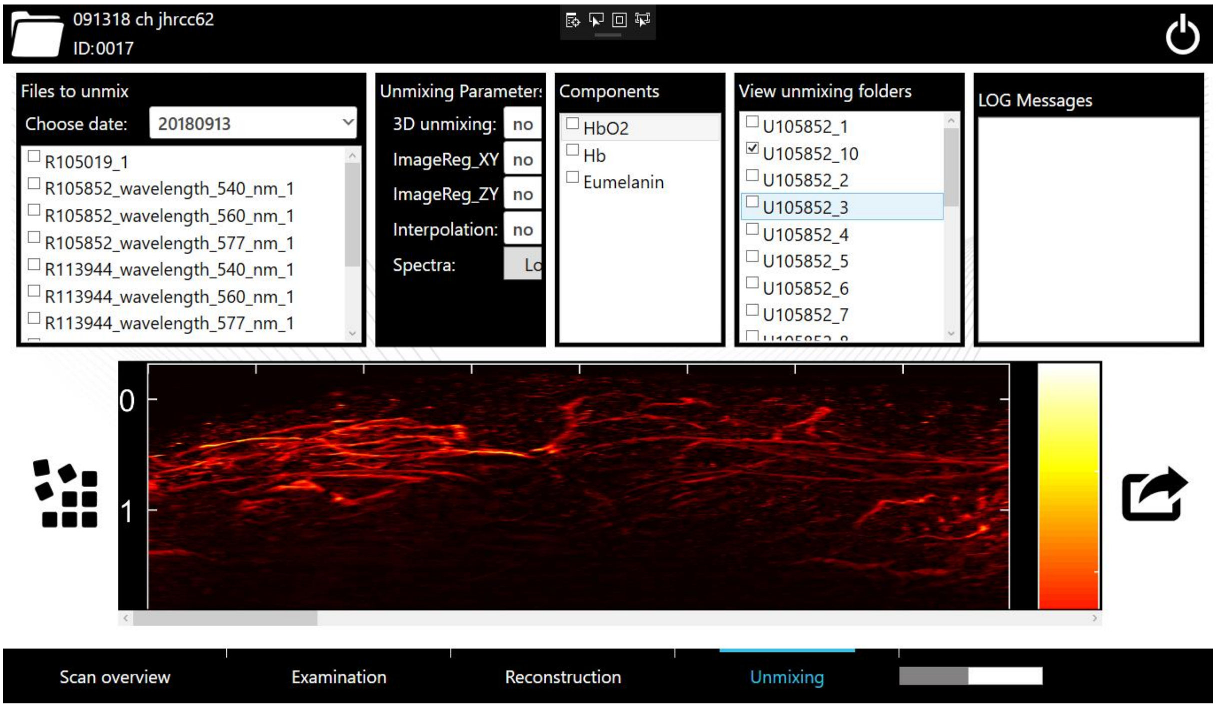

Choose date: 20180913

☐ R105019_1
☐ R105852_wavelength_540_nm_1
☐ R105852_wavelength_560_nm_1
☐ R105852_wavelength_577_nm_1
☐ R113944_wavelength_540_nm_1
☐ R113944_wavelength_560_nm_1
☐ R113944_wavelength_577_nm_1

3D unmixing: no
ImageReg_XY: no
ImageReg_ZY: no
Interpolation: no
Spectra: Lo

☐ HbO2
☐ Hb
☐ Eumelanin

☐ U105852_1
☑ U105852_10
☐ U105852_2
☐ U105852_3
☐ U105852_4
☐ U105852_5
☐ U105852_6
☐ U105852_7

Figure 6.1 GUI for unmixing of the skin chromophores.

In order to control the laser and tuning of the wavelengths per B-plane, the full control of the laser and the acquisition code were implemented in a GUI developed by iThera Medical GmbH for a commercial RSOM Explorer 50 system. Furthermore, the code for linear unmixing of the chromophores from the images acquired at multiple wavelengths was developed and implemented in the GUI (Figure 6.1). The developed unmixing software allowed in a user-friendly manner to select files for unmixing, select chromophores, load spectra of the chromophores, perform unmixing in 3D or less time consuming 2D, and view the results of the unmixing.

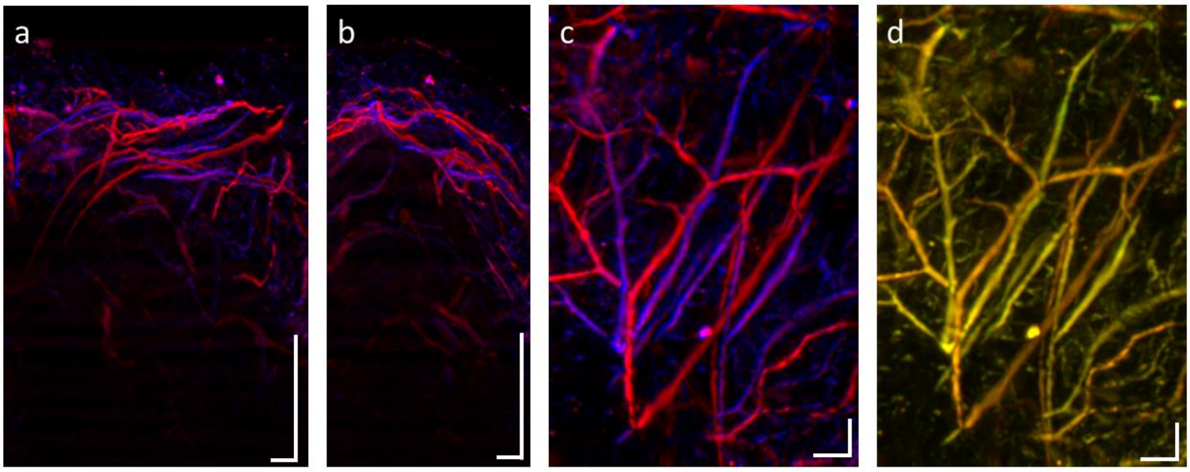

Figure 6.2 Oxygenation of the skin microvasculature in a mouse hip. a) MIP of the of the mouse hip along X axis. b) MIP of the mouse hip along Y axis. c) MIP of the mouse hip along Z axis (top view). In the images a-c, red color represents unmixed oxyhemoglobin, blue color represents unmixed deoxygenated hemoglobin. The images a-c are created by composing the images of the unmixed oxy- and deoxyhemoglobin. d) Merged image of the images acquired at the 540 nm (red) and 560 nm (green). Scale bars 500 µm.

Figure 6.2 shows the results of the RSOM acquisitions performed on the mouse hip skin *in vivo* at 540 nm, 560 nm, 577 nm, and 650 nm wavelengths. The acquired multi-wavelengths data were spectrally unmixed for oxygenated and deoxygenated hemoglobin. The oxygenated hemoglobin is color-coded in red, deoxygenated hemoglobin is color-coded in blue. Figure 6.2a-c represent microvessel oxygenation in the mouse skin of the hip *in vivo* in three maximum intensity projections (X-, Y-, Z-axes). The oxygenation of arterioles is usually above 90% in healthy skin, therefore, red color is dominant. The oxygenation of the venules has been reported to lie in the range from 50 -65%, therefore, the venules are shown as a mixture of blue and red and clearly can be separated from arterioles [197]. Furthermore, the analysis conducted on the unmixed data showed that the values attributed to arterioles lie in the range from 85% to 100%, while the values of the venules are in the range from 50% to 75% which is in a good agreement with previous reports.

6.2.2. VTP assessment by dual-wavelength RSOM

Anti-vascular and anti-angiogenic therapies are developed to deplete malignant tumor of oxygen supply and delivery of the nutrients through microvascular network, therefore reducing tumor growth and metastasis. However, the acquired resistance to the drug or impaired delivery lead to unexpected results of the therapies and require further investigation to highlight the effects of the therapies targeting vascular network of the malignant tumors. Non-invasive imaging technique, such as LSCI or contrast enhanced ultrasound, utilized for visualizing vascular bed have been limited either in the small region of interest, penetration depth or low imaging resolution [194,196].

Imaging capacity of RSOM to visualize skin microvasculature at single vessel resolution may bring new insights into the effects of the anti-vascular and anti-angiogenic therapies on the tumor vasculature. Furthermore, retrieved oxygenation of the vessels may reveal complex oxygenation patterns induced by the therapies. Despite of the great progress in skin oxygenation assessment shown by RSOM coupled to an OPO as explained in Section 6.2.1, implementation of UWB RSOM at even higher operation rates could offer faster scanning times to monitor rapid oxygenation changes, while preserving high resolution imaging through the skin depth in 3D. Furthermore, OPOs require rather complex control, are bulky and expensive, which limits their translation to the clinical and pre-clinical studies.

In order to address this problem two fast repetition rate and high energy lasers operating at 532 nm and 515 nm wavelengths (see Section 3.5) were used for assessment of hemodynamics in skin. The use of the 515 line has several advantages, in particular that the overall performance and imaging depth are similar to those achieved by 532 nm. In addition, the use of two separate cost-efficient lasers could allow interleaved operation and do not increase scanning times, as it would be necessary with a tunable laser. In order to investigate the performance of the DW RSOM system (see Section 3.5) in assessment of oxygenation changes in skin, the vascular changes and tumor oxygenation in mouse skin induced by the vascular targeted therapy were studied.

The DW RSOM system was utilized to investigate the results of vascular-targeted photodynamic therapy (VTP) with WST11 (Tookad®-soluble). Vascular occlusion followed by ablation of the tumor were triggered by illumination of WST11 in the bloodstream around the tumor with a 753 nm laser. The tumor area of 8×8 mm^2 was imaged with DW RSOM before the treatment with the 753 nm laser, 5 min, 1h, and 24 h after the treatment.

The oxygenation changes in the mouse skin microvascular were retrieved as a ratio of the signals acquired at 515 nm and 532 nm. Owning to the absorption properties, oxyhemoglobin has higher absorption at 532 nm while deoxyhemoglobin at 515 nm, indicating that they are on the opposite sides from the isosbestic point (see Figure 2.1a). Therefore, oxygenation changes can be estimated by taking the ratio of the signals acquired at these two wavelength. In fact, the most prominent absorbers of the skin in visible range are melanin, oxy- and deoxyhaemoglobin, while the absorption of the other chromophores can be neglected (see Figure 2.2a). Therefore, the optoacoustic signal from the skin at wavelength λ and position $\vec{r}$ can be approximated by the linear combination of the three absorbers:

$$\mu(\vec{r},\lambda) = \varepsilon_{oxy}(\lambda)C_{oxy}(\vec{r}) + \varepsilon_{deoxy}(\lambda)C_{deoxy}(\vec{r}) + \varepsilon_{melanin}(\lambda)C_{melanin}(\vec{r}), \qquad 6.1$$

where $\varepsilon_{oxy}, \varepsilon_{deoxy}$, and $\varepsilon_{melanin}$ are extinction coefficients for oxygenated hemoglobin, deoxygenated hemoglobin, and melanin, respectively, and $C_{oxy}, C_{deoxy}, C_{melanin}$ are their corresponding concentrations. The concentration of chromophores can be calculated by solving the system of linear equations for at least three wavelengths. It can be assumed that the bloodless epidermis is not affected by the oxygenation changes, thus, the last term of the Equation 6.1 is constant and does not depend on the induced hemodynamic changes. Besides, the athymic nude foxn1 mouse model used in this study has a negligible amount of melanin in the skin, therefore, optoacoustic signal attributed to melanin can be neglected. Following the assumption, that only oxy- and deoxyhemoglobin will partake in the hemodynamic changes, the optoacoustic signal in each location can be expressed as follows:

$$p_0(\vec{r},\lambda) = \Gamma\phi(\vec{r},\mu_a,\mu_s,g,\lambda)\left(\varepsilon_{oxy}(\lambda)C_{oxy}(\vec{r}) + \varepsilon_{deoxy}(\lambda)C_{deoxy}(\vec{r})\right), \qquad 6.2$$

where Γ is the Grüneisen parameter, and ϕ is the light fluence. For simplicity, the Grüneisen parameter is assumed to be constant and the light fluence equals for both wavelengths. In order to estimate oxygenation changes, a simple ratio between two signals acquired at 515 nm and 532 nm can be sufficient:

$$\frac{p_{0\,532}(\vec{r},\lambda_{532})}{p_{0\,515}(\vec{r},\lambda_{515})} = \frac{\varepsilon_{oxy\,532}C_{oxy}(\vec{r})+\varepsilon_{deoxy\,532}C_{deoxy}(\vec{r})}{\varepsilon_{oxy\,515}C_{oxy}(\vec{r})+\varepsilon_{deoxy\,515}C_{deoxy}(\vec{r})} = \frac{\varepsilon_{oxy\,532}+\varepsilon_{deoxy\,532}\,{}^{C_{deoxy}(\vec{r})}\!/_{C_{oxy}(\vec{r})}}{\varepsilon_{oxy\,515}+\varepsilon_{deoxy\,515}\,{}^{C_{deoxy}(\vec{r})}\!/_{C_{oxy}(\vec{r})}}. \qquad 6.3$$

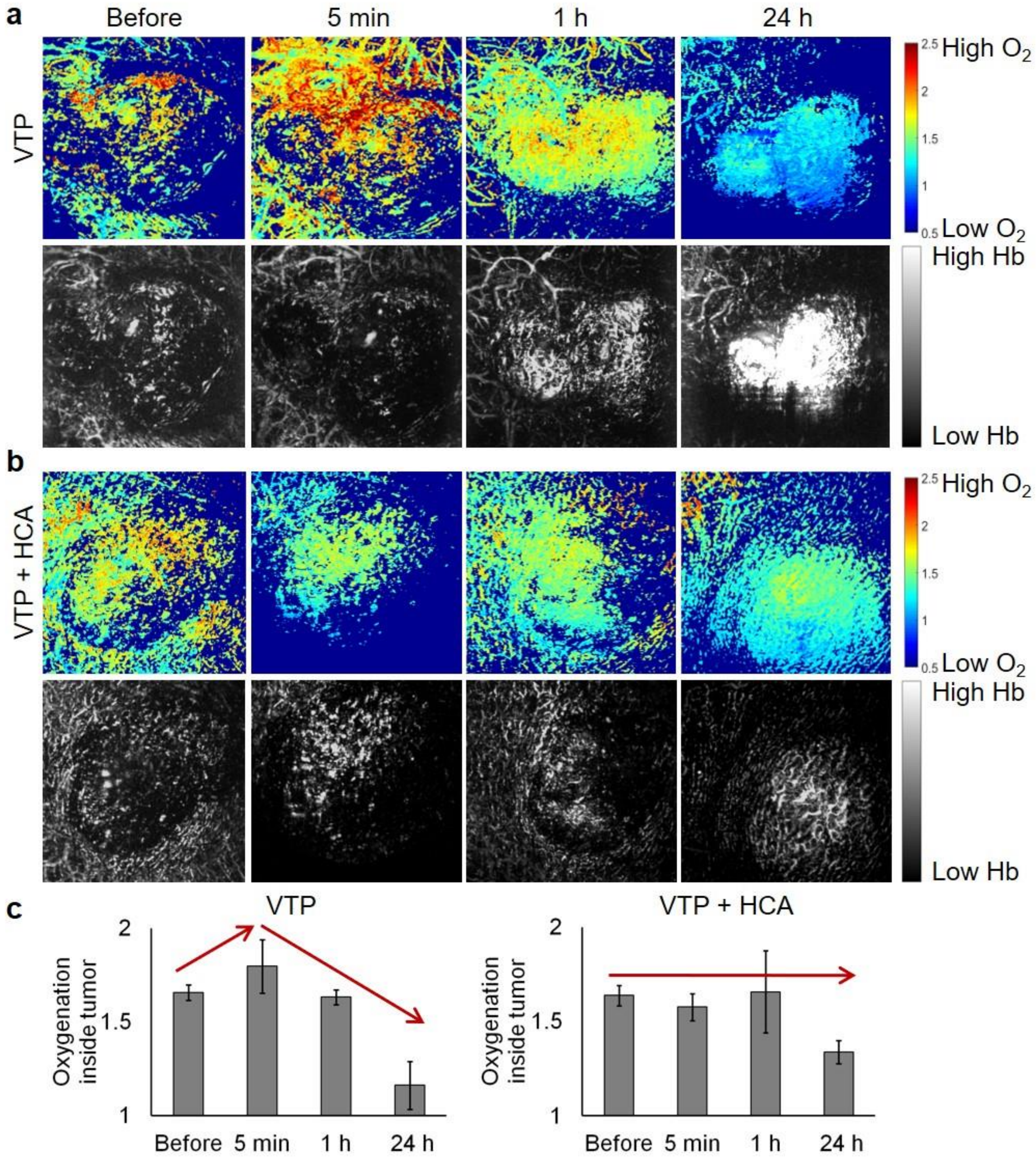

Figure 6.3 CT26 tumor microvasculature oxygenation assessed by DW RSOM. a) top row - MIP images (top view) of the oxygenation ratio before and after WST-11 VTP. Red color corresponds to higher oxygenation values, blue – to lower. Bottom row – images of the microvasculature morphology acquired at 532 nm wavelengths before and after WST-11 VTP. b) top row - MIP images (top view) of the oxygenation ratio before and after WST-11 VTP and blocking with the nitric oxide scavenger HCA. Red color corresponds to higher oxygenation values, blue – to lower. Bottom row – images of the microvasculature morphology acquired at 532 nm wavelengths before and after WST-11 VTP and blocking with the nitric oxide scavenger HCA. c) quantification analysis performed on oxygenation ratio change over time induced by VTP (left) and VTP with HCA blocking (right). N = 3. Adapted from Haedicke, Agemy, Omar, Berezhnoi et al. [191]. © 2019 Springer, Nature Biomedical Engineering. Reproduced with permission.

Therefore, the ratio-signal calculated from the absorption maps acquired at 515 nm and 532 nm can be used for evaluation of oxygenation changes in the skin.

Figure 6.3 shows the response of the tumor microvasculature to the vascular targeted therapy (Figure 6.3a) and VTP and blocking agent based on the nitric oxide scavenger HCA (Figure 6.3b). The top row in Figure 6.3a visualizes oxygenation ratio changes recorded over the time span of 24 h. Clear increase in vascularization and oxygenation ratio at 5 min after treatment of the tumor with a 753 nm laser indicates strong reperfusion after the effect of the therapy, which is followed by a die-away trend at 1 h and 24 h. The die-away trend indicates necrosis of the tissue induced by the distraction of the tumor surrounding microvasculature (Figure 6.3a, bottom row) and, therefore, reduced supply of nutrient and oxygen. The analysis of the oxygenation ratio in the tumor microvasculature containing WST-11 and scavenger HCA displays steady values of oxygenation with a dip at 24 h.

The results of the oxygenation assessment in the tumor and surrounding microvasculature in response to VTP show a great promise for imaging of functional and morphological effects of oncological studies by DW RSOM. Furthermore, they show promise for translation of the technique to human studies to monitor metabolic activity in the skin.

6.3. Oxygenation measurements in human

In order to study the performance of DW RSOM for assessment of the oxygenation in the human skin, the DW RSOM system was utilized to monitor fast oxygenation changes in the human microvasculature induced by a post-occlusive reactive hyperemia (PORH) test. Currently, changes in tissue oxygenation from a PORH test are conventionally assessed with (NIRS), which has shown a great promise for mapping cerebral oxygenation and oxygenation of skin affected by the peripheral disease and claudication of the vasculature. However, NIRS is 2-dimensional and limited by poor resolution, which does not allow visualization of the fine vasculature, and which, however, is crucial for assessing 3D maps of the skin microvasculature oxygenation [194]. UB RSOM operating at single wavelength has shown its ability to capture elaborate images of the skin microvasculature at previously unattainable depth-to-resolution ratio, enabling label-free assessment of skin inflammation and other morphological changes triggered by progression of psoriasis [198], measurements of systemic sclerosis-relevant biomarkers [95], and assessment of heat-induced dermal vasodilation at microvessel resolution [176].

It also has been shown that photoacoustic microscopy could be utilized to monitor oxygenation changes in human skin induced by an occlusion test at the resolution of 70 µm (lateral) and 54 µm (axial) and of 5 min scanning time to acquire 3D data [88]. The system employed two lasers operating at 561 and 570 nm wavelengths. Oxygenation changes attributed to occlusion test were extracted from maximum amplitude projection of cross-sections of the skin rather than from 3D reconstructed data sets, thus, significantly limiting spatial dimensionality of oxygenation measurements to one dimension. Besides, acquired cross-sections were not interleaved, but rather each cross-section was scanned separately at each wavelength.

In Section 6.2.2, it has been presented that dual-wavelength optoacoustic system employing 515 nm and 532 nm lasers is able to monitor relative gradient of oxygenated hemoglobin in tumors and its surroundings in nude – outbred athymic mouse skin triggered by VTP. However, the snapshots of the mouse skin were taken before VTP, 5 min, 1 h and 24 hours after VTP [191], while assessment of rapid oxygenation changes in human skin microvasculature induced by PORH requires scanning times under 1 minute. Although microvascular oxygenation showed clear response to VTP therapy, the sensitivity of the system to these changes requires further investigation, especially in human studies. Besides, in human skin imaging, the prominent melanin layer can interfere with the signals attributed to blood especially in healthy skin at the epidermal-dermal junction making accurate monitoring of the oxygenation a difficult task. Therefore, the problem of melanin segmentation from oxy- and deoxyhemoglobin signal using only 2 wavelengths is yet to be addressed.

Despite of the fact that 515 nm and 532 nm lasers for monitoring of oxygenation changes in mouse models were introduced, the main goal of the work presented in this section is to investigate whether DW RSOM is sensitive enough to be utilized for monitoring of oxygenation changes induced by the PORH test in human skin *in vivo* at high resolution in 3D. Therefore, the DW RSOM system was investigated for ability to retrieve oxygenation changes induced by PORH test in the capillaries – the smallest vessels of the human body, and dermal microvasculature in human skin *in vivo*. The accuracy of the SO_2 changes acquired by DW RSOM was analyzed and sensitivity metric based on the error propagation was developed. Furthermore, the devised sensitivity metric was used to segment melanin in skin from hemoglobin. From the results of the retrieved oxygenation changes induced by the PORH test, oxygen consumption, time of recovery, time to peak value, and maximal hyperemic response are calculated.

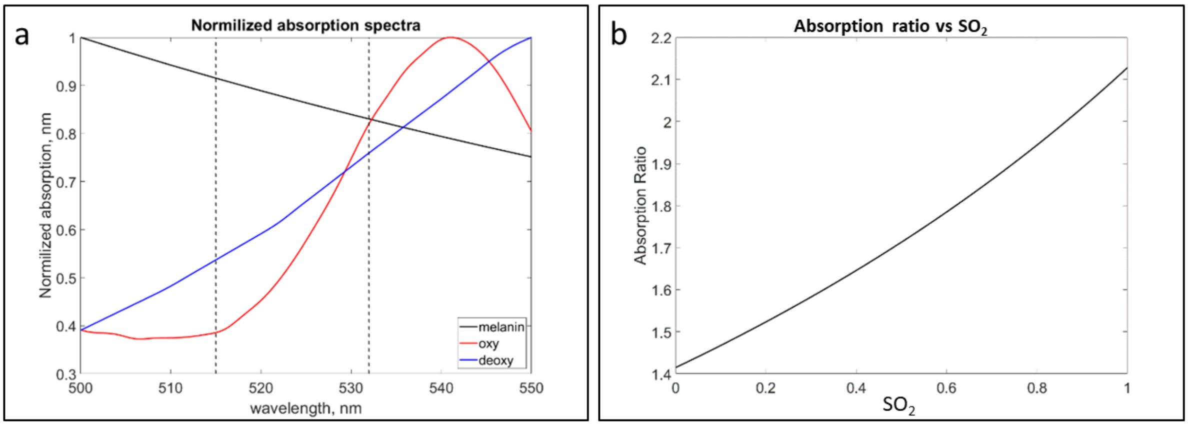

Figure 6.4 DW RSOM operational principles. a) Absorption spectra of melanin, oxy and –deoxyhemoglobin; b) Absorption ratio of 515 and 532 wavelengths as a function of oxygen saturation. Adapted from Berezhnoi et al. [192].

Figure 6.4a shows normalized absorption values of melanin (black), oxy- (red) and deoxyhemoglobin (blue). The two dashed vertical lines illustrate 515 nm and 532 nm wavelengths and the respective absorption values for each of the chromophores at these wavelengths. The oxygen saturation (SO_2) in microvasculature can be calculated as follows:

$$SO_2 = \frac{C_{oxy}}{C_{oxy}+C_{deoxy}}, \qquad 6.4$$

where C_{oxy} and C_{deoxy} are concentrations of oxy and deoxyhaemoglobin in the blood.

In Section 6.2.2 the oxygenation ratio was introduced to evaluate changes in optoacoustic signal attributed to oxygenation variation (Equation 6.3.). The oxygen saturation parameter in the Equation 6.4, can be correlated with the ratio of the signals acquired at 532 nm and 515 nm by substituting expression (6.4) into (6.3):

$$K=\frac{p_{0\ 532}(\vec{r},\lambda_{532})}{p_{0\ 515}(\vec{r},\lambda_{515})}=\frac{\varepsilon_{oxy\ 532}SO_2(\vec{r})+\varepsilon_{deoxy\ 532}(1-SO_2(\vec{r}))}{\varepsilon_{oxy\ 515}SO_2(\vec{r})+\varepsilon_{deoxy\ 515}(1-SO_2(\vec{r}))}. \qquad 6.5$$

The graph in the Figure 6.4b represents the ratio as a function of oxygen saturation. Since the SO_2 is a relative parameter that lays in the range from 0 to 1, the ratio values can be estimated to be in the range from 1.42 to 2.12. A similar ratio can be calculated for melanin signal at 532 nm and 515 nm wavelengths, which results in the melanin ratio equal to 1.1 and does not overlap with the oxygenation ratio. Alternatively, the SO_2 parameter can be expressed analytically as a function of the oxygenation ratio:

$$SO_2=\frac{\varepsilon_{oxy\ 532}-K\cdot\varepsilon_{deoxy\ 532}}{K\cdot\varepsilon_{oxy\ 515}-K\cdot\varepsilon_{deoxy\ 515}-\varepsilon_{oxy\ 532}+\varepsilon_{deoxy\ 532}}= \qquad 6.6$$

$$\frac{\varepsilon_{oxy\ 532}-\frac{p_{0\ 532}}{p_{0\ 515}}\cdot\varepsilon_{deoxy\ 532}}{\frac{p_{0\ 532}}{p_{0\ 515}}\cdot\varepsilon_{oxy\ 515}-\frac{p_{0\ 532}}{p_{0\ 515}}\cdot\varepsilon_{deoxy\ 515}-\varepsilon_{oxy\ 532}+\varepsilon_{deoxy\ 532}}.$$

In order to assess changes of the oxygenation in the forearm skin microvasculature, the optoacoustic signals were acquired over 4×1 mm^2 (FOV) for approximately 200 s prior to the application of the occlusion. The acquisition continued for 270 s before the cuff was released at 470 s followed by a strong hyperemic response in the skin microvasculature and stopped at 750 s. The similar acquisition protocol was followed in the assessment of the oxygenation changes in the proximal of the finger nailfold. The acquisition time before the occlusion was 150 s in order to ease the experiment inconvenience for the volunteers. The cuff was released at 400 s and the imaging was finished at 700 s.

The composite of the reconstructed images for each scan was color-coded to represent the 515 nm image in the green channel and 532 nm image in the red channel. Deoxygenated hemoglobin has higher absorption at 515 nm, while oxygenated hemoglobin absorbs more at 532 nm. Thus, the decline in the oxygenation of the blood will lead to prevalence of the green color in the overlay image, whereas saturation of the red color is attributed to the increase of the oxygenation.

For quantitative analysis of the oxygenation changes, the oxygen saturation was calculated for each reconstructed data set following the Equation 6.6. Furthermore, to estimate the accuracy of the SO_2 measurements obtained by DW RSOM, for each oxygen saturation image a sensitivity metric based on the error propagation analysis was derived. The variance of the calculated SO_2 can be estimated from the variances of the data acquired at 515 nm and 532 nm:

$$dSO_2{}^2 = \left(\frac{\partial SO2}{\partial p_{0\ 532}}\right)^2 dp_{0\ 532}{}^2 + \left(\frac{\partial SO2}{\partial p_{0\ 515}}\right)^2 dp_{0\ 515}{}^2. \qquad 6.7$$

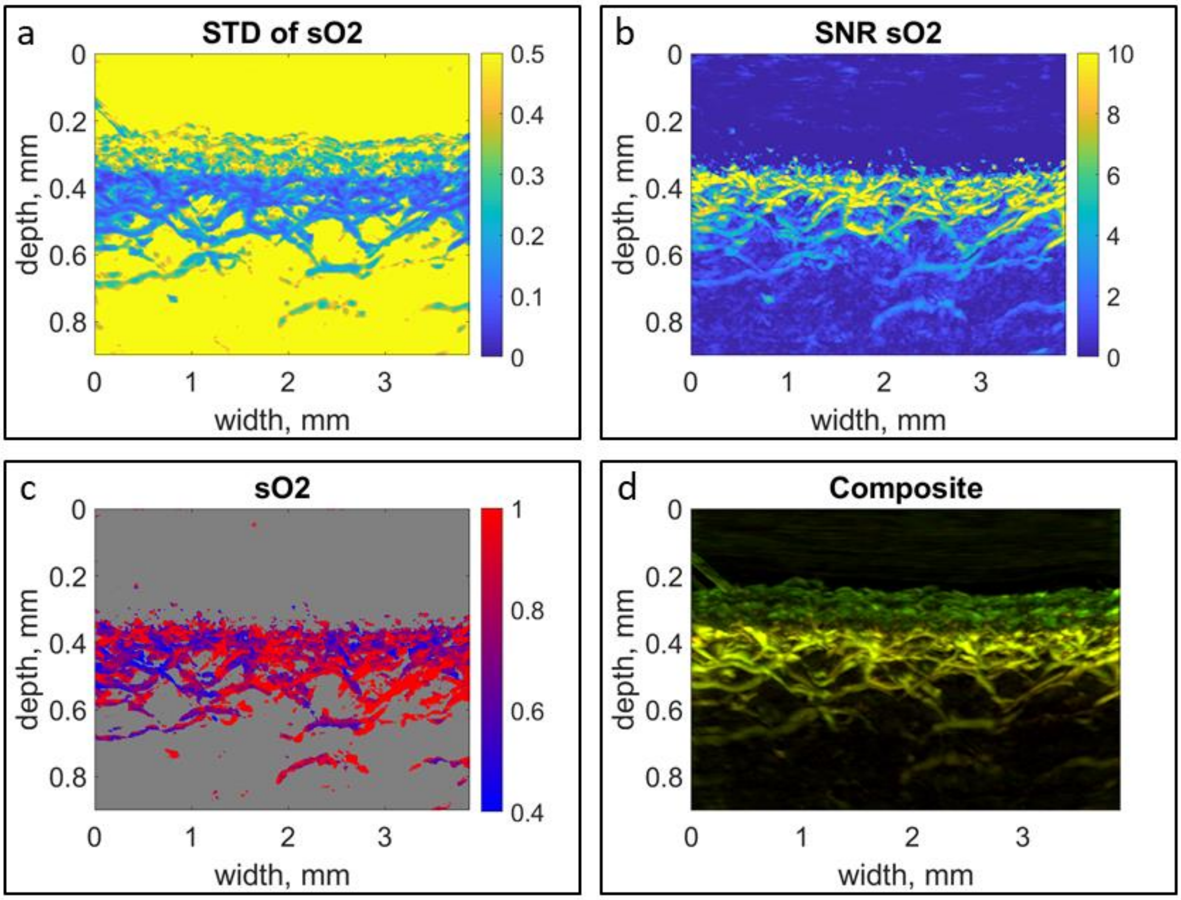

Figure 6.5 Noise analysis and sensitivity of the DW RSOM system to oxygen saturation changes. a) The map of the standard deviation of the oxygen saturation in the human skin measured by DW RSOM. The STD was calculated by propagating the standard deviation error values from the reconstructed data acquired at 515 nm and 532 nm. The lower error values correspond to the strong optoacoustic signals of skin microvasculature, melanin in epidermis and hair. b) Signal-to-Noise ratio map of SO_2 values. The SNR map allows clear segmentation of haemoglobin-rich skin microvasculature from melanin signal and estimation of the sensitivity to SO_2 changes. c) oxygen saturation map of skin microvasculature segmented based on SNR set above 2. SO_2 map shows oxygenation gradient between arterioles and venules. d) Composite image of the reconstructed data acquired at 515 nm (green color) and 532 nm (red color). Due to higher absorption of melanin at 515 nm then at 532 nm, signal from melanin appears in green, while for haemoglobin the absorption is higher for 532 nm. Adapted from Berezhnoi et al. [192].

The variance of the reconstructed optoacoustic signals was measured for each of the wavelength by selecting an ROI above the skin surface where no absorbers are expected and the signal is attributed to noise. The SO_2 images were thresholded based on the pre-selected

SNR value. Next, the mean SO_2 values from the whole values attributed to blood were calculated for each of the images.

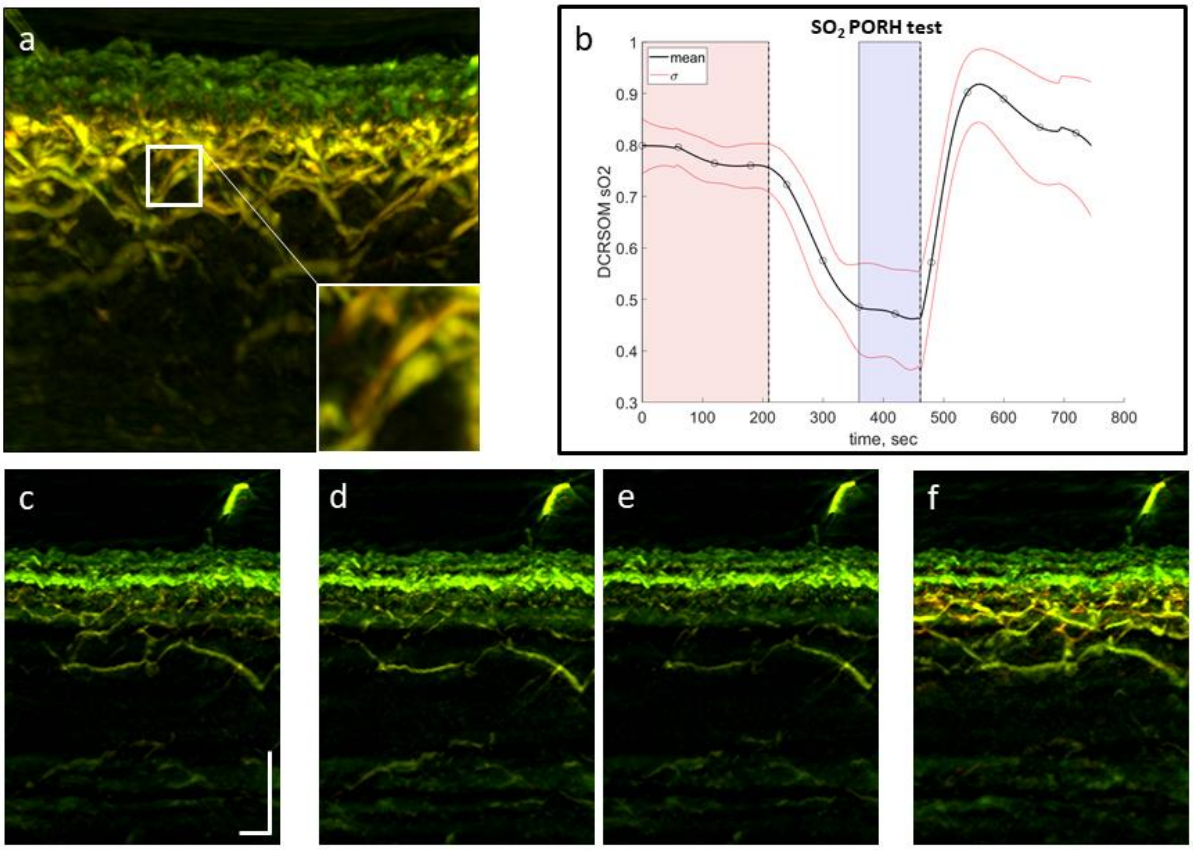

Before occlusion During occlusion After occlusion

Figure 6.6 Oxygenation changes in the dermal microvasculature of the forearm. a) Dermal microvasculature acquired at 515 nm - green color, and 532 nm - red color; the inset emphasizes the ratio difference between vessels; b) oxygen saturation changes before systolic occlusion (0-205 s), during (206-460 s) and after (460-750 s), the vertical dashed lines mark the application and release of the cuff; the oxygen saturation values were acquired using blood gas analyser: the area shaded in red corresponds to the oxygen saturation of 85-90%, the area shaded in blue corresponds to the oxygen saturation values of 40-60%. c-f) Forearm skin oxygenation changes images (4 images, before - 2x during - after). Scale bars 500 µm. Adapted from Berezhnoi et [192].

Figure 6.5 demonstrates the results of the derived sensitivity metric for estimation of the accuracy of the oxygenation measurements. The standard deviation of the SO_2 map calculated according to the Equation 6.7 is shown in Figure 6.5a. The highest standard deviation is observed in the regions above the skin surface due to lack of absorbers and below the upper vascular plexus. High values of the STD below the upper vascular plexus in dermis are attributed to the increased sparsity of the microvasculature as well as to decreased light fluence. Figure 6.5b represents signal-to-noise ratio of the SO_2 values. It can be observed that the region of the epidermis where strong melanin signal is present has low SNR values except small dots which are attributed to the tips of the capillary loops. Based on the extracted SNR values a powerful thresholding approach was developed in order to segment hemoglobin signal from the signal attributed to melanin, to bring up small structures obstructed by the melanin layer, and to remove the background endorsed by strong presence of noise (Figure 6.5c). The oxygen saturation values for each acquisition point were calculated as a mean value of the signal from the region segmented based on the sensitivity metric.

Figure 6.6a illustrates the side view of the human forearm skin imaged using dual-wavelength RSOM. The image is a maximum intensity projection of 3D reconstructed data acquired at 515 nm (green) and 532 nm (red). Therefore, the overlay of two images acquired at 515 nm and 532 nm wavelengths represents the gradient of oxygenation, so that red color corresponds to more oxygenated blood while green to less oxygenated. Such colormap allowed to differentiate venules and arterioles based on their appearance in different shades of green and red, which is shown in the inset of Figure 6.6a.

The melanin layer is clearly visible and appears in green, since the absorption of melanin at 515 nm wavelength is stronger than its absorption at 532 nm. Furthermore, due the fact the dermal papillae is characterized by the ridged-like structure, taking the maximum intensity makes the tips of the capillary loops appear inside the melanin layer as they are inside the epidermis.

Figure 6.6c-d shows how the oxygenation changes in the forearm microvasculature applying systolic occlusion to the forearm. Figure 6.6c corresponds to the oxygenation state before using the cuff to restrict arterial blood flow. Figure 6.6d,e illustrate the decrease in the oxygenation of the dermal microvasculature as a result of applying the cuff above the systolic pressure. The systolic occlusion leads to the colors turning to the shades of green, which corresponds to decrease in oxygenation. Furthermore, it can be seen that in Figure 6.6d,e some of the microvasculature disappeared, which is also a result of the occlusion. Figure 6.6f is taken after the release of the cuff and shows that microvasculature turning red indicating the increase in oxygenation, reappearance of the vessels and emergence of the new ones.

Figure 6.6b depicts the results of the oxygenation change measured using DW RSOM in the forearm skin of 5 healthy volunteers. The mean oxygenation values obtained using the DW RSOM system are represented by the black curve, while the red curves show the standard deviation. Two dashed vertical lines mark the beginning of the occlusion (200 s) and the end 470 (s). Red area denotes SO_2 values measured with blood gas analyzer prior the occlusion, while blue shaded area corresponds to the SO_2 values during the occlusion. The SO_2 values measured in the forearm before the occlusion were in the range 85-95%, while during the occlusion they were in the range 40-60%.

The oxygenation values obtained before the occlusion remain constant and correspond to around 80% percent oxygenation. The DW RSOM oxygenation values are slightly lower than the SO_2 obtained with blood gas analyzer. This can be explained by the fact, that the gas blood analyzer relies on the extracted blood from the damaged microvasculature caused by a small syringe needle, which is used to draw the blood. The main contribution to the drawn blood is made by the arteries due to higher pressure in them, therefore more blood is spilled. As a result, the SO_2 values from the blood gas analyzer show higher values because of the dominance of the arterial blood. Immediately after beginning of the occlusion, the oxygenation of the forearm microvasculature starts to fall for approximately 150 s until it reaches a plateau. The oxygenation values obtained with DW RSOM are in the range from 40% to 60%, which is in a good agreement with results from the blood gas analyzer. The release of the cuff is followed by a rapid hyperemic response and increase in the microvasculature oxygenation. There is a prominent peak of the oxygenation, which exceed the oxygenation values before the occlusion. After reaching the peak, oxygenation declines over time to its original values.

The graph in Figure 6.6b allows to retrieve occlusion parameters measured by the DW RSOM system. Oxygen consumption rate (VO_2) is an important physiological parameter related to metabolic activity and describes the rate of oxygen uptake by the tissue. VO_2 parameter was calculated as the speed of the SO_2 decrease right after beginning of the occlusion with a value of 0.25. The time interval between release of the cuff and SO_2 reaching initial values describes time of recovery (t_R) and is equal 38 s. Another parameter extracted from the graph in Figure 6.6b is time-to-peak value (t_M). Time-to-peak value defines the interval after release of the cuff until 95% of the signal peak values are reached.

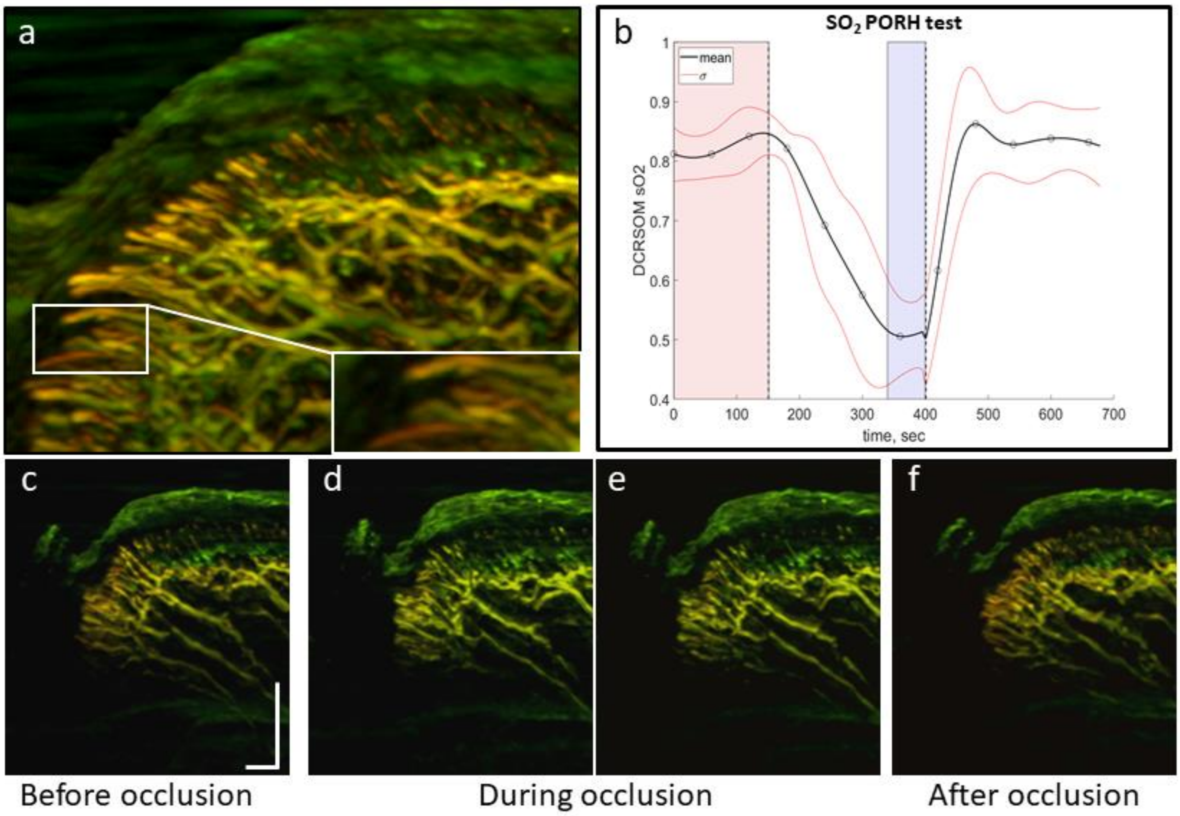

Figure 6.7 Oxygenation changes in the nailfold microvasculature. a) Nailfold microvasculature acquired at 515 nm - green color, and 532 nm - red color; the inset emphasizes the ratio difference between capillary loops; b) oxygen saturation changes before systolic occlusion (0-150 s), during (151-400 s) and after (400-700 s), the vertical dashed lines mark the application and release of the cuff; the oxygen saturation values were acquired using blood gas analyzer: the area shaded in red corresponds to the oxygen saturation of 85-90%, the area shaded in blue corresponds to the oxygen saturation values of 40-60%; c-f) nailfold skin oxygenation changes images (4 images, before - 2x during - after). Scale bars 500 µm. Adapted from Berezhnoi et [192].

Following a similar imaging procedure as for the forearm, the proximal of the human nail fold was imaged with DW RSOM. Figure 6.7a shows a representative image of the skin microvasculature including the capillary loops. The dominant red color of the vessels indicates higher concentration of the oxygenated hemoglobin in the blood and corresponds to the arterioles, while vessels of the dominant green color are associated with venules. The capillary loops are horizontal at the proximal of the nailfold raising straight up further away. Due to the limited acceptance angle of the transducer (60°), the capillary loops seem to fade away when they ascend vertically to the skin surface. When the capillary loops are at the right angle to the skin surface, only the optoacoustic signal from their tips is detected by the ultrasound transducer.

The inset in Figure 6.7a shows a zoomed-in section of the capillary loops horizontal to the imaging plane. Close up view allows to clearly distinguish variation in oxygenation for different vessels. Figure 6.7c,d shows the images before systolic occlusion of the blood flow in the forearm (Figure 6.7c), two images during the occlusion (Figure 6.7d,e), and the image after release of the cuff (Figure 6.7f). As it has been discussed above for the forearm skin microvasculature, the colormap changes to the dominant green color during the occlusion indicating the decrease of oxygenation in the microvasculature. Release of the occlusion followed by the strong hyperemic response and increase in oxygenation is depicted in Figure 6.7f. The capillary loops get saturated with oxygen after being depleted during the occlusion and appear in red-dominant colormap.

The graph in Figure 6.7b shows the quantitative results of the oxygenation change in the proximal of the nail fold as a result of the systolic occlusion applied to the forearm. The black curve shows the mean DW RSOM SO_2 values calculated for 5 volunteers, red lines depict the standard deviation. Two dashed vertical lines mark the beginning of the occlusion (150 s) and the end (400 s). Red area denotes SO_2 values measured with blood gas analyzer prior the occlusion, while blue shaded area corresponds to the SO_2 values during the occlusion. The SO_2 values measured in the fingertip before the occlusion were in the range 85-95%, while the SO_2 values during the occlusion were in the range 40-60%.

The DW RSOM SO2 values before the occlusion are in the range 77% -90%. The systolic occlusion is followed immediately by the rapid decrease of the nailfold microvasculature oxygenation for around 180 s reaching the lowest DW RSOM SO_2 of 43%-55%. Therefore, the oxygen consumption rate (VO2) is equal to 0.18 and is slower than in the forearm. After the release the microvasculature oxygenation quickly restores its original values experiencing a less prominent peak due to hyperemic reaction. The calculated timer of recovery and time-to-peak value are 54 s and 86 s.

In this section DW RSOM has been utilized to resolve oxygen saturation changes induced by PORH test in the human skin *in vivo*. In order to estimate accuracy of the DW RSOM in retrieving oxygenation changes a powerful metric based on the error propagation analysis and thresholding of the signal attributed to hemoglobin based on calculated SNR maps. Thus, having only 2 wavelengths, DW RSOM offers clear separation of the melanin signal from hemoglobin, reducing number of wavelengths, which are required to separate chromophores using linear unmixing, from three to two wavelengths.

The results of the PORH test clear oxygenation changes before, during, and after the occlusion. The retrieved oxygenation graphs resemble very closely the ones retrieved using NIRS. Furthermore, the oxygenation values calculated from DW RSOM measurements are in a good agreement with the results obtained from Blood Gas Analyzer.

6.4. Conclusion

In this chapter RSOM equipped with a 500 Hz OPO and dual-wavelength RSOM were introduced for assessment of skin microvasculature oxygenation. The ability of the OPO to tune emitted wavelengths in a broad optical range allows multi-wavelengths imaging of skin and has been extensively studied in our group [2,96] . However, the low resolution rate of the emitted light pulses and strong energy variations may lead to misinterpretation of the data, because for quantitative analysis it is required to know the deposited heat energy (see Section 3.2). In order to improve the scanning times, a 500 Hz OPO was employed in an RSOM system. The energy fluctuations were compensated by tuning of the wavelengths for each B-plane instead of per pulse, which reduced per-pulse energy fluctuations. Furthermore, the recorded optoacoustic signals were compensated by the pulse energies recorded with a photodiode. In order to implement such improvements a precise control of the OPO was developed and implemented in the GUI along with an unmixing algorithms and visualization of the images. Precise control of the OPO and robust compensation of the energy fluctuations enabled imaging of the oxygenation of the mouse skin microvasculature at high resolution; furthermore, venules and arterioles were clearly differentiated based on their oxygenation values.

In order to further increase the imaging speed and reduce the complexity attributed to operation of the OPO in the oxygenation measurements assessed by RSOM, the dual-wavelength RSOM system was developed implementing fast, high energy, single-wavelength lasers operating at 515 nm and 532 nm. First, the DW RSOM was utilized to study the outcomes of the novel anti-angiogenic cancer therapy VTP in mouse models. A complex pattern of the oxygenation changes over 24 h time span was observed at single vessel resolution. Specifically, oxygenation decrease induced by VTP was observed 1 h after the therapy up to 24 h, which is consisted with the studies performed by MSOT [199]. In comparison to the previous reports, for the first time an initial boost of oxygenation due to the destruction of the vessels by VTP was recorded by DW RSOM and analyzed. Overall, DW RSOM is anticipated to significantly benefit pre-clinical studies of oncological therapies by providing non-invasive, high-resolution, in-depth assessment of cancer parameters.

Second, the performance of the DW RSOM was evaluated to conduct human skin oxygenation studies. DW RSOM showed that fast oxygenation changes in the human skin microvasculature induced by a standardized PORH test can be evaluated. Furthermore, oxygen consumption, time of recovery, and time to peak value were extracted from the oxygenation graphs. The oxygenation changes are evaluated in forearm skin and in the capillary loops and microvasculature of the nailfold. Assessment of the capillaries proved the system to be capable of retrieving oxygenation from the smallest vessels in human body. The accuracy of the DW RSOM system in oxygenation measurements was estimated by a developed sensitivity metric, which was based on the error propagation analysis. The sensitivity metric provided information on the reliability of the 3D oxygenation maps revealing the noise level in each voxel of the reconstructed optoacoustic signals. Moreover, the metric facilitated segmentation of the optoacoustic signals attributed only to blood excluding melanin. It helped to improve the visualization of the small capillaries at the epidermal-dermal junction and reduced the error of the oxygenation calculations.

Compare to previously reported results, the developed DW RSOM system provides for the first time 3-dimensionals maps of the oxygen saturation at unpreceded resolution through the whole skin depth visualizing oxygenation in the skin microvasculature including the capillaries. The results of the oxygenation assessment in the human and mouse skin highlight the impressive potential of DW RSOM for basic and clinical investigations. These results demonstrate new possibilities for functional measurements of the skin and pave the path for the future translation of the technique to the clinical bedside.

7. Conclusion and future outlook

This chapter is dedicated to give a conclusive summary on the objectives stated in Section 1.5. Furthermore, an outlook on future possible developments of the raster-scanning optoacoustic mesoscopy technique with the aim to outline possible technical improvements for facilitating translation of the technique to the clinical applications of skin imaging is discussed.

7.1. Conclusive summary

Skin conditions and manifestations of systemic and metabolic disorders in skin result in a significant complication of one’s life, may lead to death, and bear a substantial economic burden. High incidence of skin cancers and their high aggressiveness are often referred as a melanoma epidemic and require immediate action to reduce the mortality rate among the patients. Atopic eczema, psoriasis and other inflammatory diseases are closely linked to morphological and functional changes in microvasculature, however, their underlying mechanisms are still not well understood. Cardiovascular diseases and diabetes are often accompanied at early stage by dysfunction of microvascular bed, impaired metabolic activity of subcutaneous fat and other skin features. Therefore, early diagnosis and monitoring of functional and structural alterations in skin may provide valuable insights into the disease progression and lead to improved therapeutical measures. As it was outlined in Section 1.4, optoacoustics offers several crucial advantages compare to other technique utilized for *in vivo* skin imaging: prominent optical contrast based on the light absorption, unprecedented depth-to-resolution ratio, differentiation of skin chromophores by multi-wavelength excitation. The central goal of this thesis was to advance the RSOM technique further towards multi-wavelength acquisition in order to increase the number of detected skin chromophores and visualized skin features, and towards extraction of functional changes of the skin microvasculature, such as blood volume and oxygenation. Thus, to elaborate on the current progress achieved in this work, the summary of the thesis is addressed in the objectives formulated in Section 1.5:

- **Development of a hand-held multiple laser optoacoustic mesoscopy system, including detectors, optics and software control that can achieve previously unmet capacity for multi-wavelength acquisition.**

In order to achieve this goal, the multispectral RSOM system was upgraded and described in detail in Section 3.4. The main technical advances of the system included incorporation of three light sources: optical parametric oscillator (OPO) and two fast single-wavelength lasers operating at 532 nm and 515 nm. Simultaneous operation of all three lasers was achieved by the smart coupling of all three lasers into the fiber bundle and by the developed software control to facilitate operation and switching between laser sources depending on an application and imaging procedure. The spectral range of the OPO spanning from 420 nm to 2000 nm enabled analysis of the absorption spectra of skin chromophores including oxy- and deoxyhemoglobin, melanin, water, and lipids. In addition to the 55 MHz transducer utilized primarily for detection of oxy-, deoxyhemoglobin, and melanin, the performance of the UWSB RSOM system was enhanced by incorporating the highly sensitive 24 MHz transducer. The 24 MHz transducer facilitated detection of the optoacoustic signals attributed to lipids and water, which are characterized by the low absorption coefficient. The designed casing and detachable interface unit along with an upgraded articulated arm significantly simplified positioning and handling of the scanning head, which benefited imaging procedure and considerably reduced stress on the volunteers and patients involved in imaging studies ultimately leading to the improved image quality.

- **Development of a method for robust monitoring of rapid blood volume changes caused by external stimuli in skin microvasculature at single-vessel resolution.**

For the first time a handheld clinical raster-scanning optoacoustic mesoscopy system was utilized to study hyperthermia-induced microvascular perfusion changes in human skin at single vessel resolution through the whole skin depth. In order to provoke microvasculature response to local heating, a temperature control system was designed. The TCS provided precise control over the coupling medium temperature while the imaging procedure was not affected. RSOM showed a great capacity for 3D visualization of blood volume changes in skin microvasculature in human forearm in response to local heating. At high precision it has been revealed that the diameter of vessels grows 1.56-fold while total blood volume multiplies up to two- to three-fold. Such results are in a good agreement with previous reports on heat-induced microvasculature changes obtained by LDPI or LSCI in bulk tissue, but go significantly further by assessing single vessel dynamic throughout the skin. Furthermore, the RSOM system has visualized in great detail response of microvasculature to topical application of pharmaceuticals to the skin.

The performance of RSOM in examining the dynamic of single microvessels makes the technique particularly suitable for reveling and understanding mechanisms associated with vasodilation and recruitment of microvessels in response to external stimuli. The heat- and pharmaceuticals-induced vasodilation and blood volume dynamic changes for the first time assessed by RSOM highlighted remarkable capacity of RSOM for clinical investigations.

- **Increasing the number of detected skin chromophores by state of the art ultra-wide spectrum and bandwidth RSOM system capable of acquiring signals at wavelengths from VIS to SWIR and of exploring the absorption properties of skin.**

In order to tackle the challenge of increasing the number of detected chromophores, the unique absorption spectra of skin chromophores were thoroughly studied over a broad spectral range. To facilitate their detection, the ultra-wide spectrum and bandwidth RSOM system was developed and described in detail in Section 3.4. In order to perform multi-wavelengths imaging, three lasers were employed to detect spectral signatures of the skin intrinsic chromophores over a broad spectral range from VIS to SWIR. Two fast repetition rate single wavelength lasers operating at 515 nm and 532 nm were incorporated in the system to detect melanin, oxy- and deoxyhemoglobin with implication that the approach of using two fast repetition rate lasers can benefit monitoring of oxygenation changes in skin at high resolution. Due to the drastic decrease of the absorption of hemoglobin at wavelength from 580 to 700 nm, the imaging of melanin was accomplished at 650 nm where the contrast of melanin signal is the strongest compare to the signal from blood. Potent spectral signatures of lipids around 1210 nm and water around 1450 nm facilitated their detection using the idler regime of the OPO. Previously, RSOM detected oxy- and deoxyhemoglobin and melanin content in skin [96]. However, for the first time it has been shown that the UWSB RSOM system can perform non-invasive detection of lipid and water distribution complemented by detection melanin, oxy- and deoxyhemoglobin.

The separation of signals of the biomolecules is a difficult task since their corresponding absorption spectra often overlap. In this work this problem was mitigated by utilizing a broad spectral range in which the contrast of detected chromophores can be optimized by selection of appropriate spectral regions. For instance, contrast for melanin signal is optimized by using wavelengths closer to NIR window, where the absorption of hemoglobin is reduced. Lipids signal can be negligible compare to water signal at 1450 nm, while both water and lipids show strong signals at 1210 nm. Thus, in this work it has been shown that the signals from different skin chromophores can be used to facilitate spectral unmixing or, in some instances, can be separated even without the need for spectral unmixing, assuming that the signals from other chromophores are negligible.

- **Concurrent imaging of the main skin features *in vivo*: skin microvasculature, sebaceous glands, subcutaneous fat, the melanin layer, the whole hair, and water content.**

Cutaneous features can be imaged based on their molecular composition. For example, skin microvasculature is rich with oxy- and deoxyhemoglobin, hair and stratum basale are pigmented by melanin, subcutaneous fat and sebaceous glands are characterized by the high lipid content, while water is distributed almost homogeneously throughout the dermis and exhibits decreasing concentration in epidermis towards the skin surface. In this work, by taking advantage of the strong sensitivity of UWSB RSOM to the main skin chromophores and attained high depth-to-resolution ratio, the number of skin features, such as dermal microvasculature, melanin layer, the whole hair, sebaceous glands, subcutaneous fat, sebum distribution on the hair shaft, water content in epidermis were visualized at high resolution through the whole skin depth in a complementary manner. The achieved resolution of the UWSB RSOM in revealing, hair, subcutaneous fat and sebaceous glands improved more than two-fold compare to the previous reports. Furthermore, the analysis of the signals detected at 1210 nm on the hair shaft allows to hypothesis that this signal is attributed to the deposition of sebum. The examination of sebum can play an important role in understanding sebum transportation to the skin surface and associated pathologies, including acne and xerosis. The sensitivity of UWSB RSOM to detect optoacoustic signal from the very surface of the hair may facilitate the research of transdermal drug delivery by reaching greater depths compare to microscopy techniques. Besides, epidermal water content visualized at 1450 nm wavelength can help to monitor hydration state of the skin with further implications for assessment of hair loss and xerosis cutis. Examining of oxygenation and dermal microvasculature morphology at 515 nm and 532 nm wavelengths, may be translated to evaluate psoriatic inflammation or oxygen consumption by skin cancers.

Overall, the abilities of the currently available skin imaging techniques cannot offer the performance of visualizing skin features over a broad optical range at high resolution through the whole skin depth achieved by UWSB RSOM. Based on the above summarized results of this thesis, it can be presumed, that the developed technique can help to discover new approaches for diagnosis and monitoring of skin conditions and skin functional changes associated with systemic diseases.

- **Development of a new method for monitoring fast oxygenation changes in skin microvasculature including capillaries (the smallest vessels in the human body).**

This goal was accomplished by integrating two fast-repetition rate lasers operating at 515 nm and 532 nm wavelengths into the UWSB RSOM system. In addition to the previously employed in RSOM systems laser operating at 532 nm wavelength, the exploitation of the 515 nm laser has several advantages, in particular that the overall performance and imaging depth are similar to those achieved by the 532 nm laser. Furthermore, the implementation of two separate cost-efficient lasers allowed interleaved operation and did not increase scanning times, as it would be necessary with a tunable laser. Similar characteristics of the lasers, fast scanning rates and high output light energies are crucial parameters for conducting functional imaging of oxygenation in skin *in vivo*. The performance of the developed DW RSOM was corroborated by revealing a complex pattern of oxygenation changes induced by a novel anti-angiogenic cancer therapy in mouse models and by monitoring oxygenation changes in microvasculature of human skin triggered by an occlusion challenge. The imaging of the outcomes of the anti-angiogenic cancer therapy was performed over a 24 h time span and for the first time identified the initial oxygenation boost at the beginning of the therapy caused by distraction of the microvasculature. Translation of the DW RSOM system to the clinical studies exposed oxygenation changes in human skin microvasculature in 3D throughout the skin depth. Furthermore, owning to high resolution performance of the system, the oxygenation was shown even in the smallest vessels of human body – capillaries, located at the proximal of the nailfold. The analysis of the oxygenation patterns in response to the PORH test revealed that clinically relevant parameters, such as oxygen consumption, time of recovery, and time to peak value can be extracted from the images recorded by DW RSOM. Furthermore, the sensitivity metric of the SO_2 measurements was derived from the acquired data based on the noise propagation analysis. Besides, the derived sensitivity metric led to improved visualization of the microvasculature in the proximity to the epidermis and of the capillaries rising up to the dermal papillae. Melanin segmentation utilizing only two wavelengths can be of a great importance in melanoma imaging to estimate location of melanin rich cells and their proliferation deep in the skin.

7.2. Future outlook

Owning to accomplishments achieved in this thesis a great number of clinical application for raster-scanning optoacoustic mesoscopy can be anticipated. For example, alterations of structure and reactivity of dermal microvasculature are often attributed to early sings of diabetes and cardiovascular diseases, obesity and metabolic syndrome [23–25]. Single wavelength RSOM showed great capacity to monitor structural and functional changes in skin microvasculature at single vessel resolution. Stimulating skin with heat or by applying pharmaceuticals to induce functional changes in the microvasculature can be used to study poorly understood phenomena of vasodilation, vasoconstriction and vascular recruitment [58]. The devised heating method can be easily accommodated in clinic to measure endothelial function of patient affected by diabetes or peripheral vascular disease. Furthermore, single wavelength RSOM may be used to analyze neural responsivity, which involves axon reflex and release of neuro mediators [178,179]. Thermoregulation process are yet to be investigated in single micro vessels, while they can be useful for diagnosis and monitoring of major diseases [186].

Multi-wavelength imaging of key skin components showed by UWSB RSOM paves the way to enabling diagnosis and monitoring of skin conditions and systemic diseases [38,200,201]. Fat morphology imaged by UWSB RSOM can be useful for prediction of cardiovascular diseases, while fat function correlates with insulin sensitivity and weight loss [38]. The dysfunction of lipid-rich sebaceous glands and hydration state of the stratum corneum can be associated with xerosis cutis and loss of hair [39,40]. Altered microvascular hemodynamics, oxygenation and morphology of the skin microvasculature and density of hair follicles are the signs of Type 2 diabetes [42]. The results presented in this thesis show powerful performance of UWSB RSOM to identify skin features such microvasculature, sebaceous glands, whole hair, subcutaneous fat, water content in epidermis. The clear need for comprehensive monitoring of features and functions of skin through the whole skin depth, makes UWSB RSOM indispensable tool that can be used for diagnosis of diseases based on the information and biomarkers acquired by UWSB RSOM.

Certainly, further translation of raster-scanning optoacoustic mesoscopy towards clinical applications will benefit tremendously from technological advances of the technique. The technological advances can be viewed as a many-fold problem. First, NIR and SWIR offer significant improvement in penetration depth compare to visible range due to lower scattering coefficient and increased forward scattering. While the absorption of hemoglobin in NIR is significantly reduced, finding a compromise between penetration depth of light and absorption contrast can benefit visualization of microvasculature at greater depth. SWIR is a relatively less explored spectral region that owns prominent spectral signature of lipids, water and proteins, which are overtones of vibrational modes of C-H, O-H, and N-H bonds, respectively [141,142]. Further efforts towards exploration of SWIR may help identifying proteins, in addition to reported sensitivity to lipids and water by UWSB RSOM. While it has been shown, that in some instances skin chromophores detected by UWSB RSOM can be separated by appropriate selection of spectral regions, spectral unmixing is still required for quantitative imaging. Moreover, ultra-broad optical range used for imaging herein poses even a greater problem for accurate quantification of concentrations of detected absorbers, therefore, new sophisticated models for light fluence compensation will be required.

Second, the functional imaging can greatly benefit from a faster scanning speed without sacrificing the size of the region of interest. The main limiting factors of the scanning speed is a trade-off between complying with maximum permissible exposure limits for the skin and sensitivity of the transducers. On the one hand, the sensitivity of the transducers can be amplified by increasing the size of the detection area. However, in order to continue miniaturization of the system and reducing mechanical stress on the moving parts, smaller detectors are preferable. On the other hand, the sensitivity of the currently employed piezoelectric transducers can be improved by reducing noise. The noise in principle can be decreased by attaching an amplification element directly to the crystal in order to reduce length of the wires and, therefore, induced electromagnetic noise. In recent years, the sensitivity of interferometric sensor utilized for sound detection has been reported to overcome the sensitivity of the conventional piezoelectric transducers when calculated per area while reaching ultra-high bandwidth up to 300 MHz at 110 MHz central frequency [202]. Further development of this technique towards simplification of the detection scheme and multiplexing of multiple sensors may offer fully optical light delivery and acquisition scheme for RSOM.

Recent development of fast light sources that can operate at high repetition rates preserving short pulse width is of great importance for optoacoustic imaging. Light sources based on OPOs can offer broad optical range but are rather bulky, expensive and operate at low repletion rates. Laser diodes have been reported to operate at fast repetition rates providing high quality images of the mouse skin at multiple wavelengths, however, low output energies and their availability only at certain wavelengths insinuate the need for improvement of the technology [203].

Third, as of today, a great progress of the deep learning algorithms showed promising results in analyzing medical images of various radiological modalities. The main bottle neck of the deep learning approaches is the required excessive amount of data to train the network and generate accurate results. Due to the fact that optoacoustic mesoscopy is getting a lot of attention in the medical community, there are several studies that involve few tens of individual generating large amounts of data. Therefore, deep learning approaches can significantly benefit image analysis of UWSB RSOM data, identifying new biomarkers of the diseases from UWSB RSOM images and extracting valuable information not accessible even for a trained person.

Acknowledgements

The time of my PhD studies was a challenging and, at the same time, an inspiring period of my life. The hurdles of which were eased to a great extent by my friends, family, and colleagues. In this section I would like to give my sincere appreciation to all those people who were present in my life during my work at IBMI and who made completing my doctoral studies possible in direct or indirect way.

First of all, my appreciation goes to Prof. Dr. Vasilis Ntziachristos, who, without a tiny doubt, has been the main contributor guiding me through the process of obtaining a doctoral degree. His broad vision, enthusiasm, and experience have always fascinated me. I am grateful to him for allowing me to work independently, establish interdisciplinary collaborations, and always be at the frontiers of the research.

Dr Juan Aguirre was my mentor and group leader during the PhD. He was always there for me when I had struggles with my projects. He helped me to identify problems and find solutions. His ideas have tremendously benefited the results of my work and helped me in the developing of the RSOM technique and its translational aspects to the clinical applications. Our fruitful collaborations and his attentive supervision resulted in numerous papers. I am also thankful to him for his valuable advice on writing papers, project reports and revision of my thesis as well as preparing a presentation for the defence.

I am indebted to my dear groupmates with whom I spent multiple hours performing all sorts of measurement. Dr Benedikt Hindelang has shown supreme endurance and has always been keen on suffering sometimes crazy experiments we performed together. One the fondest memories I have is when we performed an oxygenation challenge breathing low percentage of oxygen from a huge air tank and trying to capture oxygenation changes. Or occluding blood flow in the limbs and drawing the blood from the skin, squeezing, pinching and puncturing ourselves with no pity. Working with Dr Christine Schönmann was always joyful even in the days of a bad mood. She always knew when to give support and a little treat or help with experiments. Dr Hailong He and Dr Lucas Riobo joined our great clinical RSOM group in the middle of my PhD and I am thankful to them for inspiring discussions, shared knowledge and a good time spent in less professional settings outside of work.

Dr Ludwig Prade and I shared an office at the HMGU campus. We both lived outside the city, where we discovered a nice bar in our neighbourhood. There we spent numerous evenings venting about the hardships of being a PhD student. Also, I would like to recognize his valuable assistance in my projects and his deep knowledge in electrical engineering. With Antonis

Stylogiannis I had a privilege to share the office too. Thanks to him Ludwig and I had to buy noise cancelling headphones. However, his assistance during my PhD cannot be overestimated. I am really thankful for his willingness to share/lend equipment or to have rewarding discussions about our projects. Sharing the lab with Francesca and Kaushik has always brighten up my days. They were always eager to talk and share a good laugh about our daily routine. Also, the energy and liveliness radiated by Francesca made me grin on the gloomiest days.

Dr Katja Haedicke and I had performed one of the first experiments using DW RSOM, which was part of her paper published in Nature Biomedical Engineering. Our collaboration later evolved in a friendship I am very fond of and value a lot. She has always been there for me as a colleague and as a friend. I am very happy that I our paths crossed and hope that our friendship will continue.

With Dr Mathias Schwarz I worked at the beginning of my PhD when he was already a senior PhD student working towards the end of the doctorate. I am thankful for his collaboration on multiple projects we worked together including the installation of multispectral laser for an RSOM system in New York.

Dr Gael Diot and Dr Andreas Bühler supervised me at the beginning of my PhD. They helped me to find my path and without them I would not be where I am. Being a newbie in a new city, Gael was very supportive in finding my ways around Munich including the never-ending hustle with accommodation.

I cannot stress enough how many times Dr Dmitry Bozhko has helped in my professional career as well as in personal life. We spent countless hours discussing work related questions or private matters. He was always there for me in my worst and my best times. We have been friends since the University and he was the one who suggested me to apply at IBMI, for which I am infinitely grateful to him. It would take about the same number of pages as this dissertation to describe all the adventures we have had together.

My IBMI life had started with my first interview, which was conducted by Dr Murad Omar. I still remember the questions I was asked and how supportive Murad was in my PhD. He was always the person I would come to ask all sorts of technical questions about the technique and was always eager to share his extensive knowledge.

Dr Rebecca Favaro and I worked together on Innoderm project, for which I was assigned rather unexpectedly to work on the development of optoacoustic microscope for skin imaging. Thank you to Rebecca for helping me with the arrangement of my multiple business trips to Humanitas University and being accommodating and welcoming. I will never forget the great food in the local Mensa and Aperitivos in the evenings.

I had a pleasure to work with Christian Zakian and was fascinated by his ability to explain even complicated things in a simple manner, and by his mentoring skills and vision. I am very thankful to him for his valuable advice, assistance and support with the projects we worked on together. Markus Seeger's help on revision of my thesis was huge, to be more specific, he left me with more than 1000 comments, all which of course I had to correct. His attentions to details has helped me immensely in writing my thesis considering that I had to rewrite the entire sections sometimes. Also, he was always willing to share his knowledge on optics.

With Roman Shnaiderman and Ivan Olefir, my fellow comrades, we were always the ones who stayed the longest at IBMI festivities discussing matters of great importance, such as politics, healthcare and many others urgent topics. Chapin Rodriguez did not only help with countless pre-questionnaires and revisions of papers, but he was also an amazing person to talk to and to seek for advice. His cheerfulness even in the hardest situations could lift anybody's spirit.

Prof Ulf Darsow was in my thesis committee of HELENA graduate school providing me with his guidance and valuable medical advice on medical underlying of various diseases, which has helped me in the development a better suited imaging technique.

Also, our dear Admin Team has contributed tremendously to ease the struggles of a PhD studies, to navigate through the debris of bureaucracy and to establish healthy work environment. Therefore, I would like to sincerely thank Dr Andreas Hillmair, Susanne Stern, Dr Nike Tsalas, Dr Robert Wilson, Dr Roland Boha, Ines Baumgartner, Silvia Weinzierl, Julia Niefnecker, Dr Doris Bengel, and Dr Karl-Hans Englmeier. I would like to recognize the invaluable assistance provided by the technical personnel of IBMI Sarah Glasl, Uwe Klemm and Pia Anzenhofer. They are one of the most valuable and irreplaceable employees at the institute. I am also very grateful to all volunteers who participated in my studies, even though the experience was not very pleasant oftentimes. However, without them none of the results achieved in this work would be possible.

My special recognition goes to my family. They were always supportive and curious about my research. Despite me being far away from home and not having many opportunities to visit them, I missed them a lot.

A. List of publications

Publication in peer-reviewed journals

1. **A. Berezhnoi,** M. Schwarz, A. Buehler, S. V. Ovsepian, J. Aguirre, and V. Ntziachristos, "Assessing hyperthermia-induced vasodilation in human skin in vivo using optoacoustic mesoscopy," J. Biophotonics 11, (2018).
2. **A. Berezhnoi,** J. Aguirre, B. Hindelang, N. Garzorz-Stark, M. Omar, U. Darsow, K. Eyerich, and V. Ntziachristos, "Optical features of human skin revealed by optoacoustic mesoscopy in the visible and short-wave infrared regions," Opt. Lett. 44, 4119 (2019).
3. B. Hindelang, J. Aguirre, M. Schwarz, **A. Berezhnoi**, K. Eyerich, V. Ntziachristos, T. Biedermann, and U. Darsow, "Non-invasive imaging in dermatology and the unique potential of raster-scan optoacoustic mesoscopy," J. Eur. Acad. Dermatology Venereol. 33, 1051–1061 (2019).
4. J. Aguirre, **A. Berezhnoi**, H. He, M. Schwarz, B. Hindelang, M. Omar, and V. Ntziachristos, "Motion quantification and automated correction in clinical RSOM," IEEE Trans. Med. Imaging PP, 1–1 (2019).
5. E. Hadjipanayi, P. Moog, S. Bekeran, K. Kirchho, **A. Berezhnoi**, J. Aguirre, A. Bauer, H. Kükrek, D. Schmauss, U. Hopfner, S. Isenburg, V. Ntziachristos, M. Ninkovic, H. Machens, A. F. Schilling, and U. Dornseifer, "In Vitro Characterization of Hypoxia Preconditioned Serum (HPS)— Fibrin Hydrogels : Basis for an Injectable Biomimetic Tissue Regeneration Therapy," (2019).
6. K. Haedicke, L. Agemy, M. Omar, **A. Berezhnoi**, K. Nagar, H.-T. Hsu, K. Kim, J. Coleman, V. Ntziachristos, A. Scherz, and J. Grimm, "Listening to the therapy: High-resolution optoacoustic imaging allows real-time, non-invasive monitoring of the response to vascular-targeted therapy," Nat. Biomed. Eng. (2019).
7. J. Aguirre, B. Hindelang, **A. Bereznhoi**, U. Darsow, F. Lauffer, K. Eyerich, T. Biedermann, and V. Ntziachristos, "Assessing nailfold microvascular structure with ultra-wideband raster-scan optoacoustic mesoscopy," Photoacoustics 10, 31–37 (2018).
8. B. Hindelang, J. Aguirre, **A. Berezhnoi**, K. Eyerich, V. Ntziachristos, T. Biedermann, and U. Darsow, "Optoacoustic mesoscopy shows potential to increase accuracy of allergy patch testing," (2020), (the manuscript is in submission)

9. **A. Berezhnoi**, B. Hindelang, L. Riobo, C. Schönmann, H. He, J. Aguirre, and V. Ntziachristos, "Oxygenation changes in human skin assessed by dual-wavelength raster–scanning optoacoustic mesoscopy," (the manuscript is in preparation).

International conference contribution and proceedings

1. **Andrei Berezhnoi**, Mathias Schwarz, Andreas Buehler, Saak V. Ovsepian, Juan Aguirre, and Vasilis Ntziachristos, "Assessing hyperthermia-induced vasodilation in human skin in vivo using optoacoustic mesoscopy (Conference Presentation)", *Proc. SPIE 10494,* Photons Plus Ultrasound: Imaging and Sensing 2018, 1049408 (Presented at SPIE BiOS: January 28, 2018; Published: 15 March 2018); https://doi.org/10.1117/12.2288909.5752213094001.
2. Christine Schönmann, Juan Aguirre, He Hailong, **Andrei Berezhnoi**, Benedikt Hindelang, Vasilis Ntziachristos, Tilo Biedermann, Ulf Darsow, "Optoakustische Bildgebung bei Livedo-Vaskulopathie Fallbericht", (Poster presentation at DDG Kompakt & Praxisnah 2020)

B. Permission to reuse content from publications

Chapter 4 contains adapted text passages and figures from the publication by Berezhnoi et al. [176] © 2018 Wiley.

Chapter 5 and Section 3.4 contain adapted text passages and figures from the publication by Berezhnoi and Aguirre et al. [2] © 2018 OSA.

Section 6.2 contains adapted text passages and figures from the publication by Haedicke et al. [191] at Nature Biomedical Engineering.

Section 6.3 contains adapted text passages and figures from a manuscript to be submitted for publication by Berezhnoi et al. [192].

Written permission to reproduce text and illustrations have been granted for all the publications mentioned above. The permissions have been received in written electronic form and are available upon request

Bibliography

1. A. Berezhnoi, M. Schwarz, A. Buehler, S. V Ovsepian, J. Aguirre, and V. Ntziachristos, "Assessing hyperthermia-induced vasodilation in human skin in vivo using optoacoustic mesoscopy," J. Biophotonics **11**, (2018).
2. A. Berezhnoi, J. Aguirre, B. Hindelang, N. Garzorz-Stark, M. Omar, U. Darsow, K. Eyerich, and V. Ntziachristos, "Optical features of human skin revealed by optoacoustic mesoscopy in the visible and short-wave infrared regions," Opt. Lett. **44**, 4119 (2019).
3. R. J. Hay, N. E. Johns, H. C. Williams, I. W. Bolliger, R. P. Dellavalle, D. J. Margolis, R. Marks, L. Naldi, M. A. Weinstock, S. K. Wulf, C. Michaud, C. J.l. Murray, and M. Naghavi, "The global burden of skin disease in 2010: An analysis of the prevalence and impact of skin conditions," J. Invest. Dermatol. **134**, 1527–1534 (2014).
4. C. Karimkhani, R. P. Dellavalle, L. E. Coffeng, C. Flohr, R. J. Hay, S. M. Langan, E. O. Nsoesie, A. J. Ferrari, H. E. Erskine, J. I. Silverberg, T. Vos, and M. Naghavi, "Global skin disease morbidity and mortality an update from the global burden of disease study 2013," JAMA Dermatology **153**, 406–412 (2017).
5. J. E. Frangos, L. M. Duncan, A. Piris, R. M. Nazarian, M. C. Mihm, M. P. Hoang, B. Gleason, T. J. Flotte, H. R. Byers, R. L. Barnhill, and A. B. Kimball, "Increased diagnosis of thin superficial spreading melanomas: A 20-year study," J. Am. Acad. Dermatol. **67**, 387–394 (2012).
6. H. W. Lim, S. A. B. Collins, J. S. Resneck, J. L. Bolognia, J. A. Hodge, T. A. Rohrer, M. J. Van Beek, D. J. Margolis, A. J. Sober, M. A. Weinstock, D. R. Nerenz, W. Smith Begolka, and J. V. Moyano, "The burden of skin disease in the United States," J. Am. Acad. Dermatol. **76**, 958-972.e2 (2017).
7. D. C. Whiteman, A. C. Green, and C. M. Olsen, "The Growing Burden of Invasive Melanoma: Projections of Incidence Rates and Numbers of New Cases in Six Susceptible Populations through 2031," J. Invest. Dermatol. **136**, 1161–1171 (2016).
8. Z. Apalla, A. Lallas, E. Sotiriou, E. Lazaridou, and D. Ioannides, "Epidemiological trends in skin cancer," Dermatol. Pract. Concept. **7**, 1–6 (2017).
9. R. M. Bakos, T. P. Blumetti, R. Roldán-Marín, and G. Salerni, "Noninvasive Imaging Tools in the Diagnosis and Treatment of Skin Cancers," Am. J. Clin. Dermatol. **19**, 3–14 (2018).
10. A. Breslow, "Thickness, Cross-Sectional Areas and Depth of Invasion in the Prognosis of Cutaneous Melanoma," Ann. Surg. **172**, 902–908 (1970).

11. V. Bhandari, C. Hoey, L. Y. Liu, E. Lalonde, J. Ray, J. Livingstone, R. Lesurf, Y. J. Shiah, T. Vujcic, X. Huang, S. M. G. Espiritu, L. E. Heisler, F. Yousif, V. Huang, T. N. Yamaguchi, C. Q. Yao, V. Y. Sabelnykova, M. Fraser, M. L. K. Chua, T. van der Kwast, S. K. Liu, P. C. Boutros, and R. G. Bristow, "Molecular landmarks of tumor hypoxia across cancer types," Nat. Genet. **51**, 308–318 (2019).

12. R. Huber, B. Meier, A. Otsuka, G. Fenini, T. Satoh, S. Gehrke, D. Widmer, M. P. Levesque, J. Mangana, K. Kerl, C. Gebhardt, H. Fujii, C. Nakashima, Y. Nonomura, K. Kabashima, R. Dummer, E. Contassot, and L. E. French, "Tumour hypoxia promotes melanoma growth and metastasis via High Mobility Group Box-1 and M2-like macrophages," Sci. Rep. **6**, 1–14 (2016).

13. T. Golan, R. Parikh, E. Jacob, H. Vaknine, V. Zemser-Werner, D. Hershkovitz, H. Malcov, S. Leibou, H. Reichman, D. Sheinboim, R. Percik, S. Amar, R. Brenner, S. Greenberger, A. Kung, M. Khaled, and C. Levy, "Adipocytes sensitize melanoma cells to environmental TGF-β cues by repressing the expression of miR-211," Sci. Signal. **12**, 6847 (2019).

14. S. Batz, C. Wahrlich, A. Alawi, M. Ulrich, and J. Lademann, "Differentiation of Different Nonmelanoma Skin Cancer Types Using OCT," Skin Pharmacol. Physiol. **31**, 238–245 (2018).

15. "Common Inflammatory Skin Disorders," https://www.lifeextension.com/protocols/skin-nails-hair/skin-disorders/page-07.

16. K. Eyerich and N. Novak, "Immunology of atopic eczema: Overcoming the Th1/Th2 paradigm," Allergy Eur. J. Allergy Clin. Immunol. **68**, 974–982 (2013).

17. R. Heidenreich, M. Röcken, and K. Ghoreschi, "Angiogenesis drives psoriasis pathogenesis," Int. J. Exp. Pathol. **90**, 232–248 (2009).

18. S. Eyerich, A. T. Onken, S. Weidinger, A. Franke, F. Nasorri, D. Pennino, M. Grosber, F. Pfab, C. B. Schmidt-Weber, M. Mempel, R. Hein, J. Ring, A. Cavani, and K. Eyerich, "Mutual antagonism of T cells causing psoriasis and atopic eczema," N. Engl. J. Med. **365**, 231–238 (2011).

19. J. Aguirre, M. Schwarz, N. Garzorz, M. Omar, A. Buehler, K. Eyerich, and V. Ntziachristos, "Precision assessment of label-free psoriasis biomarkers with ultra-broadband optoacoustic mesoscopy," Nat. Biomed. Eng. **1**, 1–8 (2017).

20. J.-M. Anaya, Y. Shoenfeld, A. R.-V. R. A. Levy, and R. Cervera, *Autoimmunity: From Bench to Bedside* (2013).

21. A. Berekméri, A. Tiganescu, A. A. Alase, E. Vital, M. Stacey, and M. Wittmann, "Non-

invasive Approaches for the Diagnosis of Autoimmune/Autoinflammatory Skin Diseases—A Focus on Psoriasis and Lupus erythematosus," Front. Immunol. **10**, 1–12 (2019).

22. F. Fichel, N. Baudot, J. P. Gaitz, S. Trad, C. Barbe, C. Francès, and P. Senet, "Systemic sclerosis with normal or nonspecific nailfold capillaroscopy," Dermatology **228**, 360–367 (2014).
23. C. T. Minson, "Thermal provocation to evaluate microvascular reactivity in human skin," J. Appl. Physiol. **109**, 1239–1246 (2010).
24. R. Joannides, J. Bellien, and C. Thuillez, "Clinical methods for the evaluation of endothelial function-- a focus on resistance arteries.," Fundam. Clin. Pharmacol. **20**, 311–320 (2006).
25. L. A. Holowatz, C. S. Thompson-torgerson, and W. L. Kenney, "The human cutaneous circulation as a model of generalized microvascular function," J. Appl. Physiol. **105**, 370–372 (2008).
26. A. L. Lima, T. Illing, S. Schliemann, and P. Elsner, "Cutaneous Manifestations of Diabetes Mellitus: A Review," Am. J. Clin. Dermatol. **18**, 541–553 (2017).
27. I. Fredriksson, M. Larsson, F. H. Nyström, T. Länne, C. J. Östgren, and T. Strömberg, "Reduced arteriovenous shunting capacity after local heating and redistribution of baseline skin blood flow in type 2 diabetes assessed with velocity-resolved quantitative laser Doppler flowmetry," Diabetes **59**, 1578–1584 (2010).
28. C. Freccero, H. Svensson, S. Bornmyr, P. Wollmer, and G. Sundkvist, "Sympathetic and parasympathetic neuropathy are frequent in both type 1 and type 2 diabetic patients," Diabetes Care **27**, 2936–2941 (2004).
29. J. C. Patik, K. M. Christmas, C. Hurr, and R. M. Brothers, "Impaired endothelium independent vasodilation in the cutaneous microvasculature of young obese adults," Microvasc. Res. **104**, 63–68 (2016).
30. J. Cui, A. Arbab-Zadeh, A. Prasad, S. Durand, B. D. Levine, and C. G. Crandall, "Effects of heat stress on thermoregulatory responses in congestive heart failure patients," Circulation **112**, 2286–2292 (2005).
31. D. J. Green, A. J. Maiorana, J. H. J. Siong, V. Burke, M. Erickson, C. T. Minson, W. Bilsborough, and G. O’Driscoll, "Impaired skin blood flow response to environmental heating in chronic heart failure," Eur. Heart J. **27**, 338–343 (2006).
32. L. Jayakody, T. Kappagoda, M. P. J. Senaratne, and A. B. R. Thomson, "Impairment of endothelium- dependent relaxation: an early marker for atherosclerosis in the rabbit," Br.

J. Pharmacol. **94**, 335–346 (1988).

33. L. G. Kraemer-Aguiar, C. M. Laflor, and E. Bouskela, "Skin microcirculatory dysfunction is already present in normoglycemic subjects with metabolic syndrome," Metabolism. **57**, 1740–1746 (2008).
34. J. M. Johnson, C. T. Minson, and D. L. Kellogg, "Cutaneous vasodilator and vasoconstrictor mechanisms in temperature regulation," Compr. Physiol. **4**, 33–89 (2014).
35. D. L. Kellogg, "In vivo mechanisms of cutaneous vasodilation and vasoconstriction in humans during thermoregulatory challenges.," J. Appl. Physiol. **100**, 1709–1718 (2006).
36. R. B. D’Agostino, R. S. Vasan, M. J. Pencina, P. A. Wolf, M. Cobain, J. M. Massaro, and W. B. Kannel, "General cardiovascular risk profile for use in primary care: The Framingham heart study," Circulation **117**, 743–753 (2008).
37. K. H. Liu, Y. L. Chan, W. B. Chan, W. L. Kong, M. O. Kong, and J. C. N. Chan, "Sonographic measurement of mesenteric fat thickness is a good correlate with cardiovascular risk factors: Comparison with subcutaneous and preperitoneal fat thickness, magnetic resonance imaging and anthropometric indexes," Int. J. Obes. **27**, 1267–1273 (2003).
38. D. P. Andersson, D. E. Hogling, A. Thorell, E. Toft, V. Qvisth, E. Näslund, A. Thörne, M. Wirén, P. Löfgren, J. Hoffstedt, I. Dahlman, N. Mejhert, M. Rydén, E. Arner, and P. Arner, "Changes in subcutaneous fat cell volume and insulin sensitivity after weight loss," Diabetes Care **37**, 1831–1836 (2014).
39. C. C. Zouboulis, S. Schagen, and T. Alestas, "The sebocyte culture: A model to study the pathophysiology of the sebaceous gland in sebostasis, seborrhoea and acne," Arch. Dermatol. Res. **300**, 397–413 (2008).
40. M. I. Perez and S. R. Kohn, "Cutaneous manifestations of diabetes mellitus," J. Am. Acad. Dermatol. **30**, 519–531 (1994).
41. J. J. Miranda, A. Taype-Rondan, J. C. Tapia, M. G. Gastanadui-Gonzalez, and R. Roman-Carpio, "Hair follicle characteristics as early marker of type 2 diabetes," Med Hypotheses **95**, 39–44 (2016).
42. J. D. McBride, A. J. Jenkins, X. Liu, B. Zhang, K. Lee, W. L. Berry, R. Janknecht, C. T. Griffin, C. E. Aston, T. J. Lyons, J. J. Tomasek, and J. X. Ma, "Elevated circulation levels of an antiangiogenic serpin in patients with diabetic microvascular complications impair wound healing through suppression of Wnt signaling," J. Invest. Dermatol. **134**, 1725–1734 (2014).

43. M. S. Nguyen-Tu, P. Nivoit, V. Oréa, S. Lemoine, C. Acquaviva, A. Pagnon-Minot, B. Fromy, J. K. Sethi, and D. Sigaudo-Roussel, "Inflammation-linked adaptations in dermal microvascular reactivity accompany the development of obesity and type 2 diabetes," Int. J. Obes. **43**, 556–566 (2018).

44. M. R. Prausnitz and R. Langer, "Transdermal drug delivery," Nat. Biotechnol. **26**, 1261–1268 (2008).

45. M. Rajadhyaksha, A. Marghoob, A. Rossi, A. C. Halpern, and K. S. Nehal, "Reflectance confocal microscopy of skin in vivo: From bench to bedside," Lasers Surg. Med. **49**, 7–19 (2017).

46. P. Calzavara-Pinton, C. Longo, M. Venturin, R. Sala, and G. Pellacani, "Reflectance confocal microscopy for in vivo skin imaging," Photochem. Photobiol. **84**, 1421–1430 (2008).

47. C. P and L. JL., "In vivo vision of the human skin with the tandem scanning microscope," Dermatology **186**, 50–54 (1993).

48. S. González and Y. Gilaberte-Calzada, "In vivo reflectance-mode confocal microscopy in clinical dermatology and cosmetology," Int. J. Cosmet. Sci. **30**, 1–17 (2008).

49. R. Archid, "Confocal laser-scanning microscopy of capillaries in normal and psoriatic skin," J. Biomed. Opt. **17**, 101511 (2012).

50. S. Nori, F. Rius-Díaz, J. Cuevas, M. Goldgeier, P. Jaen, A. Torres, and S. González, "Sensitivity and specificity of reflectance-mode confocal microscopy for in vivo diagnosis of basal cell carcinoma: A multicenter study," J. Am. Acad. Dermatol. **51**, 923–930 (2004).

51. E. Yew, C. Rowlands, and P. T. C. So, "Application of multiphoton microscopy in dermatological studies: A mini-review," J. Innov. Opt. Health Sci. **07**, 1330010 (2014).

52. E. Dimitrow, M. Ziemer, M. J. Koehler, J. Norgauer, K. Ko, P. Elsner, and M. Kaatz, "Sensitivity and Specificity of Multiphoton Laser Tomography for In Vivo and Ex Vivo Diagnosis of Malignant Melanoma," **129**, 1752–1758 (2009).

53. P. D. Maker and R. W. Terhune, "Study of Optical Effects Due to an Induced Polarization Third Order in the Electric Field Strength," Phys. Rev. **137**, (1965).

54. Y. Ozeki, W. Umemura, Y. Otsuka, S. Satoh, H. Hashimoto, K. Sumimura, N. Nishizawa, K. Fukui, and K. Itoh, "High-speed molecular spectral imaging of tissue with stimulated Raman scattering," Nat. Photonics **6**, 845–851 (2012).

55. C. P. Lin, X. S. Xie, C. L. Evans, E. O. Potma, M. Puoris, and D. Co, "Chemical imaging of tissue in vivo with video-rate coherent anti-Stokes Raman scattering microscopy,"

Proc. Natl. Acad. Sci. **102**, 16807–16812 (2005).

56. R. Bonner and R. Nossal, "Model for laser Doppler measurements of blood flow in tissue," Appl. Opt. **20**, 2097–2107 (1981).

57. C. Song, L. Chelstrom, D. Aumschild, D. Haumschild, and D. Aumschild, "Changes in human skin blood flow by hyperthermia," Int. J. Radiat. Oncol. Biol. Phys. **18**, 903–907 (1990).

58. D. J. H. Chang W. Song, Lisa M. Chelstrom, Seymour H. Levitt, "Effects of temperature on blood circulation measured with the laser doppler method," Int. J. Radiat. Oncol. **17**, 1041–1047 (1989).

59. V. Rajan, B. Varghese, T. G. Van Leeuwen, and W. Steenbergen, "Review of methodological developments in laser Doppler flowmetry," Lasers Med. Sci. **24**, 269–283 (2009).

60. H. N. Mayrovitz and J. A. Leedham, "Laser-Doppler imaging of forearm skin: perfusion features and dependence of the biological zero on heat-induced hyperemia.," Microvasc. Res. **62**, 74–8 (2001).

61. M. Roustit, C. Millet, S. Blaise, B. Dufournet, and J. L. Cracowski, "Excellent reproducibility of laser speckle contrast imaging to assess skin microvascular reactivity," Microvasc. Res. **80**, 505–511 (2010).

62. T. Binzoni, a Humeau-Heurtier, P. Abraham, and G. Mahe, "Blood Perfusion Values of Laser Speckle Contrast Imaging and Laser Doppler Flowmetry: Is a Direct Comparison Possible?," Biomed. Eng. IEEE Trans. **60**, 1259–1265 (2013).

63. D. Huang, E. a Swanson, C. P. Lin, J. S. Schuman, W. G. Stinson, W. Chang, M. R. Hee, T. Flotire, K. Gregory, C. a Puliafito, and J. G. Fujimoto, "Optical Coherence Tomography," Science (80-.). **254**, 1178–1181 (1991).

64. B. Zabihian, J. Weingast, M. Liu, E. Zhang, P. Beard, H. Pehamberger, W. Drexler, and B. Hermann, "In vivo dual-modality photoacoustic and optical coherence tomography imaging of human dermatological pathologies," Biomed. Opt. Express **6**, 3163 (2015).

65. E. Sattler, R. Kästle, and J. Welzel, "Optical coherence tomography in dermatology," J. Biomed. Opt. **18**, 061224 (2013).

66. J. Qin, J. Jiang, L. An, D. Gareau, and R. K. Wang, "In vivo volumetric imaging of microcirculation within human skin under psoriatic conditions using optical microangiography," Lasers Surg. Med. **43**, 122–129 (2011).

67. C. Errico, J. Pierre, S. Pezet, Y. Desailly, Z. Lenkei, O. Couture, and M. Tanter, "Ultrafast ultrasound localization microscopy for deep super-resolution vascular

imaging," Nature **527**, 499–502 (2015).

68. D. Jasaitiene, S. Valiukeviciene, G. Linkeviciute, R. Raisutis, E. Jasiuniene, and R. Kazys, "Principles of high-frequency ultrasonography for investigation of skin pathology," J. Eur. Acad. Dermatology Venereol. **25**, 375–382 (2011).
69. M. Gutierrez, X. Wortsman, E. Filippucci, R. De Angelis, G. Filosa, and W. Grassi, "High-frequency sonography in the evaluation of nail psoriasis," Med. Ultrason. **18**, 312–317 (2016).
70. M. Gutierrez, X. Wortsman, E. Filippucci, R. De Angelis, G. Filosa, and W. Grassi, "High-Frequency Sonography in the Evaluation of Psoriasis," (n.d.).
71. W. Müller, T. G. Lohman, A. D. Stewart, R. J. Maughan, N. L. Meyer, L. B. Sardinha, N. Kirihennedige, A. Reguant-Closa, V. Risoul-Salas, J. Sundgot-Borgen, H. Ahammer, F. Anderhuber, A. Fürhapter-Rieger, P. Kainz, W. Materna, U. Pilsl, W. Pirstinger, and T. R. Ackland, "Subcutaneous fat patterning in athletes: Selection of appropriate sites and standardisation of a novel ultrasound measurement technique: Ad hoc working group on body composition, health and performance, under the auspices of the IOC Medical Commission," Br. J. Sports Med. **50**, 45–54 (2016).
72. A. A. Oraevsky, R. O. Esenaliev, S. L. Jacques, and F. K. Tittel, "Laser optoacoustic tomography for medical diagnostics: principles," Proc. Vol. 2676, Biomed. Sensing, Imaging, Track. Technol. I; (1996).
73. M. Omar, J. Aguirre, and V. Ntziachristos, "Optoacoustic mesoscopy for biomedicine," Nat. Biomed. Eng. **3**, 354–370 (2019).
74. A. N. Bashkatov, E. A. Genina, and V. V. Tuchin, "Optical properties of skin, subcutaneous, and muscle tissues: A review," J. Innov. Opt. Health Sci. **4**, 9–38 (2011).
75. V. Ntziachristos and D. Razansky, "Molecular Imaging by Means of Multispectral Optoacoustic Tomography (MSOT)," Chem. Rev. **110**, 2783–2794 (2010).
76. L. V. Wang and S. Hu, "Photoacoustic Tomography: In Vivo Imaging from Organelles to Organs," Science (80-.). **335**, 1458–1462 (2012).
77. A. Rosenthal, D. Razansky, and V. Ntziachristos, "Quantitative optoacoustic signal extraction using sparse signal representation," IEEE Trans. Med. Imaging **28**, 1997–2006 (2009).
78. M. Omar and M. Schwarz, "Pushing the Optical Imaging Limits of Cancer with Multi-Frequency-Band Raster-Scan Optoacoustic Mesoscopy (RSOM) Band Raster-Scan Optoacoustic," (2016).
79. D. M. M and P. L. Choyke, "Imaging of angiogenesis: From microscope to clinic," Nat.

Med. **9**, 713–725 (2003).

80. S. L. Jacques, "Optical properties of biological tissues: a review," Phys. Med. Biol. **58**, 5007–5008 (2013).
81. A. Plumb, N. T. Huynh, J. A. Guggenheim, E. Zhang, and P. C. Beard, "Rapid volumetric photoacoustic tomographic imaging with a Fabry-Pérot ultrasound sensor depicts peripheral arteries and microvascular vasomotor responses to thermal stimuli.," Eur. J. Radiol. “Accepted”. (2017).
82. E. Z. Zhang, J. G. Laufer, R. B. Pedley, and P. C. Beard, "In vivo high-resolution 3D photoacoustic imaging of superficial vascular anatomy," Phys. Med. Biol. 1035–1046 (2009).
83. G. Wissmeyer, M. A. Pleitez, A. Rosenthal, and V. Ntziachristos, "Looking at sound: optoacoustics with all-optical ultrasound detection," Light Sci. Appl. **7**, (2018).
84. L. Vionnet, J. Gateau, M. Schwarz, A. Buehler, V. Ermolayev, and V. Ntziachristos, "24-MHz Scanner for Optoacoustic Imaging of Skin and Burn," IEEE Trans. Med. Imaging **33**, 535–545 (2014).
85. A. A. Karabutov, E. V Savateeva, and A. A. Oraevsky, "Imaging of layered structures in biological tissues with opto-acoustic front surface transducer," **3601**, 284–295 (1999).
86. H. F. Zhang, K. Maslov, M. Li, and L. V Wang, "In vivo volumetric imaging of subcutaneous microvasculature by photoacoustic microscopy," Opt. Express **14**, 1739–1741 (2006).
87. C. P. Favazza, O. Jassim, L. A. Cornelius, and L. V Wang, "In vivo photoacoustic microscopy of human cutaneous microvasculature and a nevus," J. Biomed. Opt. **16**, (2011).
88. C. P. Favazza, L. A. Cornelius, and L. V Wang, "In vivo functional photoacoustic microscopy of cutaneous microvasculature in human skin," J. Biomed. Opt. **16**, (2011).
89. S. J. Ford, P. L. Bigliardi, T. C. P. Sardella, A. Urich, N. C. Burton, M. Kacprowicz, M. Bigliardi, M. Olivo, and D. Razansky, "Structural and Functional Analysis of Intact Hair Follicles and Pilosebaceous Units by Volumetric Multispectral Optoacoustic Tomography," J. Invest. Dermatol. **136**, 753–761 (2016).
90. E. Liapis, E. Rummeny, R. Meier, S. Metz, G. Diot, S. V. Ovsepian, V. Ntziachristos, A. Noske, and B. Schroeder, "Multispectral Optoacoustic Tomography (MSOT) of Human Breast Cancer," Clin. Cancer Res. **23**, 6912–6922 (2017).
91. M. Omar, D. Soliman, J. Gateau, and V. Ntziachristos, "Ultrawideband reflection-mode optoacoustic mesoscopy.," Opt. Lett. **39**, 3911–4 (2014).

92. J. Aguirre, M. Schwarz, N. Garzorz, M. Omar, A. Buehler, K. Eyerich, and V. Ntziachristos, "Precision assessment of label-free psoriasis biomarkers with ultra-broadband optoacoustic mesoscopy," Nat. Biomed. Eng. **1**, 1–8 (2017).

93. M. Schwarz, N. Garzorz-Stark, K. Eyerich, J. Aguirre, and V. Ntziachristos, "Motion correction in optoacoustic mesoscopy," Sci. Rep. **7**, 1–9 (2017).

94. J. Aguirre, A. Berezhnoi, H. He, M. Schwarz, B. Hindelang, M. Omar, and V. Ntziachristos, "Motion quantification and automated correction in clinical RSOM," IEEE Trans. Med. Imaging **PP**, 1–1 (2019).

95. J. Aguirre, B. Hindelang, A. Bereznhoi, U. Darsow, F. Lauffer, K. Eyerich, T. Biedermann, and V. Ntziachristos, "Assessing nailfold microvascular structure with ultra-wideband raster-scan optoacoustic mesoscopy," Photoacoustics **10**, 31–37 (2018).

96. M. Schwarz, A. Buehler, J. Aguirre, and V. Ntziachristos, "Three-dimensional multispectral optoacoustic mesoscopy reveals melanin and blood oxygenation in human skin in vivo," J. Biophotonics **9**, 55–60 (2016).

97. M. R. Hamblin, P. Avci, and G. K. Gupta, *Imaging in Dermatology* (2016).

98. H. Kittler, H. Pehamberger, K. Wolff, and M. Binder, "Diagnostic accuracy of dermoscopy," Lancet Oncol. **3**, 159–165 (2002).

99. M. Rajadhyaksha, S. González, J. M. Zavislan, R. R. Anderson, and R. H. Webb, "In vivo confocal scanning laser microscopy of human skin II: Advances in instrumentation and comparison with histology," J. Invest. Dermatol. **113**, 293–303 (1999).

100. M. Balu, H. Mikami, J. Hou, E. O. Potma, and B. J. Tromberg, "Rapid mesoscale multiphoton microscopy of human skin," Biomed. Opt. Express **7**, 4375 (2016).

101. B. G. Saar, L. R. Contreras-Rojas, X. S. Xie, and and R. H. Guy, "Imaging Drug Delivery to Skin with Stimulated Raman Scattering Microscopy," Mol. Pharm. **8**, 969–975 (2011).

102. M. Leutenegger, P. Harbi, T. Thacher, W. Raffoul, and T. Lasser, "Real-time full field laser Doppler imaging," AIP Conf. Proc. **1457**, 282–286 (2012).

103. P. G. Vaz, A. Humeau-Heurtier, E. Figueiras, C. Correia, and J. Cardoso, "Laser Speckle Imaging to Monitor Microvascular Blood Flow: A Review," IEEE Rev. Biomed. Eng. **9**, 106–120 (2016).

104. A. Dubois, O. Levecq, H. Azimani, D. Siret, A. Barut, M. Suppa, V. del Marmol, J. Malvehy, E. Cinotti, P. Rubegni, and J.-L. Perrot, "Line-field confocal optical coherence tomography for high-resolution noninvasive imaging of skin tumors," J. Biomed. Opt. **23**, 1 (2018).

105. M. Schwarz, "Multispectral Optoacoustic Dermoscopy : Methods and Applications," (2017).

106. D. Breitkreutz, I. Koxholt, K. Thiemann, and R. Nischt, "Skin basement membrane: The foundation of epidermal integrity - BM functions and diverse roles of bridging molecules nidogen and perlecan," Biomed Res. Int. **2013**, (2013).

107. J. E. Lai-Cheong and J. A. McGrath, "Structure and function of skin, hair and nails," Med. (United Kingdom) **45**, 347–351 (2017).

108. A. R. Young, "Chromophores in human skin," Phys. Med. Biol. **42**, 789–802 (1997).

109. J. A. McGrath, R. A. J. Eady, and F. M. Pope, "Components of normal human skin," (n.d.).

110. I. M. Braverman, "The cutaneous microcirculation: ultrastructure and microanatomical organization," Microcirculation **4**, 329–340 (1997).

111. O. Akkus, "Evaluation of Skin and Subcutaneous Adipose Tissue Thickness for Optimal Insulin Injection," J. Diabetes Metab. **03**, (2012).

112. M. Picardo and et al, "Sebaceous gland lipids . Dermato Endocronology," **1**, 68–71 (2009).

113. K. Kabashima, T. Honda, F. Ginhoux, and G. Egawa, "The immunological anatomy of the skin," Nat. Rev. Immunol. **19**, 19–30 (2019).

114. K. Kretzschmar and F. M. Watt, "Markers of epidermal stem cell subpopulations in adult mammalian skin," Cold Spring Harb. Perspect. Med. **4**, (2014).

115. W. C. Lobitz, "The Structure and Function of the Sebaceous Glands," A. M. A. Arch. Dermatology **76**, 162–171 (1957).

116. B. D. Hodge and R. T. Brodell, *Anatomy, Skin Sweat Glands* (StatPearls Publishing, 2019).

117. K. J. Busam, *Dermatopathology, Foundations in Diagnostic Pathology Series*, 1st ed. (Elsevier Inc., 2010).

118. A. Slominski, J. Wortsman, P. M. Plonka, K. U. Schallreuter, R. Paus, and D. J. Tobin, "Hair follicle pigmentation," J. Invest. Dermatol. **124**, 13–21 (2005).

119. K. A. WALTERS and G. L. FLYNN, "Permeability characteristics of the human nail plate," Int. J. Cosmet. Sci. **5**, 231–246 (1983).

120. J. Uitto, "Connective tissue biochemistry of the aging dermis. Age-related alterations in collagen and elastin.," Dermatol. Clin. **4**, 433–46 (1986).

121. D. J. Tobin, "Biochemistry of human skin - Our brain on the outside," Chem. Soc. Rev. **35**, 52–67 (2006).

122. K. R. Feingold, M. Schmuth, and P. M. Elias, "The regulation of permeability barrier homeostasis," J. Invest. Dermatol. **127**, 1574–1576 (2007).

123. G. K. Menon and A. M. Kligman, "Barrier functions of human skin: A holistic view," Skin Pharmacol. Physiol. **22**, 178–189 (2009).

124. T. B. Fitzpatrick, "The Validity and Practicality of," Arch. Dermatol. **124**, 869–871 (1988).

125. I. Goldstein, V. Marcel, M. Olivier, M. Oren, V. Rotter, and P. Hainaut, "Understanding wild-type and mutant p53 activities in human cancer: New landmarks on the way to targeted therapies," Cancer Gene Ther. **18**, 2–11 (2011).

126. E. Proksch, J. Brasch, and W. Sterry, "Integrity of the permeability barrier regulates epidermal Langerhans cell density," Br. J. Dermatol. **134**, 630–638 (1996).

127. O. E. Sørensen, D. R. Thapa, K. M. Roupé, E. V. Valore, U. Sjöbring, A. A. Roberts, A. Schmidtchen, and T. Ganz, "Injury-induced innate immune response in human skin mediated by transactivation of the epidermal growth factor receptor," J. Clin. Invest. **116**, 1878–1885 (2006).

128. R. C. Yu, D. C. Abrams, M. Alaibac, and A. C. Chu, "Morphological and quantitative analyses of normal epidermal Langerhans cells using confocal scanning laser microscopy," Br. J. Dermatol. **131**, 843–848 (1994).

129. L. De Witte, A. Nabatov, M. Pion, D. Fluitsma, M. A. W. P. De Jong, T. De Gruijl, V. Piguet, Y. Van Kooyk, and T. B. H. Geijtenbeek, "Langerin is a natural barrier to HIV-1 transmission by Langerhans cells," Nat. Med. **13**, 367–371 (2007).

130. N. G. Jablonski and G. Chaplin, "The evolution of human skin coloration," J. Hum. Evol. **39**, 57–106 (2000).

131. H. A. M. Daanen, "Finger cold-induced vasodilation: A review," Eur. J. Appl. Physiol. **89**, 411–426 (2003).

132. "Functions of the Integumentary System | Boundless Anatomy and Physiology," https://courses.lumenlearning.com/boundless-ap/chapter/functions-of-the-integumentary-system/.

133. T. Lister, P. a Wright, and P. H. Chappell, "Optical properties of human skin," J. Biomed. Opt. **17**, 90901 (2012).

134. I. M. Braverman and A. Keh-Yen, "Ultrastructure of the human dermal microcirculation. III. The vessels in the mid- and lower dermis and subcutaneous fat," J. Invest. Dermatol. **77**, 297–304 (1981).

135. S.-H. Tseng1, P. Bargo, A. Durkin, and N. Kollias, "Chromophore concentrations,

absorption and scattering properties of human skin in-vivo," Opt. Quantum Electron. **17**, 14599–14617 (2009).

136. S. Alaluf, D. Atkins, K. Barrett, M. Blount, N. Carter, and A. Heath, "Ethnic variation in melanin content and composition in photoexposed and photoprotected human skin," Pigment Cell Res. **15**, 112–118 (2002).

137. G. Hunt, S. Kyne, S. Ito, K. Wakamatsu, C. Todd, and A. J. Thody, "Eumelanin and Phaeomelanin Contents of Human Epidermis and Cultured Melanocytes," Pigment Cell Res. **8**, 202–208 (1995).

138. A. N. Bashkatov, E. A. Genina, V. I. Kochubei, and V. V Tuchin, "Estimate of the melanin content in human hairs by the inverse Monte-Carlo method using a system for digital image analysis," Quantum Electron. **36**, 1111–1118 (2006).

139. L. W. Thomas, "the Chemical Composition of Adipose Tissue of Man and Mice," Q. J. Exp. Physiol. Cogn. Med. Sci. **47**, 179–188 (1962).

140. R. P. REINERTSON and V. R. WHEATLEY, "Studies on the chemical composition of human epidermal lipids.," J. Invest. Dermatol. **32**, 49–59 (1959).

141. R. H. Wilson, K. P. Nadeau, F. B. Jaworski, B. J. Tromberg, and A. J. Durkin, "Review of short-wave infrared spectroscopy and imaging methods for biological tissue characterization," J. Biomed. Opt. **20**, 030901 (2015).

142. R. Nachabé, B. H. W. Hendriks, A. E. Desjardins, M. van der Voort, M. B. van der Mark, and H. J. C. M. Sterenborg, "Estimation of lipid and water concentrations in scattering media with diffuse optical spectroscopy from 900 to 1600 nm," J. Biomed. Opt. **15**, 037015 (2010).

143. R. Nachabé, D. J. Evers, B. H. W. Hendriks, G. W. Lucassen, M. van der Voort, E. J. Rutgers, M.-J. V. Peeters, J. A. Van der Hage, H. S. Oldenburg, J. Wesseling, and T. J. M. Ruers, "Diagnosis of breast cancer using diffuse optical spectroscopy from 500 to 1600 nm: comparison of classification methods," J. Biomed. Opt. **16**, 087010 (2011).

144. M. C. Branchet, S. Boisnic, C. Frances, C. Lesty, and L. Robert, "Morphometric analysis of dermal collagen fibers in normal human skin as a function of age," Arch. Gerontol. Geriatr. **13**, 1–14 (1991).

145. P. Rompre, F. A. Auger, L. Germain, V. Bouvard, C. A. Lopez Valle, J. Thibault, and A. Le Duy, "Influence of initial collagen and cellular concentrations on the final surface area of dermal and skin equivalents: A Box-Behnken analysis," Vitr. Cell. Dev. Biol. - Anim. **26**, 983–990 (1990).

146. N. Nakagawa, M. Matsumoto, and S. Sakai, "In vivo measurement of the water content

in the dermis by confocal Raman spectroscopy," Ski. Res. Technol. **16**, 137–141 (2010).

147. L. W. Thomas, "The Chemical Composition of Adipose Tissue of Man and Mice," Q. J. Exp. Physiol. Cogn. Med. Sci. **47**, 179–188 (1962).
148. E. Salomatina, B. Jiang, J. Novak, and A. N. Yaroslavsky, "Optical properties of normal and cancerous human skin in the visible and near-infrared spectral range," J. Biomed. Opt. **11**, 064026 (2006).
149. T. L. Troy and S. N. Thennadil, "Optical properties of human skin in the near infrared wavelength range of 1000 to 2200 nm," J. Biomed. Opt. **6**, 167 (2001).
150. H. Ding, J. Q. Lu, W. A. Wooden, P. J. Kragel, and X. H. Hu, "Refractive indices of human skin tissues at eight wavelengths and estimated dispersion relations between 300 and 1600 nm," Phys. Med. Biol. **51**, 1479–1489 (2006).
151. M. J. C. Van Gemert, S. L. Jacques, H. J. C. M. Sterenborg, and W. M. Star, "Skin Optics," IEEE Trans. Biomed. Eng. **36**, 1146–1154 (1989).
152. B. Cox, J. G. Laufer, S. R. Arridge, and P. C. Beard, "Quantitative spectroscopic photoacoustic imaging: a review.," J. Biomed. Opt. **17**, 061202 (2012).
153. M. A. Omar, "Multi-scale thermoacoustic imaging methods of biological tissues," (2015).
154. L. V. Wang, "Tutorial on photoacoustic microscopy and computed tomography," IEEE J. Sel. Top. Quantum Electron. **14**, 171–179 (2008).
155. F. Xu, T. J. Lu, and K. A. Seffen, "Biothermomechanical behavior of skin tissue," Acta Mech. Sin. Xuebao **24**, 1–23 (2008).
156. M. Xu and L. V. Wang, "Photoacoustic imaging in biomedicine," Rev. Sci. Instrum. **77**, 1–22 (2006).
157. Y. S. Touloukian and C. Y. Ho, "Thermophysical Properties of Matter: Thermal Conductivity of Nonmetallic Liquids and Gases," (1990).
158. L. F. Brown and S. Member, "Design Considerations for Piezoelectric Polymer Ultrasound Transducers," **47**, (2000).
159. E. Zhang, J. Laufer, and P. Beard, "Backward-mode multiwavelength photoacoustic scanner using a planar Fabry – Perot polymer film ultrasound sensor for high-resolution three-dimensional imaging of biological tissues," **47**, (2008).
160. J. Laufer, D. Delpy, C. Elwell, and P. Beard, "Quantitative spatially resolved measurement of tissue chromophore concentrations using photoacoustic spectroscopy : application to the measurement of blood oxygenation and haemoglobin concentration," Phys. Med. Biol. **52**, (2006).

161. A. Rosenthal, V. Ntziachristos, and D. Razansky, "Acoustic Inversion in Optoacoustic Tomography: A Review," Curr. Med. Imaging Rev. **9**, 318–336 (2014).
162. B. E. Treeby, "Acoustic attenuation compensation in photoacoustic tomography using time-variant filtering," J. Biomed. Opt. **18**, 036008 (2013).
163. Y. Hristova, P. Kuchment, and L. Nguyen, "Reconstruction and time reversal in thermoacoustic tomography in acoustically homogeneous and inhomogeneous media," Inverse Probl. **24**, (2008).
164. A. Dima, N. C. Burton, and V. Ntziachristos, "Multispectral optoacoustic tomography at 64, 128, and 256 channels.," J. Biomed. Opt. **19**, 36021 (2014).
165. Y. Hristova, P. Kuchment, and L. Nguyen, "Reconstruction and time reversal in thermoacoustic tomography in acoustically homogeneous and inhomogeneous media," **055006**, (2008).
166. P. J. La Rivière, J. Zhang, and M. A. Anastasio, "Image reconstruction in optoacoustic tomography for dispersive acoustic media," Opt. Lett. **31**, 781–783 (2006).
167. M. Xu and L. V. Wang, "Universal back-projection algorithm for photoacoustic computed tomography," Phys. Rev. E - Stat. Nonlinear, Soft Matter Phys. **71**, 1–7 (2005).
168. B. T. Cox, J. G. Laufer, and P. C. Beard, "The challenges for quantitative photoacoustic imaging," Photons Plus Ultrasound Imaging Sens. 2009 **7177**, 717713 (2009).
169. S. Tzoumas, A. Nunes, I. Olefir, S. Stangl, P. Symvoulidis, S. Glasl, C. Bayer, G. Multhoff, and V. Ntziachristos, "Eigenspectra optoacoustic tomography achieves quantitative blood oxygenation imaging deep in tissues," Nat. Commun. **7**, 12121 (2016).
170. M. Schwarz, D. Soliman, M. Omar, A. Buehler, S. Ovsepyan, J. Aguirre, and V. Ntziachristos, "Optoacoustic Dermoscopy of the Human Skin: Tuning Excitation Energy for Optimal Detection Bandwidth with Fast and Deep Imaging in vivo," IEEE Trans. Med. Imaging **0062**, 1–1 (2017).
171. J. Xia, J. Yao, and L. H. V. Wang, "Photoacoustic tomography: principles and advances," Prog. Electromagn. Res. **147**, 1–22 (2015).
172. M. L. Li, W. J. Guan, and P. C. Li, "Improved Synthetic Aperture Focusing Technique with Applications in High-Frequency Ultrasound Imaging," IEEE Trans. Ultrason. Ferroelectr. Freq. Control **51**, 63–70 (2004).
173. NDT Olympus, "Ultrasonic transducers technical notes," Tech. Broch. Olympus NDT, Waltham, MA 40–50 (2006).
174. M. Á. A. Caballero, "Incorporating Sensor Properties in Optoacoustic Imaging," (2013).
175. J. A. OK-Jensen, "FIELD: A Program for Simulating Ultrasound Systems," Med. Biol.

Eng. Comput. **34**, 351–352 (1996).

176. A. Berezhnoi, M. Schwarz, A. Buehler, S. V. Ovsepian, J. Aguirre, and V. Ntziachristos, "Assessing hyperthermia-induced vasodilation in human skin in vivo using optoacoustic mesoscopy," J. Biophotonics **11**, (2018).
177. H. Barcroft and O. G. Edholm, "The effect of temperature on blood flow and deep temperature in the human forearm.," J. Physiol. **102**, 5–20 (1943).
178. G. Mahé, A. Humeau-Heurtier, S. Durand, G. Leftheriotis, and P. Abraham, "Assessment of skin microvascular function and dysfunction with laser speckle contrast imaging," Circ. Cardiovasc. Imaging **5**, 155–163 (2012).
179. D. P. Stephens, N. Charkoudian, J. M. Benevento, J. M. Johnson, and J. L. Saumet, "The influence of topical capsaicin on the local thermal control of skin blood flow in humans," Am. J. Physiol. - Regul. Integr. Comp. Physiol. **281**, (2001).
180. D. a Boas and A. K. Dunn, "Laser speckle contrast imaging in biomedical optics.," J. Biomed. Opt. **15**, 011109 (2014).
181. M. Omar, M. Schwarz, D. Soliman, P. Symvoulidis, and V. Ntziachristos, "Pushing the Optical Imaging Limits of Cancer with Multi-Frequency-Band Raster-Scan Optoacoustic Mesoscopy (RSOM)," Neoplasia **17**, 208–214 (2015).
182. J. Aguirre, M. Schwarz, N. Garzorz, and M. Omar, "Precision assessment of psoriasis biomarkers using ultra-broadband optoacoustic mesoscopy," (n.d.).
183. Lasers Institute of America, *American National Standard for Safe Use of Lasers* (2007).
184. J. Aguirre, M. Schwarz, D. Soliman, A. Buehler, M. Omar, and V. Ntziachristos, "Broadband mesoscopic optoacoustic tomography reveals skin layers," Opt. Lett. **39**, 6297 (2014).
185. D. P. Stephens, N. Charkoudian, J. M. Benevento, J. M. Johnson, and J. Louis Saumet, "The influence of topical capsaicin on the local thermal control of skin blood flow in humans," (n.d.).
186. C. T. Minson, L. T. Berry, and M. J. Joyner, "Nitric oxide and neurally mediated regulation of skin blood flow during local heating Nitric oxide and neurally mediated regulation of skin blood flow during local heating," **97403**, 1619–1626 (2013).
187. A. W. Fulmer and G. J. Kramer, "Stratum corneum lipid abnormalities in surfactant-induced dry scaly skin," J. Invest. Dermatol. **86**, 598–602 (1986).
188. M. R. Prausnitz and R. Langer, "Transdermal drug delivery," Nat. Biotechnol. **26**, 1261–1268 (2009).
189. S. J. Ford, P. L. Bigliardi, T. C. P. Sardella, A. Urich, N. C. Burton, M. Kacprowicz, M.

Bigliardi, M. Olivo, and D. Razansky, "Structural and Functional Analysis of Intact Hair Follicles and Pilosebaceous Units by Volumetric Multispectral Optoacoustic Tomography," J. Invest. Dermatol. **136**, 753–761 (2016).

190. X. L. Deán-Ben and D. Razansky, "On the link between the speckle free nature of optoacoustics and visibility of structures in limited-view tomography," Photoacoustics **4**, 133–140 (2016).

191. K. Haedicke, L. Agemy, M. Omar, A. Berezhnoi, K. Nagar, H.-T. Hsu, K. Kim, J. Coleman, V. Ntziachristos, A. Scherz, and J. Grimm, "Listening to the therapy: High-resolution optoacoustic imaging allows real-time, non-invasive monitoring of the response to vascular-targeted therapy," Nat. Biomed. Eng. (2019).

192. A. Berezhnoi, B. Hindelang, L. Riobo, C. Schönmann, H. He, J. Aguirre, and V. Ntziachristos, "Oxygenation changes in human skin assessed by dual-wavelength raster–scanning optoacoustic mesoscopy," (n.d.).

193. A.-L. Steunou, B. Monsarrat, M. Erard, I. Lazar, O. Burlet-Schiltz, E. Clottes, L. Nieto, C. Muller, and M. Ducoux-Petit, "Identification of the Hypoxia-inducible Factor 2α Nuclear Interactome in Melanoma Cells Reveals Master Proteins Involved in Melanoma Development," Mol. Cell. Proteomics **12**, 736–748 (2013).

194. R. Kragelj, T. Jarm, T. Erjavec, M. Prešern-Štrukelj, and D. Miklavčič, "Parameters of postocclusive reactive hyperemia measured by near infrared spectroscopy in patients with peripheral vascular disease and in healthy volunteers," Ann. Biomed. Eng. **29**, 311–320 (2001).

195. D. T. Ubbink, M. J. H. M. Jacobs, and D. W. Slaaf, "Can transcutaneous oximetry detect nutritive perfusion disturbances in patients with lower limb ischemia?," Microvasc. Res. **49**, 315–324 (1995).

196. P. F.H. Cornelis, MD, P. K Kim, M. J.C. Durack, B. S Jebiwott, P. A Scherz, P. G Srimathveeravalli, and M. J. A. Coleman, "Contrast enhanced ultrasound imaging can predict vascular- targeted photodynamic therapy induced tumor necrosis in small animals," Photodiagnosis Photodyn Ther. **20**, 165–168 (2017).

197. U. Merschbrock, J. Hoffmann, L. Caspary, J. Huber, U. Schmickaly, and D. W. Lübbers, "Fast wavelength scanning reflectance spectrophotometer for noninvasive determination of hemoglobin oxygenation in human skin," Int. J. Microcirc. Exp. **14**, 274–281 (1994).

198. J. Aguirre, M. Schwarz, N. Garzorz, and M. Omar, "Precision assessment of psoriasis biomarkers using ultra-broadband optoacoustic mesoscopy," Nat. Biomed. Eng. **1**, 1–8 (2017).

199. V. Neuschmelting, K. Kim, J. Malekzadeh-Najafabadi, S. Jebiwott, J. Prakash, A. Scherz, J. A. Coleman, M. F. Kircher, and V. Ntziachristos, "WST11 vascular targeted photodynamic therapy effect monitoring by multispectral optoacoustic tomography (MSOT) in mice," Theranostics **8**, 723–734 (2018).

200. B. L. Wajchenberg, "Subcutaneous and visceral adipose tissue: Their relation to the metabolic syndrome," Endocr. Rev. **21**, 697–738 (2000).

201. S. Sakai, K. Kikuchi, J. Satoh, H. Tagami, and S. Inoue, "Functional properties of the stratum corneum in patients with diabetes mellitus: Similarities to senile xerosis," Br. J. Dermatol. **153**, 319–323 (2005).

202. G. Wissmeyer, M. A. Pleitez, A. Rosenthal, and V. Ntziachristos, "Looking at sound: optoacoustics with all-optical ultrasound detection," Light Sci. Appl. **7**, (2018).

203. A. Stylogiannis, L. Prade, A. Buehler, J. Aguirre, G. Sergiadis, and V. Ntziachristos, "Continuous wave laser diodes enable fast optoacoustic imaging," Photoacoustics **9**, 31–38 (2018).